IS-T 1538

Magnetiziation and Magnetostriction in Highly Magnetostrictive
Materials

by

Thoelke, Jennifer Beth

MS   Thesis submitted to Iowa State University

Ames Laboratory, U.S. DOE

Iowa State University

Ames, Iowa 50011

Date Transmitted: May 26, 1993

MASTER

DISCLAIMER

DISCLAIMER

Portions of this document may be illegible
in electronic image products. Images are
produced from the best available original
document.

For my parents, Robyn, and Michael,

TABLE OF CONTENTS

UNITS

To be uniform, SI units are used throughout this thesis. The following is a table of common quantities, the corresponding SI unit name, and symbol.

Quantity	Unit	Symbol
Length	meter	m
Mass	kilogram	kg
Time	second	s
Pressure	Pascal	Pa
Electric Charge	Coulomb	C
Electric Current	Ampere	A
Electric Potential	volt	V
Resistance	ohm	Ω
Capacitance	Farad	F
Inductance	Henry	H
Magnetic Flux	Weber	Wb
Magnetic Field	Ampere/meter	A/m[*]
Magnetization	Ampere/meter	A/m
Magnetic Induction	Tesla	T[**]

[*]1 A/m = 79.58 Oe
[**]1 T = 10^4 Gauss

ACKNOWLEDGEMENTS

Thanks are especially due to my committee members, David Jiles, Doug Finnemore, John Verhoeven, and Bruce Harmon for their patience in seeing this thesis through to its completion over such a long distance. In addition, I thank David Jiles for introducing me to magnetism, supervising my work at Ames Laboratory and encouraging me to attend and present my work at conferences. I also thank John Verhoeven and Dale McMasters (Edge Technologies) for their discussions on Terfenol and supplying me with some of the materials used in my experiments.

I thank Otto Buck and Ames Laboratory for financing my masters degree and giving me the financial support to attend conferences. In addition, thanks goes to Tom Lograsso, Harlan Baker, and all the other people at Ames Laboratory who have given me encouragement and help with this work. Thanks is also due to Joseph Holmes for his help in writing the computer code for the three-dimensional data generation program. I also thank the memebers of the magnetics group at Ames Laboratory. In particular, Russell Chang for many discussions on Terfenol research, and Patricia Pulvirenti for her friendship and interest in my research.

Many thanks is also due to Rod Greenough and the Department of Applied Physics at the University of Hull for letting me use their computer equipment during the final stages of my thesis.

Thanks is due especially to Michael my husband for all of his support and encouragement.

INTRODUCTION AND BACKGROUND

Overview

The majority of this research has been in developing a model to describe the magnetostrictive properties of Terfenol-D, $Tb_{1-x}Dy_xFe_y$ (x = 0.7-0.75 and y = 1.8-2.0), a rare earth-iron alloy which displays much promise for use in device applications. In the first chapter an introduction is given to the phenomena of magnetization and magnetostriction. The magnetic processes responsible for the observed magnetic properties of materials are explained. An overview is presented of the magnetic properties of rare earths, and more specifically the magnetic properties of Terfenol-D. In addition, methods of producing Terfenol-D are summarized including ways to improve its magnetostrictive performance.

In the second chapter, experimental results are presented on three compositions of $Tb_{1-x}Dy_xFe_y$ with x = 0.7, y = 1.9, 1.95, and x = 0.73, y = 1.95. The data were taken for various levels of prestress to show the effects of composition and microstructure on the magnetic and magnetostrictive properties of Terfenol-D. In the third chapter, a theoretical model is developed based on the rotation of magnetic domains. The model is used to explain the magnetic and magnetostrictive properties of Terfenol-D, including the observed negative strictions and large change in strain. The fourth chapter goes on to examine the magnetic properties of Terfenol-D along different crystallographic orientations. In this experiment, the magnetization curves of small [111] oriented samples

of Terfenol-D were investigated using a Vibrating Sample Magnetometer. The frequency response of magnetostrictive materials was investigated for potential use in engineering applications. In the fifth chapter initial data are presented on the time dependence of magnetization in nickel.

Magnetic Phenomena

Atomic magnetic moment

The fundamental unit of magnetism is the magnetic dipole. Its presence can be explained classically by the concept of electrical charge in motion in which there are two contributions to the resulting moment: orbital and spin angular momentum. In the classical picture, a single electron moving around an atomic nucleus is the orbital angular momentum, while spin angular momentum results from the intrinsic spin of the electron. In quantum mechanics, the orbital and spin angular momentum can only take on certain values. In the presence of a magnetic field, electron spins are constrained to lie either parallel or anti-parallel to the field, whereas the orbital momentum can only have certain values of the component parallel to the direction of the applied field.

The spins of each individual electron are coupled through the spin-spin interaction and can be summed to give the resulting spin vector S for the atom. The orbital angular momentum combines in the same manner resulting in an orbital vector L for the atom. The total angular momentum J is then the vector sum of the orbital and spin contributions.

$$\vec{J} = \vec{S} + \vec{L} \qquad \qquad (1)$$

The sum of the spin-spin interaction, orbital-orbital interaction, and spin-orbit interaction define the microscopic interactions in an atom. The spin-orbit interaction is commonly referred to as Russell-Saunders coupling and has relevance to most magnetic atoms.

The total spin angular momentum precesses about the time averaged component of the spin vector, while the total orbital angular momentum precesses about the time averaged component of the orbital vector. In addition, both the spin and orbital angular momentum precess about the time averaged component of the total angular momentum vector. The precession about the total angular momentum vector is usually much slower than the precession of the spin and orbital angular momentum about their own axes. For lighter atoms, the spin-orbit interaction is usually much weaker than the spin-spin and orbital-orbital interactions.

From a classical point of view, the magnetic dipole moment can be explained in much the same way as the angular momentum, because the two terms are inseparable. An intrinsic spin magnetic moment results which is related to the spin angular momentum of the electron. The concept of a charge in motion is easier to visualize in the case of the electron orbiting the nucleus. The magnetic field produced by this action is the same as that of a magnetic dipole at large distances from the electron and nucleus. An orbital magnetic dipole results which is related to the orbital angular momentum of the electron.[1]

The total magnetic moment of an electron turns out to be an integral multiple of a

constant commonly referred to as the Bohr magneton, μ_B, where

$$\mu_B = \frac{eh}{4\pi m_e} = 9.274 \times 10^{-24} \, J \cdot T^{-1} \tag{2}$$

and h denotes Planck's constant, e the charge of an electron, and m_e the mass of an

electron.[2] Since the majority of atoms have more than one electron, the magnetic

properties are not as simple to explain.

In multielectron atoms, the nucleus is surrounded by layers of electron shells. The

electronic structure is very ordered. Each shell consists of subshells which are filled one

electron at a time with the lowest energy subshells filled first.[1] According to Hund's

rules, it is the spin of the unpaired electrons which couple with the orbital angular

momentum to yield the total magnetic moment of an atom.

In materials, atoms exist in a crystalline structure. The magnetic moments of each

of the separate atoms will interact with each other to produce the magnetic properties for

the crystal structure.

Unlike the structure of the 3d electrons in the ferromagnetic transition metals, the

4f electrons in the rare earths are surrounded by four outer shells. For transition metals,

the 3d electrons are free to interact with other 3d electrons in a crystal. This interaction

leads to an overall magnetic moment of the crystal. In the rare earths, the 4f electrons are

shielded by four outer shells and cannot interact directly with the 4f electrons in

neighboring atoms. Instead the 4f electrons interact with the surrounding conduction

electrons in the same atom which then in turn interact with the other atoms in the crystal. Therefore, the 4f electrons interact with each other indirectly to produce an overall crystal magnetic moment.[3]

Magnetization

Exchange   Ferromagnetic materials are made up of many magnetic moments. It is the way in which these moments interact with each other and their response to the applied magnetic field that gives the observed macroscopic magnetic properties. In the simplest case, the interaction energy between two magnetic moments is given by[4]

$$E_{ex} = -2\mu_o J m_1 m_2 \cos\delta \tag{3}$$

where μ_o denotes the permeability of free space, J the exchange integral, m_1 and m_2 the magnitude of the two magnetic moments and δ the angle between the two moments. A positive value for J leads to ferromagnetism, and a negative value leads to antiferromagnetism. In ferromagnetic materials, the exchange energy is minimum when the angle between the moments is zero.

The strength of the exchange energy varies in different magnetic materials. Paramagnetic materials display a very weak coupling between neighboring magnetic moments compared with the thermal energy. However, in ferromagnetic, antiferromagnetic, and ferrimagnetic materials there is a very strong coupling between neighboring magnetic moments.

Magnetically ordered materials are characterized by their transition temperatures, the Curie and Néel temperatures. Above the Curie temperature, the thermal energy of the magnetic moments is greater than the exchange energy and tends to randomize the alignment of the moments making it paramagnet. Below its Curie temperature it is magnetically ordered.

While the Curie temperature of a ferromagnetic material separates a ferromagnetic phase from a paramagnetic phase, the Néel temperature of an antiferromagnetic material separates paramagnetic and antiferromagnetic phases. Below the Néel temperature in the antiferromagnetic phase, the anti-parallel spins completely cancel each other, whereas above the Néel temperature in the paramagnetic phase, the spins only cancel each other in the absence of an applied magnetic field.

<u>Domains</u>   On the atomic scale in a ferromagnet, magnetic moments prefer to align parallel to one another if the decrease in magnetostatic energy is greater than the energy needed to align the moments. In order to minimize the total energy of the material, magnetic domains are formed which represent magnetically saturated areas where all the magnetic moments lie parallel to one another.

Each domain is separated from others by a domain wall which is a transitional boundary between magnetic domains with spontaneous magnetizations pointing in different directions. The wall consists of a thin layer of a few hundred magnetic moments with individual orientations that are intermediate between the orientations of the neighboring domains. The width of a domain wall is determined by minimizing the anisotropy and exchange energy of the wall with respect to the width of the wall.

In a demagnetized state, a ferromagnetic material consists of many randomly oriented domains and therefore many domain walls. It is the movement of these domain walls and the rotation of magnetic domains under the action of an applied magnetic field that contribute to the change in the bulk magnetic properties of the material.

Domain magnetization processes   The magnetization of a material can change reversibly or irreversibly with the application of a magnetic field. A reversible change is one which returns to its initial magnetic state when the initial conditions are reestablished. An irreversible change is one in which the magnetization is not able to return to its initial magnetic state when the field is reversed unless an added external restoring force is applied. Reversible and irreversible magnetization changes can occur through two different magnetization processes: domain wall motion and domain rotation which are discussed separately here.

Domain wall motion   The moments within domain walls are more easily rotated into neighboring domains than an entire domain. The domain wall will appear to move when energy is added to or taken away from the magnetic system. For iron, the domain wall energy is 1.1×10^{-3} J/m^2.[5] As a magnetic field is applied, some of the moments within the wall will prefer to align with the moments in a neighboring domain, which lies closer to the direction of applied field, and the domain wall appears to move.

Crystal imperfections such as inclusions and residual stress impede the movement of a domain wall. An inclusion is generally defined as being a small region whose magnetic properties are different from the matrix material.

The magnetic poles of an inclusion are redistributed when the inclusion is

intersected by a domain wall lowering the magnetostatic energy. For large inclusions enclosed in a domain wall or domain, needle-shaped domains are generated to redistribute the magnetic poles and lower the magnetostatic energy of the inclusion. The presence of these domains increases the magnetostatic energy of the domain or domain wall, but there is still an overall decrease of the magnetostatic energy. In any case, an inclusion tends to act as an anchor to the wall and the magnetostatic energy of the inclusion is lowest when intersected by a domain wall.[6]

A reversible domain wall movement can be a bend in the wall or a translation of the wall across an energy plateau (ie. no inclusions). A domain wall will move irreversibly by attaching itself to a defect in the material in order to minimize the energy of the wall. The domain wall will want to stay attached to the defect until enough energy is put into the magnetic system to overcome the energy minimum.

A domain wall type is defined by the angle between the magnetization directions in two neighboring domains. For example, a 180 degree domain wall exists between two neighboring domains with directly opposing magnetization vectors. The movement of various types of domain walls affect magnetic properties in different ways.

Domain rotation   Rotation occurs when the magnetization vector of an entire domain changes direction. This requires an appreciable amount of energy input to the system in order for it to be energetically favorable for the rotation to occur. The energy input must be great enough to overcome the magnetic anisotropy of the material. Certain factors influence the ability of a material to change its magnetization through rotational processes. Anisotropy and stress affect the internal energy of a material and create areas

of preferred orientation. Rotational processes occur mostly at moderate to high magnetic field strengths because enough energy must be present in order to affect the large number of individual magnetic moments.[4]

Magnetic anisotropy   Anisotropy profoundly affects the rotation of magnetic domains. There are three different types of anisotropy: shape, magnetocrystalline, and magnetoelastic. Shape anisotropy affects the internal magnetic field of a material and is related to nonuniform internal demagnetizing fields expressed in the demagnetization factor.

Magnetocrystalline anisotropy is due to the crystal structure of the material and results in certain crystallographic orientations being magnetically favorable. The magnetocrystalline anisotropy energy[5] can be evaluated for a cubic crystal structure and to a first approximation depends on the first and second anisotropy constants K_1 and K_2 in the following way.

$$E_{an} = K_1(\alpha_1\alpha_2 + \alpha_2\alpha_3 + \alpha_3\alpha_1) + K_2\alpha_1^2\alpha_2^2\alpha_3^2 \qquad (4)$$

where α_i denotes the direction cosines of the magnetization. The anisotropy constants are in the units of an energy density and represent the strength of the anisotropy in the material. For $K_1 > 0$, there are six directions of minimum energy denoted by the six magnetic easy axes along the <100> directions. For $K_1 < 0$, there are eight directions of minimum energy denoted by the eight magnetic easy axes along the <111> directions.

For example in nickel[7], $K_1 = -5.9 \times 10^3$ J/m^3, and the crystal anisotropy energy

density along the <111> directions in nickel is around -2 x 10^3 J/m^3, whereas the

anisotropy energy density along the <100> directions is zero. In iron[7], K_1 = 4.7 x 10^4

J/m^3, and the crystal anisotropy energy along the <100> directions in iron is zero, whereas

the anisotropy energy density along the <111> directions is around 15.7 x 10^3 J/m^3. The

magnetization prefers to align along energy minima in the crystal, therefore in nickel the

preferred directions of orientation are the <111> directions, whereas in iron the preferred

directions are the <100> directions. These preferred directions of magnetization are often

referred to as the magnetic easy axes.

Magnetoelasticity and magnetoelastic effects

Magnetoelasticity   Magnetoelasticity is a result of changes in the elastic moduli

of a material brought about by the application of a magnetic field. The magnetoelastic

energy[7] is given by

$$E_\sigma = -\frac{3}{2}\sigma\lambda_{100}\sum_{i\neq j}^{3} \alpha_i^2\gamma_j^2 - 3\sigma\lambda_{111}\sum_{i\neq j}^{3} \alpha_i\gamma_i\alpha_j\gamma_j \qquad (5)$$

where λ_{111} and λ_{100} are the magnetostriction constants, σ the applied stress, α_i the direction

cosines of the magnetization, and γ_i the direction cosines of the applied stress. No change

in magnetoelastic energy is produced with 180° domain wall motion. In considering

equation 5, an applied stress can create new energy minima as a result of the coupling

between the magnetization and applied stress. A change in the dimensions of the material

will result if to do so lowers the total of the elastic, magnetoelastic and magnetocrystalline

energy of the material which in turn changes its elastic behavior.

Young's modulus E is the ratio of the applied stress (σ) to the strain (e).

$$E = \frac{\sigma}{e} \tag{6}$$

The value of Young's modulus for a ferromagnet is a function of magnetic field. The difference between Young's modulus in the presence of an applied magnetic field (E_o) and Young's modulus in the demagnetized state (E_a) is referred to as the ΔE effect.

$$\Delta E = E_o - E_a \tag{7}$$

When the only strain present is magnetostriction, the energy density, $\frac{1}{2}E\lambda_s^2$, denotes the amount of magnetic energy which can be transformed to elastic energy per unit volume of the material, where λ_s is the saturation magnetostriction.[8] The ratio of magnetic energy stored as magnetoelastic energy gives a measure of the efficiency of the material, k^2, where

$$k^2 = \frac{d^2}{s\mu} \tag{8}$$

and d denotes the change in strain with field, s the compliance at constant induction, and μ the permeability at constant strain.[8]

<u>Magnetostriction</u>   Formally, the origin of magnetostriction lies in the fact that

the anisotropy energy, like the exchange energy, varies with the interatomic distance. In other words, a crystal lattice will distort to minimize the anisotropy energy of the material. On the atomic scale, spin-orbit coupling plays an important role in explaining both anisotropy and magnetostriction in the rare earth elements. The 4f-subshells display an asymmetric charge distribution for all possible values of the orbital angular momentum, except the 4f-element Gadolinium. Coulomb interaction between nearest neighbors in a lattice results in large potentials and a strong anisotropy.[7]

Magnetostriction results from a spontaneous distortion of a magnetic domain in the crystal lattice due to the interaction of the magnetic moments within the domain. The sum over all domains produces an overall change in the dimensions of a material. There are three types of magnetostriction: anisotropic, volume, and forced at very high magnetic fields.

It is essential to consider the magnetic symmetry of the material when describing anisotropic magnetostriction. The anisotropy of the material defines the magnetic symmetry and greatly affects the resulting equation describing magnetostriction. Anisotropic magnetostriction results in a distortion of the domain that conserves its volume. If the domain is elongated in one direction, it is contracted perpendicular to this direction. A change in the length of the material along the direction of applied field is referred to as longitudinal magnetostriction, while a change in the length perpendicular to the direction of the applied field is referred to as transverse magnetostriction.

In cubic anisotropic materials, the saturation magnetostriction[5] is given as a function of angle by

$$\lambda_l = \frac{3}{2}\lambda_{100}(\alpha_1^2\beta_1^2+\alpha_2^2\beta_2^2+\alpha_3^2\beta_3^2-\frac{1}{3})$$
$$+ 3\lambda_{111}(\alpha_1\alpha_2\beta_1\beta_2+\alpha_2\alpha_3\beta_2\beta_3+\alpha_3\alpha_1\beta_3\beta_1) \tag{9}$$

where λ_{111} and λ_{100} are the magnetostriction coefficients, α_i the direction cosines for the magnetization, and β_i the direction cosines for the measurement direction which is usually parallel to the field direction. The magnetostriction coefficients, λ_{111} and λ_{100}, denote the fractional elongation along the respective axes when the magnetization vector lies along these directions relative to the demagnetized state, and are derived in terms of the strain components in appendix A. In iron, $\lambda_{111} = -21.2 \times 10^{-6}$ and $\lambda_{100} = 20.7 \times 10^{-6}$, and the two constants are almost equal, but opposite in sign.[7]

Transverse magnetostriction is measured perpendicular to the direction of the applied field and is opposite and proportional to the longitudinal magnetostriction of the material. In a completely isotropic material, the longitudinal and transverse magnetostriction are related through the following equation which is a consequence of volume conservation.

$$\lambda_l = -\frac{\lambda_\perp}{2} \tag{10}$$

where λ_l denotes the longitudinal magnetostriction, and $\lambda_\perp$ the transverse magnetostriction.

The simplest equation of magnetostriction is for an isotropic material, where there is no preferred direction of orientation for the magnetization vector. The crystal therefore can be distorted equally in all directions. The saturation magnetostriction coefficient, λ_s, denotes the elongation of the material when measured along any direction in the crystal.

For an isotropic material, $\lambda_{111} = \lambda_{100} = \lambda_s$, where λ_s is the saturation magnetostriction coefficient, and the saturation magnetostriction can be rewritten as

$$\lambda_1 = \frac{\lambda_s}{2}[3(\alpha_1^2\beta_1^2 + \alpha_2^2\beta_2^2 + \alpha_3^2\beta_3^2) - 1 \\ + 6(\alpha_1\alpha_2\beta_1\beta_2 + \alpha_2\alpha_3\beta_2\beta_3 + \alpha_3\alpha_1\beta_3\beta_1)] \tag{11}$$

Rearranging terms,

$$\lambda_1 = \frac{\lambda_s}{2}[3(\alpha_1^2\beta_1^2 + \alpha_2^2\beta_2^2 + \alpha_3^2\beta_3^2 + 2\alpha_1\alpha_2\beta_1\beta_2 \\ + 2\alpha_2\alpha_3\beta_2\beta_3 + 2\alpha_3\alpha_1\beta_3\beta_1) - 1] \tag{12}$$

and recognizing that the term in parenthesis is $\cos^2\theta$, where θ is the angle between the direction of magnetization and the direction of the applied magnetic field, the equation can be rewritten as

$$\lambda_1 = \frac{3}{2}\lambda_s[\cos^2\theta - \frac{1}{3}] \tag{13}$$

The magnetostriction coefficients are characteristic of the material and only change if the interactions responsible for the magnetic state of the material change. Temperature,

composition, and crystallographic order affect the values of the magnetostriction coefficients.[5]

Volume magnetostriction, where the volume of the material is changed by magnetization, only becomes significant after magnetic saturation. It is the result of domains aligned along the field direction increasing their volume equally in all directions producing an increase in the volume of the material. Forced magnetostriction is also a volume effect. If a ferromagnet is magnetized beyond saturation (at 0 K), the alignment of the moments within the domain is increased and the magnetostriction observed is primarily a forced change in the volume of the material. The change in strain is equal in all directions, as a result of the rotation of magnetic domain vectors and spontaneous magnetostriction.[5] The magnetostriction due to volume effects is usually very small and difficult to calculate.

Terfenol-D

Introduction to Terfenol-D

In mid-1800s Joule was the first to discover the effect of magnetostriction as he observed and measured a change in the length of iron when magnetized.[9] By the early 1900s magnetostrictive materials were being utilized in devices such as high frequency oscillators and generators. In the Second World War, magnetostrictive materials were used in transducers and actuators in underwater equipment as sources and receivers of sound.[10] At that time even a strain of 100×10^{-6} was considered to be a high saturation

magnetostriction. Table 1 lists many of the early magnetostrictive materials, magnetostriction coefficients, and magnetomechanical coupling coefficients along the rod axis.

In the early sixties, high purity rare earth elements were found to possess extraordinarily unique magnetic properties at cryogenic temperatures. For example, neutron diffraction experiments revealed more complex spin structures than existed in the known classical transition element ferromagnets. Parallel coupling between large spin and orbital angular momenta in the rare earths yielded huge magnetic moments, between 7 μ_B and 11 μ_B at 4 K.[15] Studies done on the magnetostrictive properties of single crystal hexagonal Terbium (Tb) and Dysprosium (Dy) revealed their unprecedented basal plane magnetostrictions.[16,17,18] These basal plane strains were 100 to 1000 times greater than typical magnetostrictions and today remain the largest known.

Table 1. A few of the early magnetostrictive materials and their characteristics

Composition (by % wt.)	λ_{111} (10^{-6})	λ_{100} (10^{-6})	k_{33} (%)	Reference
Fe	-15.7	20	---	11
3.06% Si-Fe	-4.1	23	---	11
Ni	-24.3	-58.3	---	11
45% Co-Fe	30	130	---	11
$Co_{0.8}Fe_{2.1}O_4$	45	-515	---	12
40% Ni-Fe	λ_s = 130 ppm		37%	13
10.5% Al-Fe	λ_s = 35 ppm		$\approx$29%	14

Most of the heavy rare earths also exhibited enormous magnetic anisotropies at low temperatures because of the strong coupling between the spin and orbital angular momentum of the 4f-subshell. Gadolinium was the exception with no orbital angular momentum and only spin-spin interactions contributing to the magnetocrystalline anisotropy.

At high temperatures the rare earth elements lose their extraordinary magnetic properties and become paramagnetic at the Curie temperature, T_c. The rare earth elements all possess Curie temperatures below room temperature, except for Gadolinium. The low ordering temperatures and high magnetic anisotropies of the rare earth elements exclude the use of their magnetostrictive properties in device applications.

The maximum magnetostrictions of single crystal terbium and dysprosium were measured to be 3000 ppm and 7500 ppm, respectively, at 20 K with the magnetization vector restricted to lie in the (001) hexagonal basal plane at low temperatures due to the high magnetic anisotropy of the rare earths. The Curie point for dysprosium is 85 K, and the Néel point 178 K. Below the Néel temperature, the spins are in a helical configuration.[16,18]

To stabilize the magnetic system and maintain the magnetostrictions in Tb and Dy at high temperatures, transition elements were alloyed with the rare earth elements to increase the Curie temperature. In contrast to Ni and Co, when iron was alloyed with Tb and Dy, the Curie temperature of the resulting rare earth-iron alloy increased with increasing iron concentration. The highest ordering temperatures, around 300-400°C, were found for RFe_2 which exhibited the cubic Laves phase structure[19] shown in Figure 1,
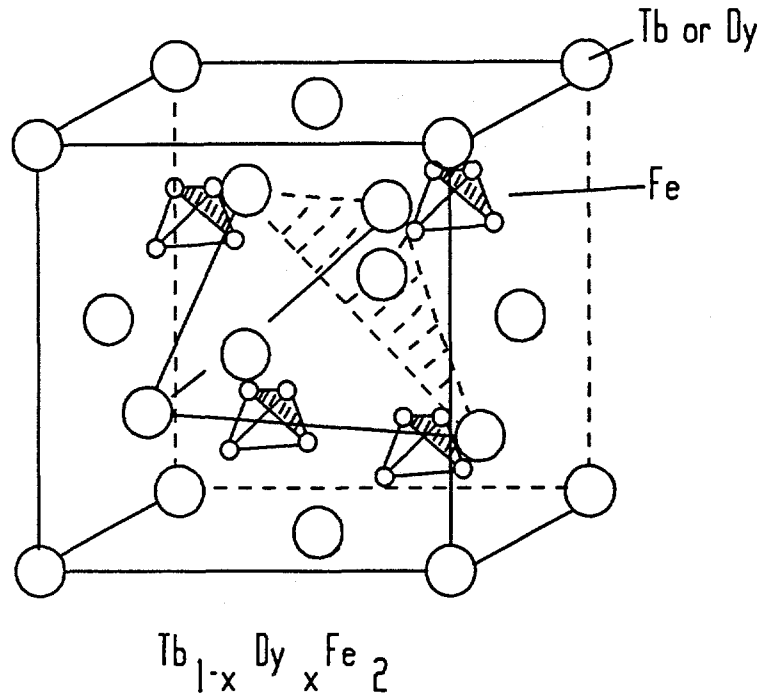
Figure 1. The laves phase in Terfenol

where R indicates rare earth.

The high Curie temperatures of these compounds along with their high rare earth concentration are responsible for the high room temperature magnetostrictions found in $SmFe_2$ (negative) and $TbFe_2$ (positive). The only drawback of these compounds is their high magnetocrystalline anisotropy. For example, $TbFe_2$ possesses an anisotropy energy greater than 10^6 J/m^3 and the field at which the maximum change in magnetic induction occurs is greater than 8,000 kA/m.[8]

$TbFe_2$ and $DyFe_2$ both have positive magnetostrictions, but compensating anisotropies (for $TbFe_2$, $K_1 < 0$, and for $DyFe_2$, $K_1 > 0$). In an attempt to lower the overall magnetic anisotropy of rare earth-iron compounds but retain high room

temperature magnetostrictions, Tb and Dy were combined with iron[8] to form a new compound referred to as Terfenol-D, which possessed a low magnetocrystalline anisotropy constant, $K_1 = -60,000$ J/m^3 for $Tb_{0.3}Dy_{0.7}Fe_{1.95}$, with $T_c = 375°C$ and high room temperature magnetostriction, with $\lambda_{111} = 1640$ ppm.[8]

The magnetostriction of Terfenol-D exhibits magnetoelastic anisotropy which can be approximately characterized by the two lowest order magnetostriction constants λ_{111} and λ_{100}. The two magnetostriction constants considered, λ_{111} and λ_{100}, represent respectively, the magnetostriction along the [111] direction and along the [100] direction when the magnetic field is applied along that direction. In Terfenol-D there is a high anisotropy in the strain, $\lambda_{111} \gg \lambda_{100}$, which is not found in iron and nickel. For Terfenol-D, λ_{111} has been measured to be 1640 ppm and λ_{100} is in the range of 50-100 ppm.[4]

The unit cell of the cubic Laves phase is composed of two rare earth atoms and four iron atoms. The rare earth spins are parallel to one another and anti-parallel to the iron spins, resulting in a ferrimagnetic structure for Terfenol-D.[19]

The spontaneous distortion observed in Terfenol-D is due to the coupling of the crystalline electrostatic field with the total angular momentum of the 4f electrons. In the [100] plane, the rare earth atoms are equidistant from the surrounding iron atoms, where the rare earth atoms can be either terbium or dysprosium. In the [111] plane, the rare earth atoms are not equidistant from the nearest neighboring atoms and a spontaneous internal distortion of the crystal lattice results due to the Coulomb attraction.[19]

Grain oriented Terfenol-D exhibits a large bulk room temperature magnetostriction which significantly increases for the $Tb_{0.3}Dy_{0.7}Fe_2$ composition upon the application of a

compressive prestress along the growth direction. The main reason for the change in magnetostriction is a domain occupancy effect caused by the applied stress. In Terfenol-D, λ_{111} is large and positive, and an externally applied stress decreases the internal energy of the crystal at right angles to the stress applied along the [11$\bar{2}$] direction. Two of the <111> magnetic easy axes lie at right angles to the [11$\bar{2}$] direction, the typical direction of applied stress and field in Terfenol-D. An applied stress will increase the population of these two easy directions resulting finally in a ninety degree rotation of the domains into the field direction. A ninety degree rotation gives the maximum achievable strain.

However, the magnetic properties of Terfenol-D are very sensitive to a change in composition or heat treatment which can pose a problem in applications which require consistent and well-documented properties.[20] For example, $Tb_{0.3}Dy_{0.7}Fe_{1.95}$ displays a bulk magnetostriction well over 1000 ppm and a discontinuous change in strain, whereas in $Tb_{0.27}Dy_{0.73}Fe_{1.95}$ the maximum strain has decreased significantly and the discontinuous change in strain has disappeared.[20,21]

Production of Terfenol-D

RFe_2 compounds are usually produced via single crystal growth techniques even though the final product is actually a twinned single crystal. Material properties can be greatly influenced by the growth technique and the methods of preparation once the material is grown. As a result, many techniques for growing crystals exist in addition to various heat treatments known to improve material properties.[22] In the case of Terfenol-D, $Tb_{1-x}Dy_xFe_y$ (x = 0.7-0.75 and y = 1.8-2.0), the method of preparation has been shown

to have profound effects on the magnetoelastic properties of the final material. Therefore a short review follows of the wide range of chemical compositions, growth techniques, and heat treatments available in the production of Terfenol-D both scientifically and commercially.

The Terbium and Dysprosium atoms are similar in size and chemical behavior. It can be seen by looking at the binary phase diagrams[23,24] for TbFe and DyFe shown in Figure 2 that the two compounds are formed by very similar reactions. Primary Terbium-iron forms Tb_6Fe_{23} followed by $TbFe_3$ at 1212°C before forming secondary $TbFe_2$ at 1187°C, while Dysprosium-iron forms $DyFe_3$ at ≈ 1500°C before forming $DyFe_2$ at 1770°C. It is assumed that Terfenol-D forms through a peritectic reaction, which means in this case that the primary RFe_3-crystal phase uses its surrounding melt to form a new crystal structure (RFe_2). After heating both $TbFe_2$ and $DyFe_2$ to a liquid, the material is cooled and eventually forms a crystalline RFe_3 structure within the melt of rare earth-iron, where R is Tb and Dy. As the material is cooled further the RFe_3 crystals react with the molten rare earth rich melt to produce $Tb_{1-x}Dy_xFe_y$ (x = 0.7-0.75 and y = 1.8-2.0). The initial composition must be kept below $Tb_{1-x}Dy_xFe_2$ to reduce the possibility of the growth of the brittle primary iron rich RFe_3 structure which reduces the strain and mechanical strength.[25]

A well-grown Terfenol-D rod is usually composed mostly of dendritic sheets with a small amount of excessive rare earth phase between the platelets oriented in the [11$\bar{2}$] direction. A small change in either x or y can result in a significant change in the final product and the resulting magnetic properties. The ideal composition for applications has
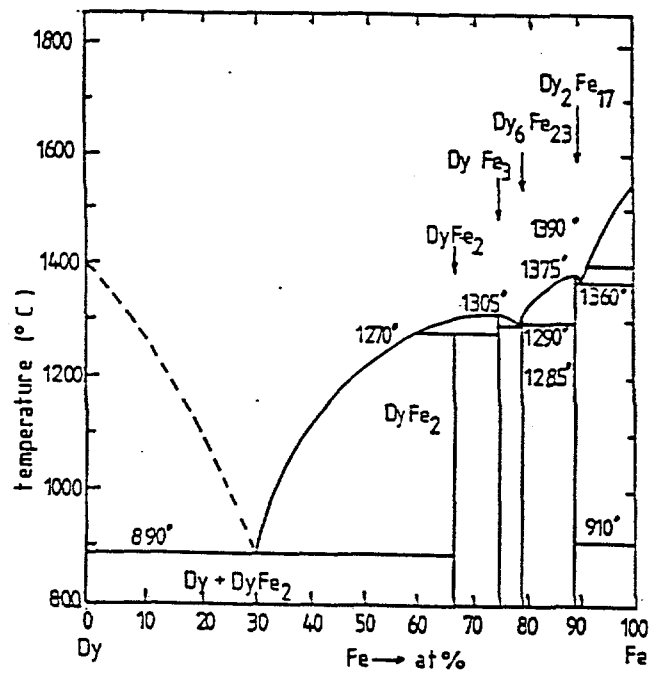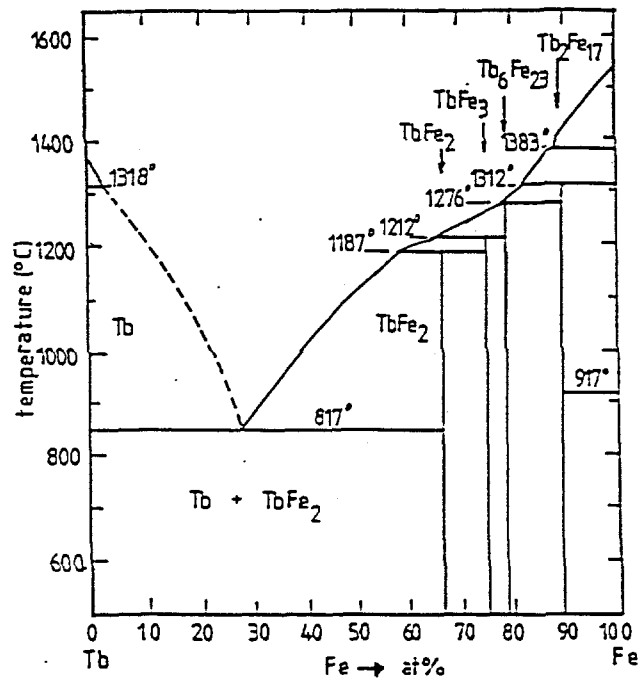
Figure 2. Phase diagrams for TbFe (top) and DyFe (bottom)

been found to be $Tb_{1-x}Dy_xFe_y$ with x = 0.7 and y = 1.95. When y < 2, the brittleness

decreases, but the maximum bulk magnetostriction also tends to decrease. With y = 1.95,

the brittleness is decreased without compromising the magnetostrictive strain. Changing

the value of x changes the magnetocrystalline anisotropy of the final material. It is

important to keep the ratio of Terbium to Dysprosium constant throughout the material

while it is grown in order to keep the magnetic properties uniform along the length of the

material.[22]

Many different techniques are available for growing crystals. With any technique

a few general conditions must be met in order to successfully grow single crystals. The

rate of crystal growth must balance with the thermal conditions present. The thermal

gradient at the growth interface is important in establishing the shape and perfection of the

grown crystal. The highest thermal gradient must coincide with the growth plane of the

crystal to minimize imperfections caused by second phases. Imperfections tend to

propagate throughout the remainder of the growth when not stopped early. It is also

Table 2. The advantages and disadvantages of different single crystal growth techniques

Technique	Advantages	Disadvantages
Czochralski	growth direction and size of material are easily controlled by observation	crucible
Float Zone Melting	crucibleless, normally a purification technique	only small diameter samples
Bridgeman	able to grow large diameter samples	crucible

important to start with a very high quality crystalline "seed" crystal. The Czochralski, Bridgman, and float zone techniques have been used successfully to grow twinned single crystal Terfenol-D.[25,26,27] A summary of the advantages and disadvantages of these techniques is given in Table 2.[22]

MAGNETIC AND MICROSTRUCTURAL PROPERTIES OF DIFFERENT COMPOSITIONS OF TERFENOL-D UNDER VARIOUS PRESTRESS CONDITIONS

Magnetization and Magnetostriction in Terfenol-D

Demagnetized and at room temperature, the magnetic moments in Terfenol-D prefer to align along the <111> easy directions. A magnetic field applied along the [11$\bar{2}$] growth direction in Terfenol-D results in 70.5°, 109°, and 180° domain wall movement because of the symmetry between the <111> directions.[25] The shape of the magnetization curve is determined by various mechanisms such as magnetocrystalline anisotropy and domain wall pinning which affect the hysteresis.

A magnetization curve (M vs. H) holds important information about the magnetic properties of a material. Figure 3 shows a typical magnetization curve for a ferromagnet. The curve is produced by cycling a magnetic field from zero to a positive maximum value then to the negative maximum value and back again to the positive maximum value while measuring the magnetization of the material. The slope of the hysteresis loop at any field, dB/dH, is the differential permeability.

Both magnetostriction and magnetization are material properties which are affected differently by domain wall motion and rotation. The magnetization of a material is related to the magnetic induction through the simple equation
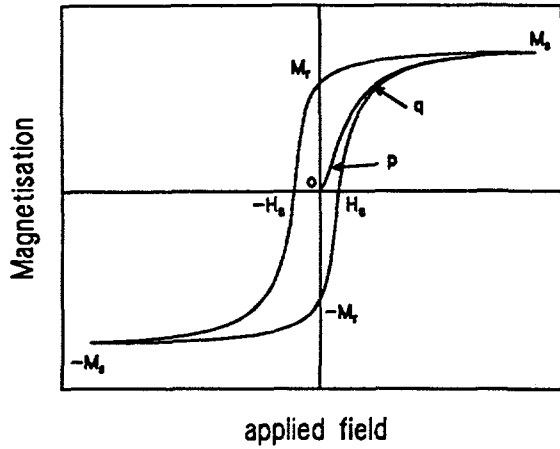
$$B = \mu_o(H + M) \qquad (14)$$
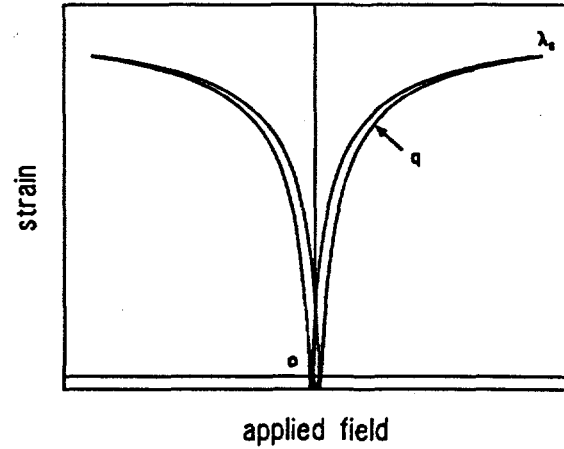
Figure 3. Magnetization curve

Figure 4. Magnetostriction curve

where μ_0 denotes the permeability of free space, B the magnetic induction, H the applied

magnetic field, and M the magnetization. Magnetization processes are fairly well

understood and can be used to explain the observed magnetic properties.

The material starts in the demagnetized state where the bulk magnetization is zero

due to a random distribution of the magnetic domain orientations, point 'o' in Figure 3.

As the magnetic field is slowly increased, the magnetization at low fields, up to point p,

expressed through the initial permeability, μ_i, can be attributed to reversible domain wall

motion (domain growth).

At higher fields, the magnetization is due mostly to irreversible domain wall

motion and the rotation of magnetic domains into a direction along or closer to the

direction of the applied field. In the region between points 'p' and 'q', the large change

in magnetization is due mainly to irreversible domain wall motion and rotation and can be

expressed using the maximum differential permeability, μ'_{max}. After the knee of the magnetization curve is reached, point 'q', the small increases in magnetization are due to reversible domain rotation as the material approaches saturation M_s. Technical saturation is reached when the material is converted to a single domain. Beyond that there is forced magnetization where the magnetization is pulled away from the easy direction.

Certain points on the magnetization curve have particular definitions. The coercivity, H_c, of the material is defined by the coercive force which is the field needed to return the residual magnetization to zero from saturation. M_r denotes the remanent magnetization or the magnetization present in the material after the applied magnetic field has been decreased to zero. Hysteresis is observed as the field is decreased to zero and the magnetization does not follow its original path to zero. The area inside the hysteresis loop is referred to as the hysteresis loss and is an energy density.

The magnetostriction curve (λ vs. H) shown in Figure 4 takes on a slightly different shape than the magnetization curve. The bulk magnetostriction is usually set arbitrarily to zero in the demagnetized state, point 'o'. At low fields, the magnetostriction can be attributed to domain wall motion. $71°$ and $109°$ domain wall motion will result in a small increase in magnetostriction, whereas $180°$ wall motion contributes nothing to the measured strain. Some materials display a negative strain. In the case of Terfenol-D under certain initial conditions both negative and positive strain can be observed but the large positive strain is the dominant feature of the material. At higher fields the large changes in magnetostriction are due to rotational processes. Past point 'q', the increase in strain is due to reversible rotational processes. As the curve approaches saturation, λ_s, the

increase in magnetostriction is due to coherent rotation. When the magnitude of the applied magnetic field is decreased to zero from saturation, the remaining strain due to irreversible magnetic processes is referred to as the remanent magnetostriction. The slope of the λ vs. H curve is referred to as the strain coefficient d_{33}.

The different magnetic processes occurring in magnetization and magnetostriction curves are not as clearly defined as they may seem. All the processes are interdependent. The magnetic processes responsible for large increases in magnetization are not always the same processes responsible for large increases in magnetostriction. Therefore the separation between magnetic processes can be seen more clearly in plots of the magnetization versus magnetostriction. Annealing samples can enhance the separation of the different processes.[28]

The factors which inhibit domain wall movement in Terfenol-D are crystal and magnetoelastic anisotropy and parent-twin boundaries. When a magnetic field is applied to any material the first processes to occur are those that are most energetically favorable, 180° wall motion. As the field increases further, domain wall movement will align all the domains along the most energetically favorable directions determined by the sum of field and anisotropy energies. In Terfenol-D with no prestress and no field, these are the <111> easy axes. As compressive prestress increases, the [111] and [$\bar{1}\bar{1}$1] directions which are at right angles to the direction of applied stress become energetically most favorable.

The parent-twin structure in Terfenol-D plays an important role in the magnetic processes. The parent subcrystal orients along the [11$\bar{2}$] direction, which is the primary

growth direction in Terfenol-D.[29] The twin subcrystal can be defined as a 180° rotation of the parent subcrystal around the [111] direction, which is 90° to the [11$\bar{2}$] direction. The [$\bar{1}\bar{1}$2] direction is then oriented along the rod axis in the twin, as the [11$\bar{2}$] direction lies along the rod axis in the parent.

It is not energetically favorable for domain walls to cross the parent-twin boundaries in Terfenol-D. For example, two domains lie on either side of the parent-twin boundary. They are oriented along the <111> direction 19.5° from the direction of applied field which lies along the rod axis. One domain would have to rotate 39° in order for the two domains to merge into one. The process of rotation requires a larger amount of energy, therefore it is thought that the parent-twin boundary inhibits the movement of domain walls increasing the hysteresis loss.[25]

$Tb_{1-x}Dy_xFe_y$ with $0.70 \leq x \leq 0.75$ and $1.8 \leq y \leq 2.0$ are the compositions of Terfenol-D which are widely used in applications. A lower iron content results in a less brittle material, while the larger x content has the effect of decreasing the magnetocrystalline anisotropy. The $x = 0.7$ composition displays a larger change in magnetostriction but the $x = 0.73$ composition is easier to control in devices because of a more linear change in strain with applied field and a decrease in hysteresis and magnetocrystalline anisotropy.

The $Tb_{0.3}Dy_{0.7}Fe_{1.9}$ composition is commonly used in applications because it sometimes displays the "burst effect"[30], an almost discontinuous change in strain with respect to magnetic field when a prestress is applied, with values of d_{33} approximately 105 x 10^{-9} m/A.[31] The magnetocrystalline anisotropy is larger for the $Tb_{0.3}Dy_{0.7}Fe_{1.95}$

composition than for the $Tb_{0.27}Dy_{0.73}Fe_{1.95}$ composition. Higher anisotropy restricts the rotation of domains until higher field strengths are applied.

The microstructure and magnetic properties of three specific compositions of Terfenol-D, $Tb_{0.3}Dy_{0.7}Fe_{1.9}$, $Tb_{0.3}Dy_{0.7}Fe_{1.95}$, and $Tb_{0.27}Dy_{0.73}Fe_{1.95}$, have been investigated with the intention of presenting an overview of the properties of three different compositions widely used in applications.

Materials and Experimental Methods

Materials

Four samples of Terfenol-D with different compositions were tested. The four samples provided by Ames Laboratory and Edge Technologies in Ames were grown using the float zone technique. All four samples were 6 mm in diameter and about 50 mm in length.

Samples one and two were of composition $Tb_{0.3}Dy_{0.7}Fe_{1.9}$. Both samples were cut from the same cylindrical Terfenol-D rod after it was annealed at 950°C for one hour and then furnace cooled. This particular Terfenol-D rod was grown purely for scientific research at Ames Laboratory.

Optical macrographs and micrographs were taken of samples one and two in order to record and better characterize their crystallographic make-up. The two samples were lightly ground and electropolished in a 4% Perchloric acid-Methanol solution at 20°C and 50 V dc, before the pictures were taken.

Figure 5 shows an optical macrograph and micrograph of one end of sample one. The macrograph shows a few misaligned grains within a single crystal structure. These misaligned grains disappear before reaching the other end of this sample, which is single crystal. The optical micrograph also shows the compositional variations in the material. The white regions in the optical micrograph represent a pure Terfenol-D phase, while the black regions represent a rare earth phase.[25] Ideally a material with no inclusions or black regions is wanted, but when Terfenol-D is grown a rare earth phase usually develops between the dendritic sheets.

Optical macrographs and micrographs of one end of sample two are shown in Figure 6. The macrograph shows a grain oriented structure with the parallel lines across the surface representing the dendritic sheets that Terfenol-D grows in. The optical micrograph reveals that the dendritic sheets are composed of areas rich in rare earth phase. The optical macrographs and micrographs in Figure 6 are typical representations of the microstructure of Terfenol-D samples.

Samples three and four were grown commercially by Edge Technologies in Ames. Sample three had a composition of $Tb_{0.27}Dy_{0.73}Fe_{1.95}$ and sample four had a composition of $Tb_{0.3}Dy_{0.7}Fe_{1.95}$.

Experimental methods

Two separate experimental set-ups were used. Measurements were taken on samples one and two using the hysteresisgraph[32] shown in Figure 7. The computer controlled system simultaneously records the magnetic induction and magnetostriction of a
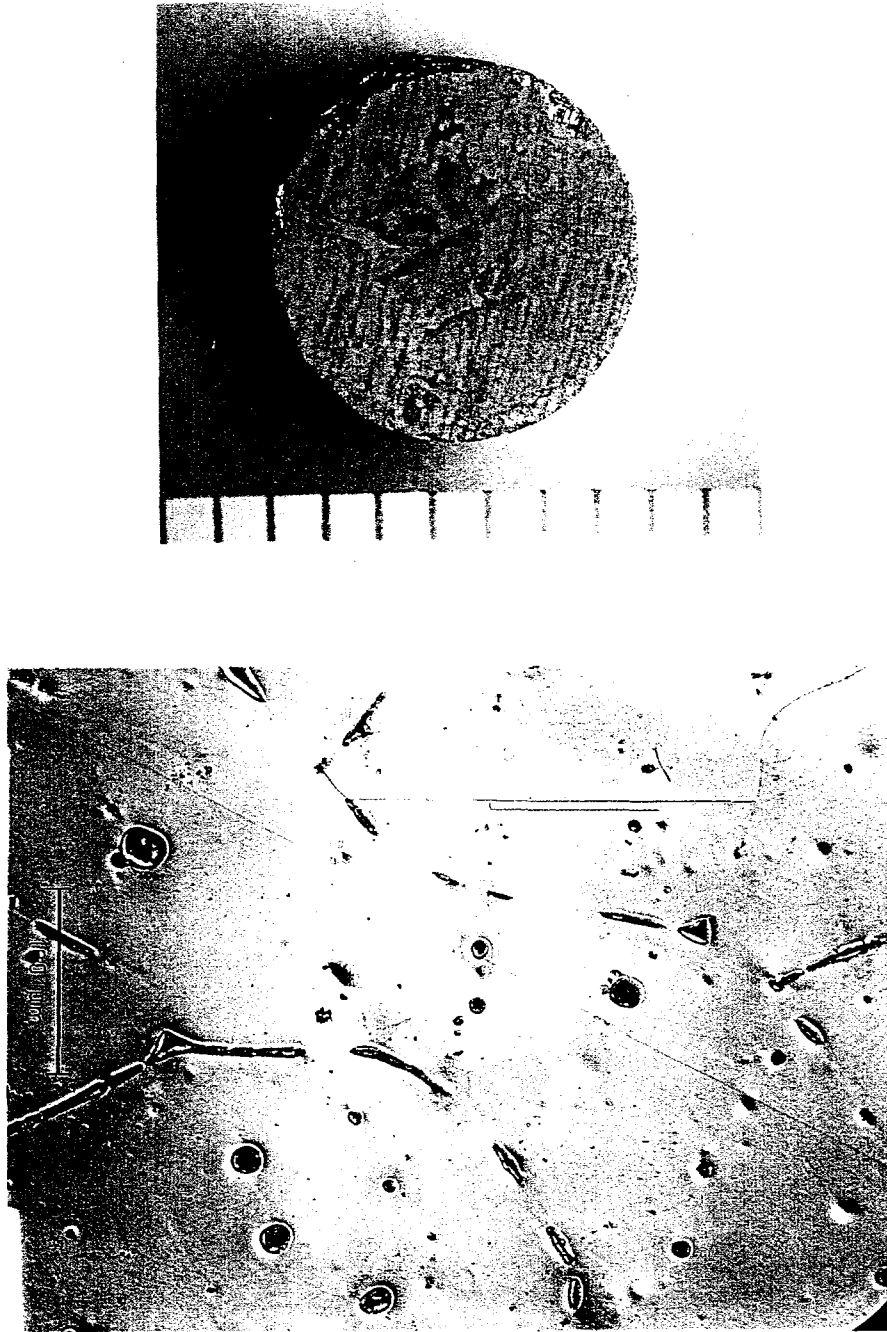
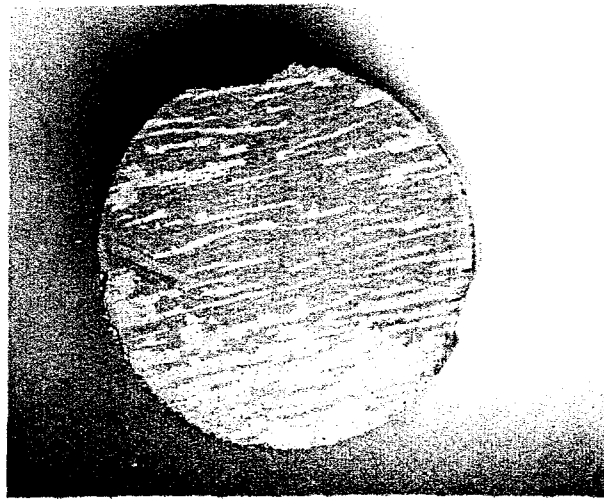Figure 5. Optical macrograph (top) and optical micrograph (bottom) of sample one

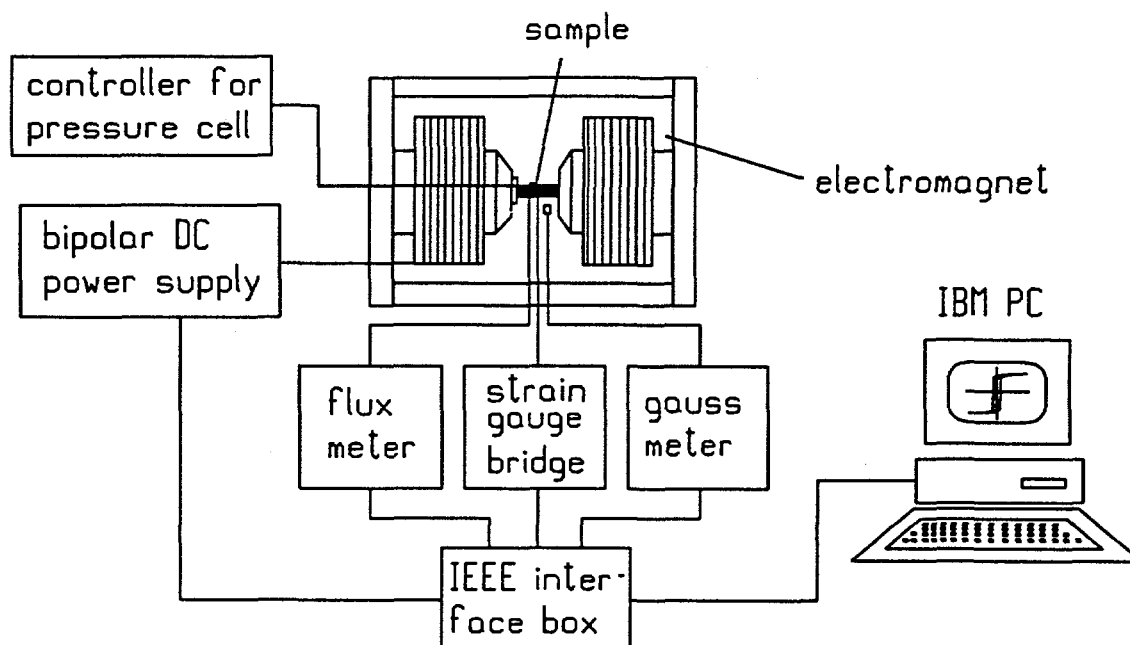Figure 6. Optical macrograph (top) and optical micrograph (bottom) of sample two

Figure 7. Experimental set up with electromagnet

magnetic material while the applied magnetic field is cycled. In the first set-up, the

sample is placed between two pole pieces of an electromagnet whose input current is

supplied by a bipolar power supply, and controlled from the computer.

A Hall probe attached perpendicular to the center of the sample measured the

applied magnetic field, and a 100 turn coil of insulated copper wire wrapped around the

middle of the sample and connected to an integrating fluxmeter measured the

magnetic induction through the rod. A commercial strain gauge glued to the center of the

sample along with a commercial strain gauge bridge measured the magnetostriction. A

nitrogen charged pressure cell attached to one pole of the electromagnet applied pressure

to the sample. The magnetic measurements were taken at compressive prestresses of 0, 3.5, 7, 10.5, and 14 MPa after the sample was demagnetized.

Samples three and four were tested on a different system shown in Figure 8 consisting of a 500 mm long solenoid of insulated copper wire. The magnetic field was generated by a current, produced by a bipolar power supply and changed linearly using a frequency generator running at 0.0016 Hz. Pressure was applied to the sample using a spring system made available by the University of Hull in the United Kingdom.[33] The spring system consisted of a spring with a known spring constant through which the pressure was applied uniaxially to the sample. A 100 turn coil of insulated copper wire
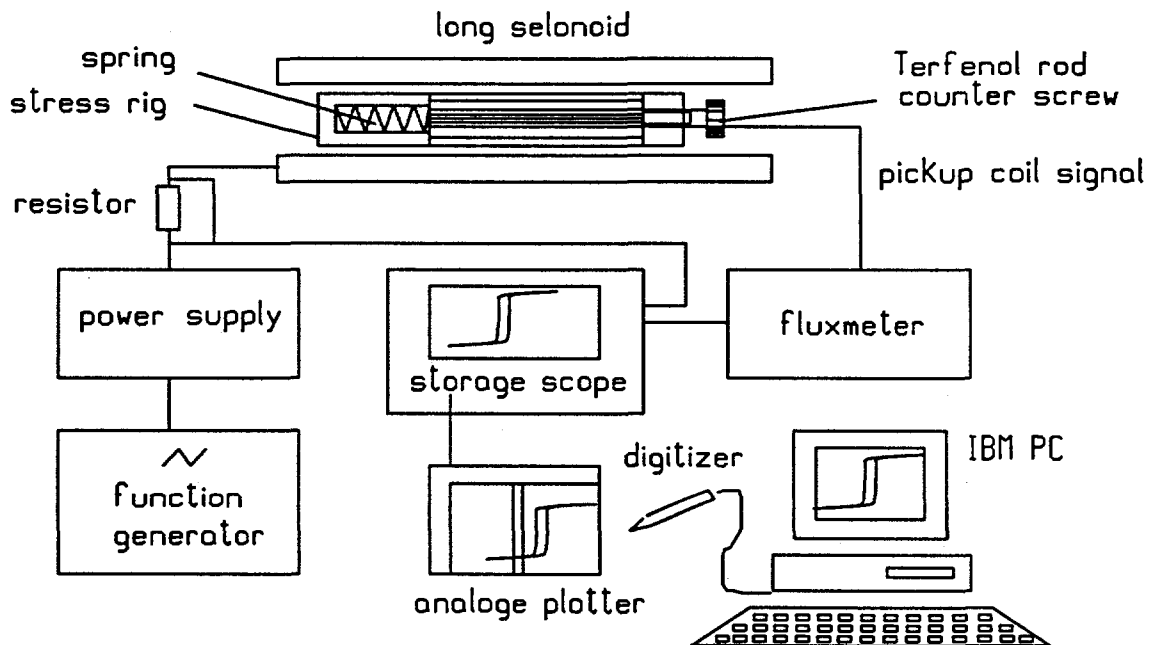
Figure 8. Experimental set-up with solenoid

wrapped around the middle of the sample measured the magnetic flux through the rod. A commercial strain gauge attached to the center of the sample along with a commercial gauge bridge measured the magnetostriction. The magnetic measurements were taken at compressive prestresses of 0, 3.5, 7, 10.5, and 14 MPa after the sample was demagnetized. The data were stored on an oscilloscope and then plotted on paper. The final graph was digitized and stored on disk. The two systems utilized were seen to give similar output.

Results

Plots of magnetic induction and magnetostriction versus magnetic field (B vs. H and λ vs. H, respectively), and magnetostriction versus magnetic induction (λ vs. B) for samples one and two, $Tb_{0.3}Dy_{0.7}Fe_{1.9}$, at compressive prestresses of 0, 3.5, 7, 10.5, and 14 MPa are shown in Figures 9-13, respectively. For the purpose of comparison, data for sample one are on the left of the page and sample two on the right. The B vs. H curve is at the top of the page, λ vs. H curve in the middle, and λ vs. B curve on the bottom.

Sample one showed a decrease in initial permeability and remanence as prestress increased, while magnetostriction and coercivity increased as prestress increased, see Figures 10-13. The field at which the maximum rate of change of magnetic induction with field occurs, increased as the prestress increased and became much larger than the coercivity at large compressive prestresses. The hysteresis curve (B vs. H) exhibited a distortion near the origin at higher prestress. It was also noted that there was a small negative strain of about -20×10^{-6} at low fields in the λ vs. H curve which depended
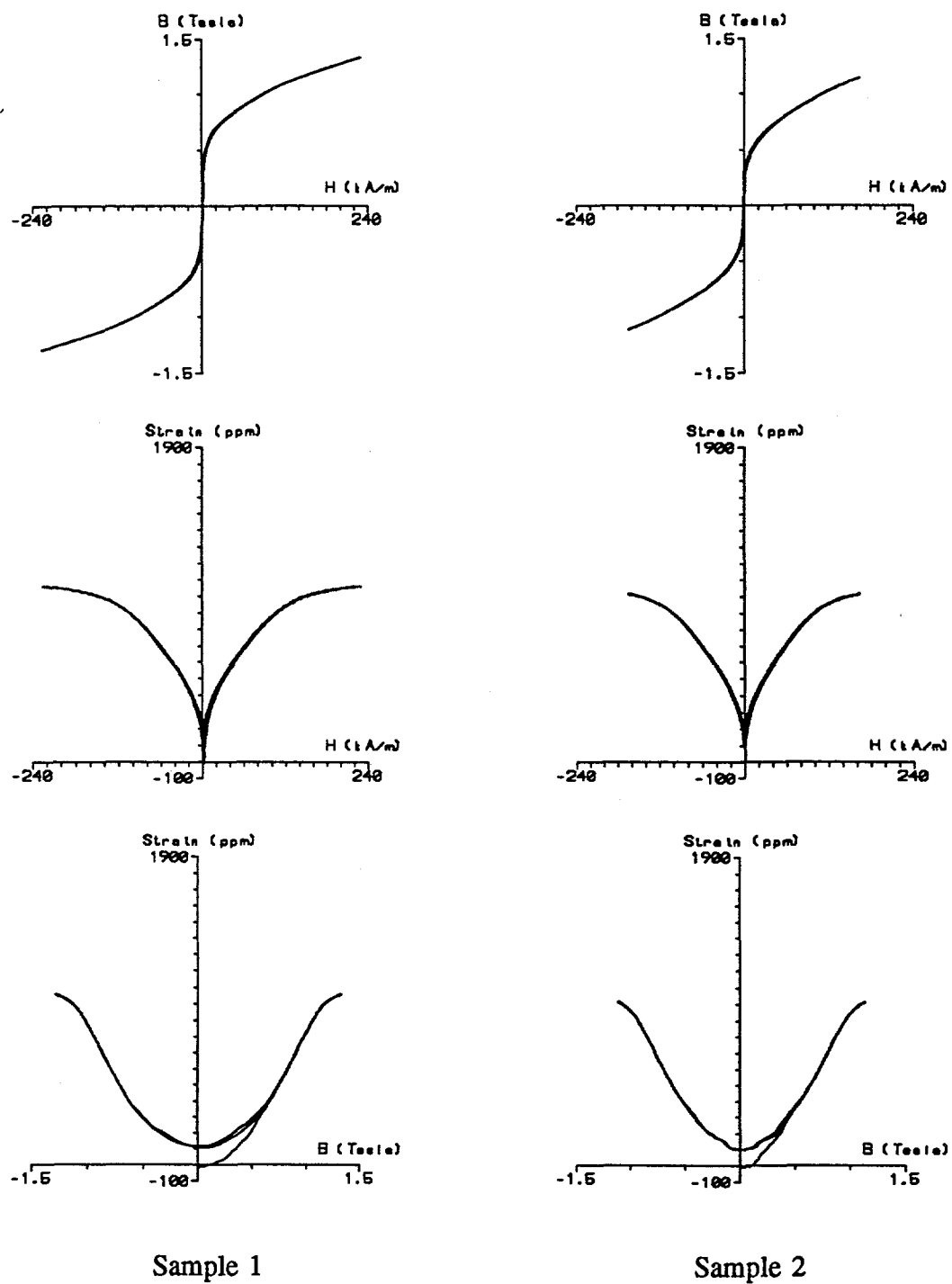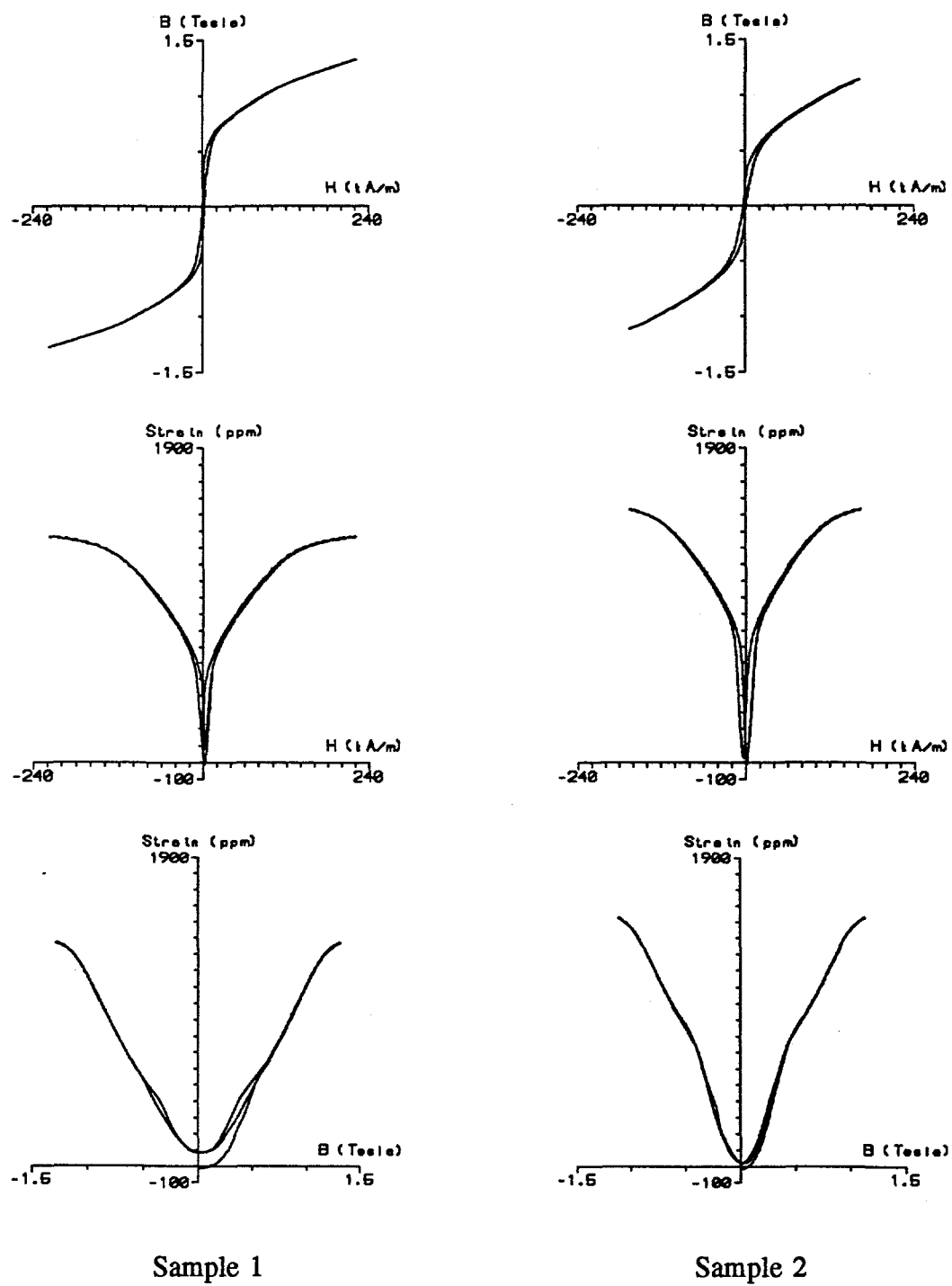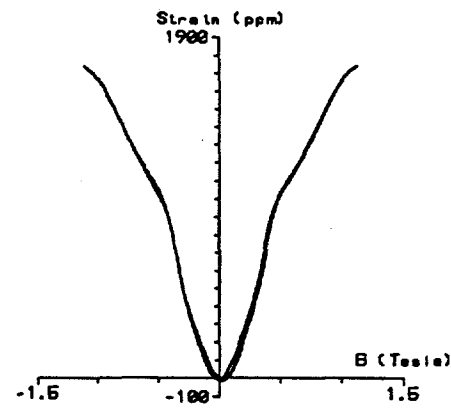
Sample 1   Sample 2

Figure 9. 0 MPa

38

Sample 1   Sample 2

Figure 10. 3.5 MPa
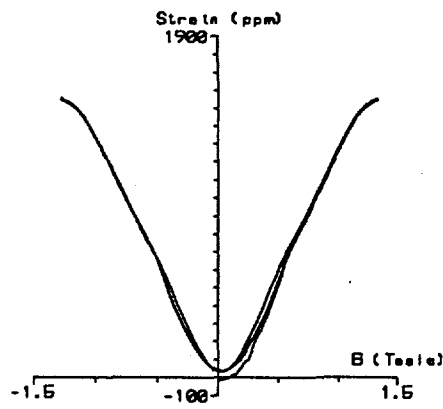
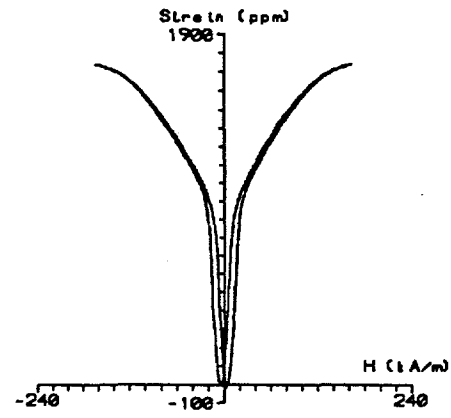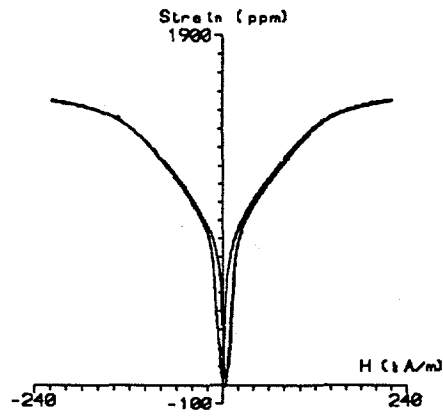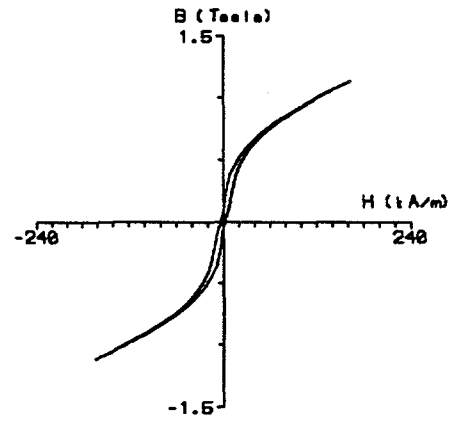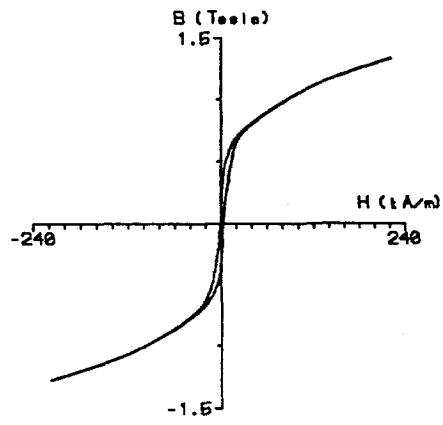Figure 11. 7 MPa

Sample 1   Sample 2

Figure 12.   10.5 MPa
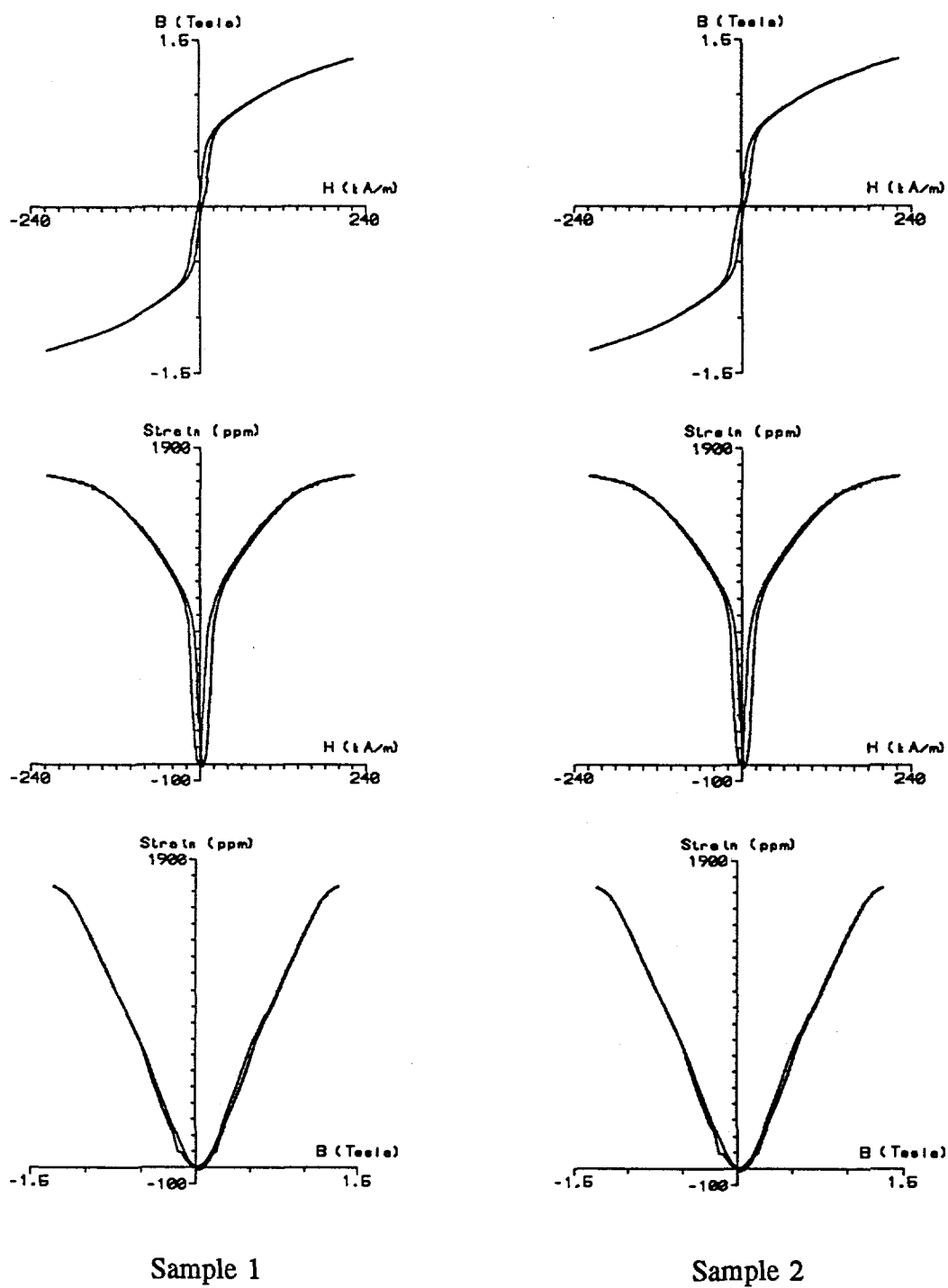
Sample 1   Sample 2
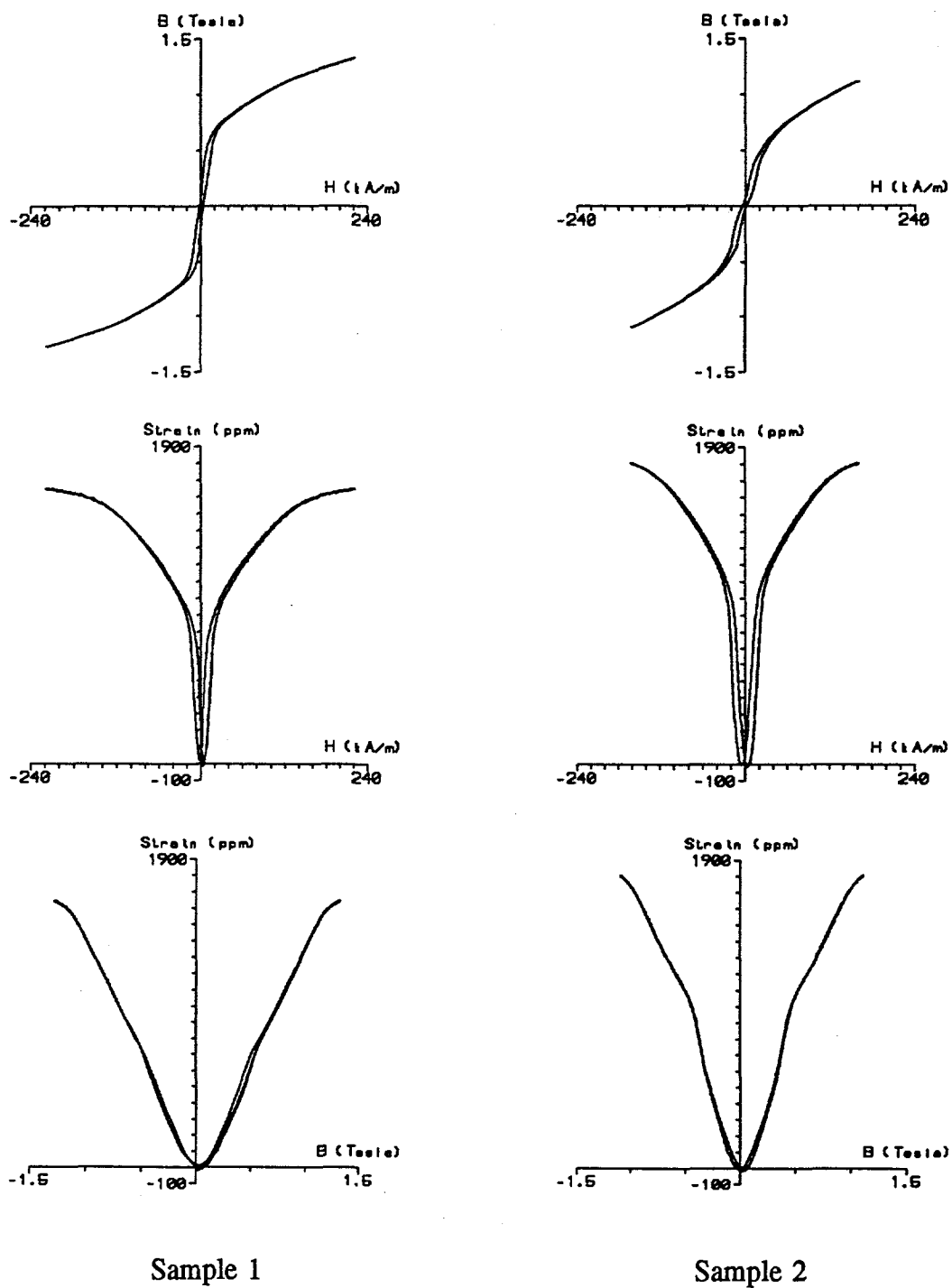
Figure 13. 14 MPa

strongly on the initial magnetocrystalline anisotropy and applied prestress. Maximum strain increased by a large amount with prestress, and the "burst effect" occurred for prestresses up to 14 MPa, see Figures 10-13.

The data for samples three, $Tb_{0.27}Dy_{0.73}Fe_{1.95}$, and four, $Tb_{0.3}Dy_{0.7}Fe_{1.95}$, at compressive prestresses of 0, 3.5, 7, 10.5, and 14 MPa are shown in Figures 14-18. The plots for sample three are shown on the left side of the page with B vs. H, λ vs. H, and λ vs. B curves on the top, middle, and bottom of the page, respectively. The data for sample four are shown on the right side of the page in the same format.

The hysteresis curve for sample three showed a decrease in remanence with increased compressive prestress. The maximum strain in sample three increased only a small amount (100×10^{-6}) as prestress was increased. Less hysteresis was also observed in sample three ($Tb_{0.27}Dy_{0.73}Fe_{1.95}$) as compared to sample four ($Tb_{0.3}Dy_{0.7}Fe_{1.95}$). There was also a slow change in the slope of the magnetostriction curve of sample three (ie. no "burst effect") and little or no negative strain.

Sample four displayed increased hysteresis in the λ vs. H curve with increased prestress. There was a significant decrease in the remanence in the B vs. H and λ vs. H curves with increased prestress. A prestress of 14 MPa resulted in a 500×10^{-6} increase in maximum strain from 1000×10^{-6} in the zero prestress state, see Figures 14 and 18. The remanent strain decreased as the prestress increased. There was an increased maximum slope of the λ vs. B curve as pressure increased. Table 3 summarizes the experimental results obtained for samples three and four.

Sample 3   Sample 4
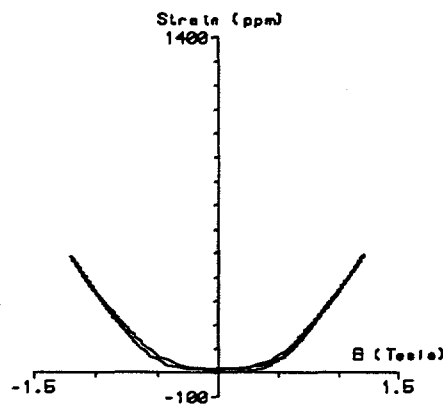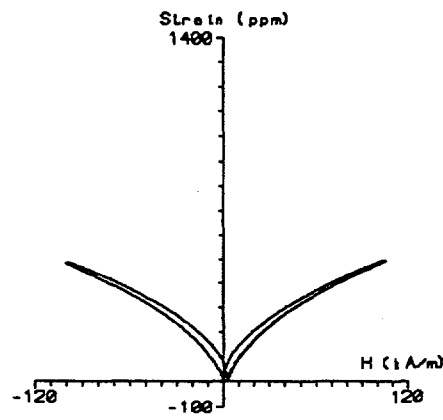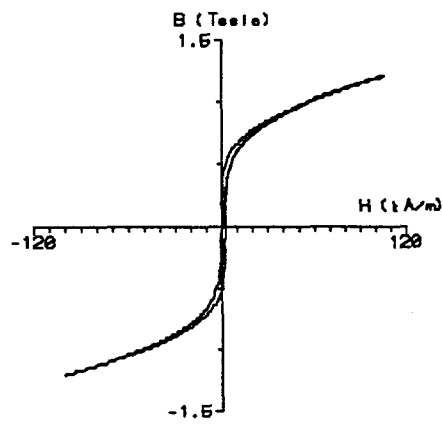
Figure 14. 0 MPa
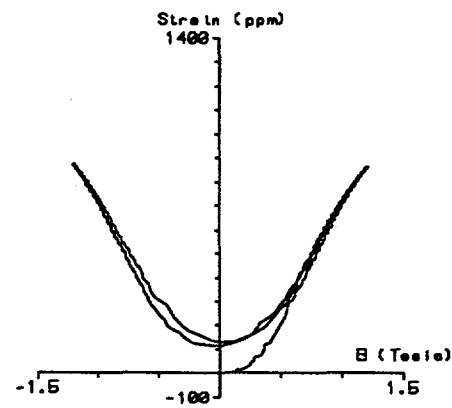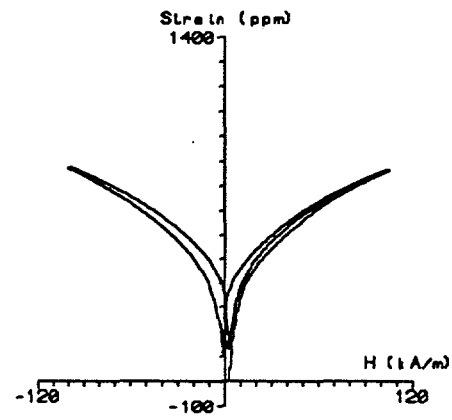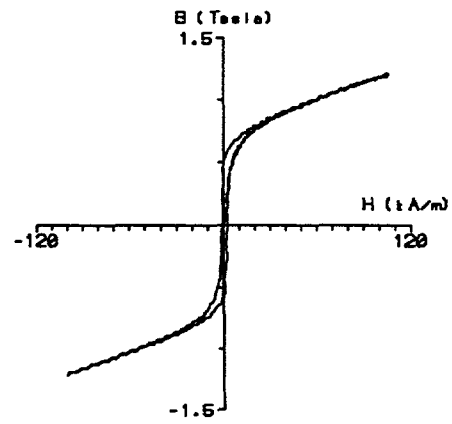
Sample 3   Sample 4
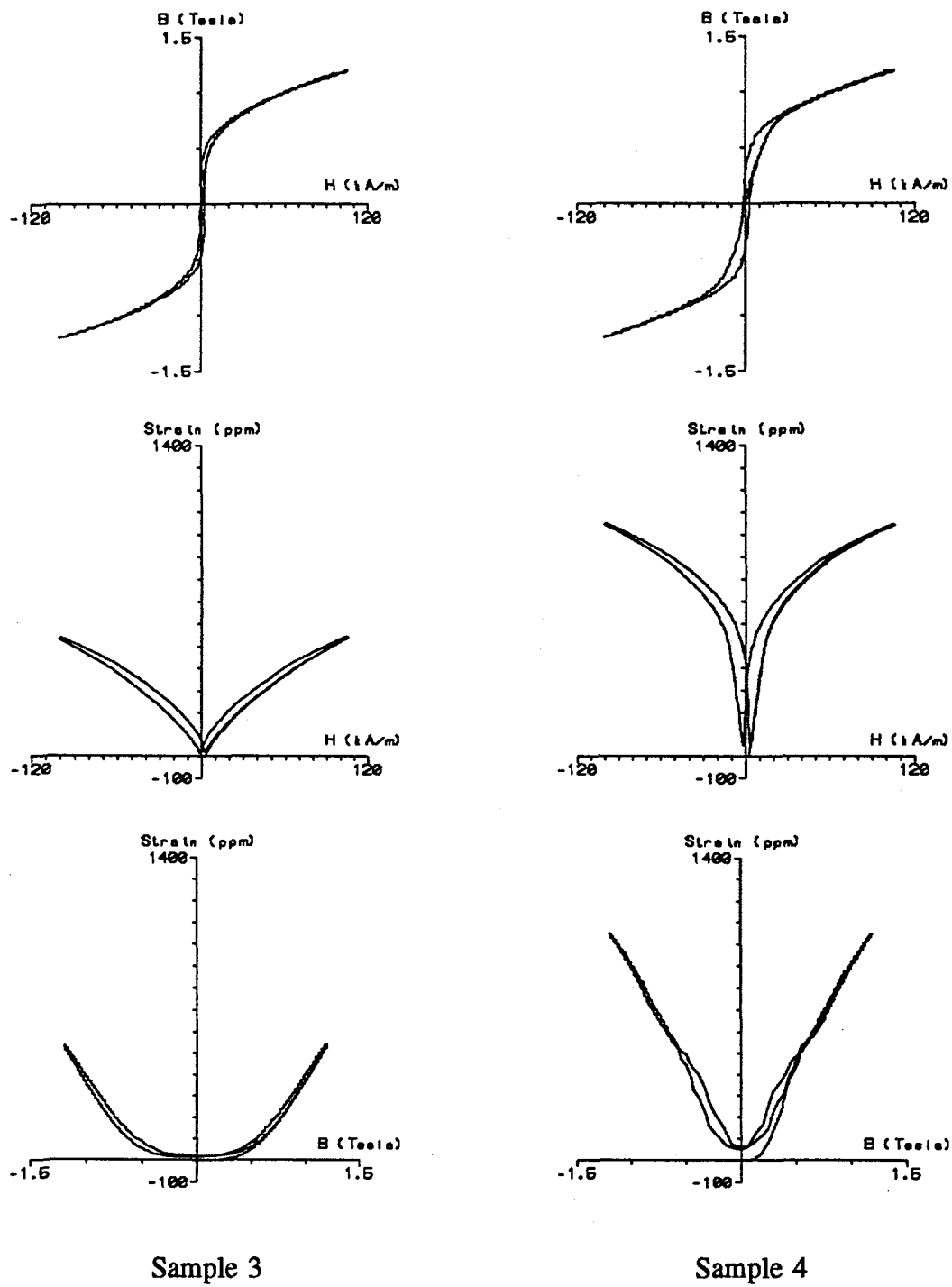
Figure 15. 3.5 MPa
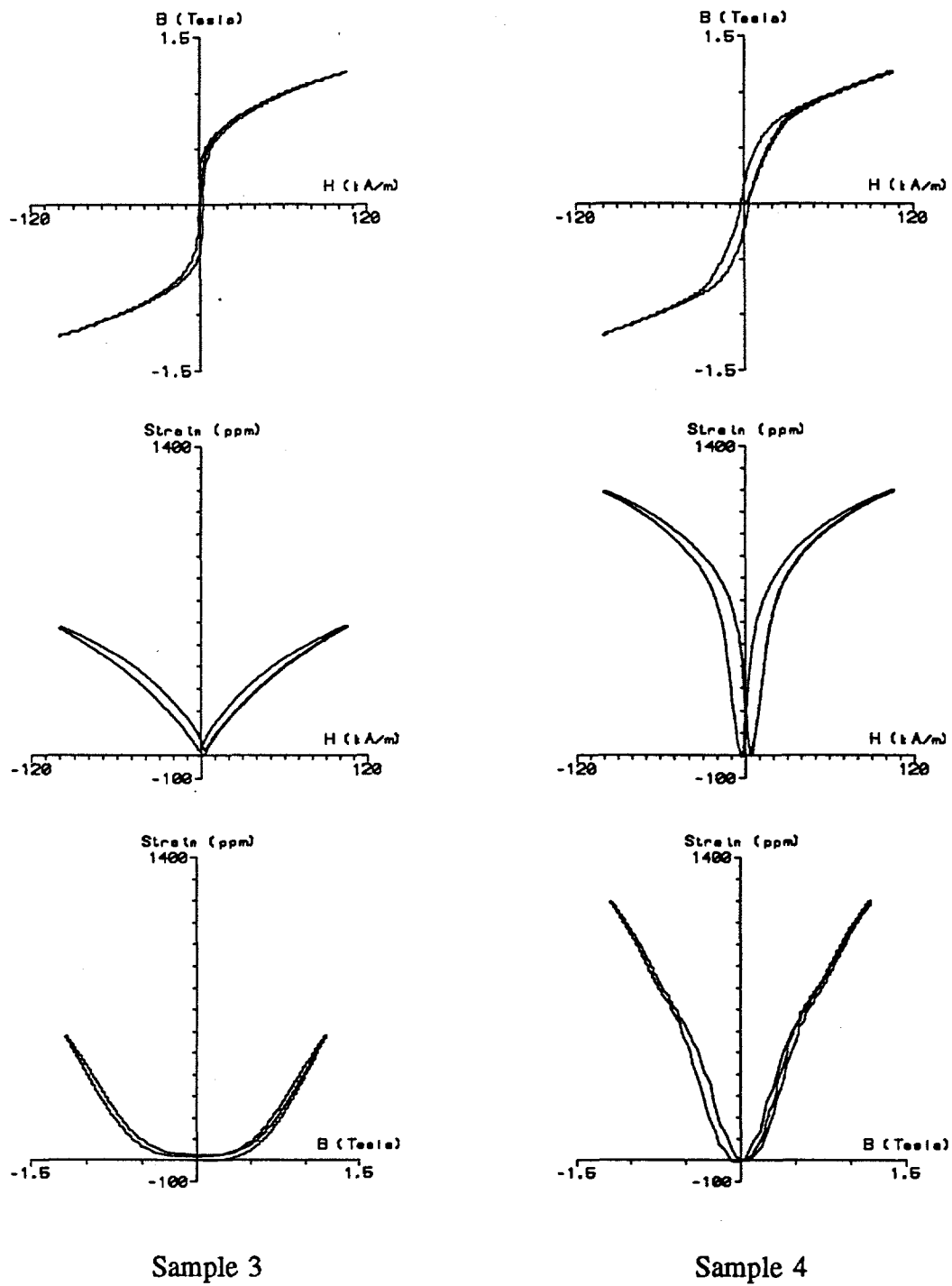
Sample 3   Sample 4

Figure 16. 7 MPa
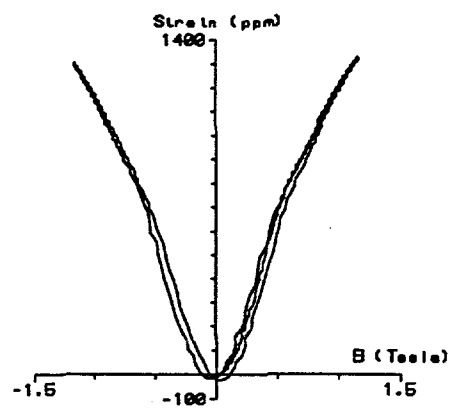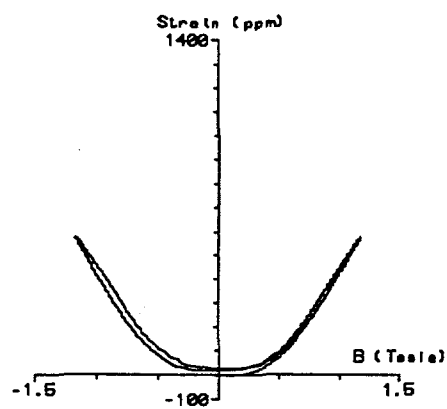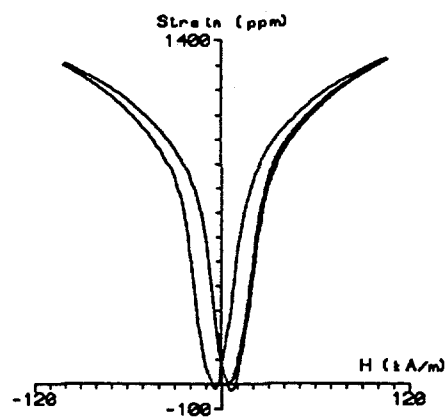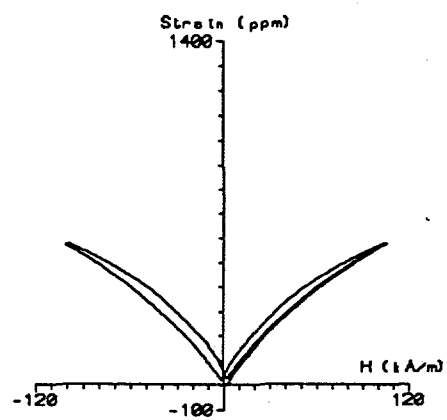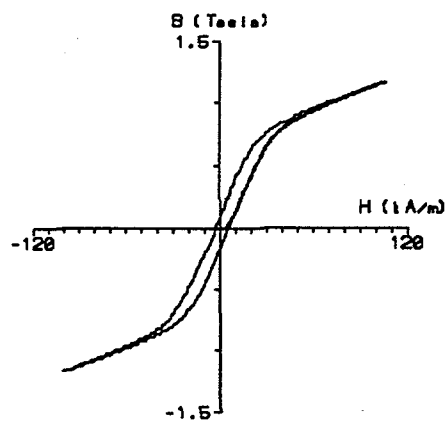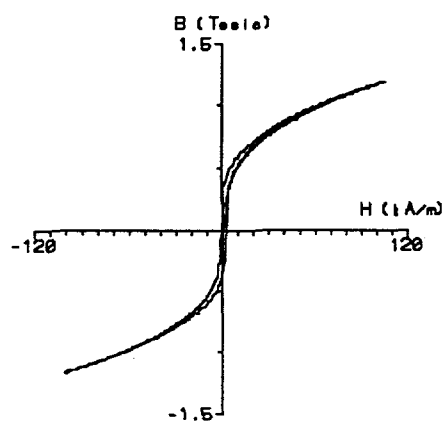
Sample 3   Sample 4

Figure 17. 10.5 MPa
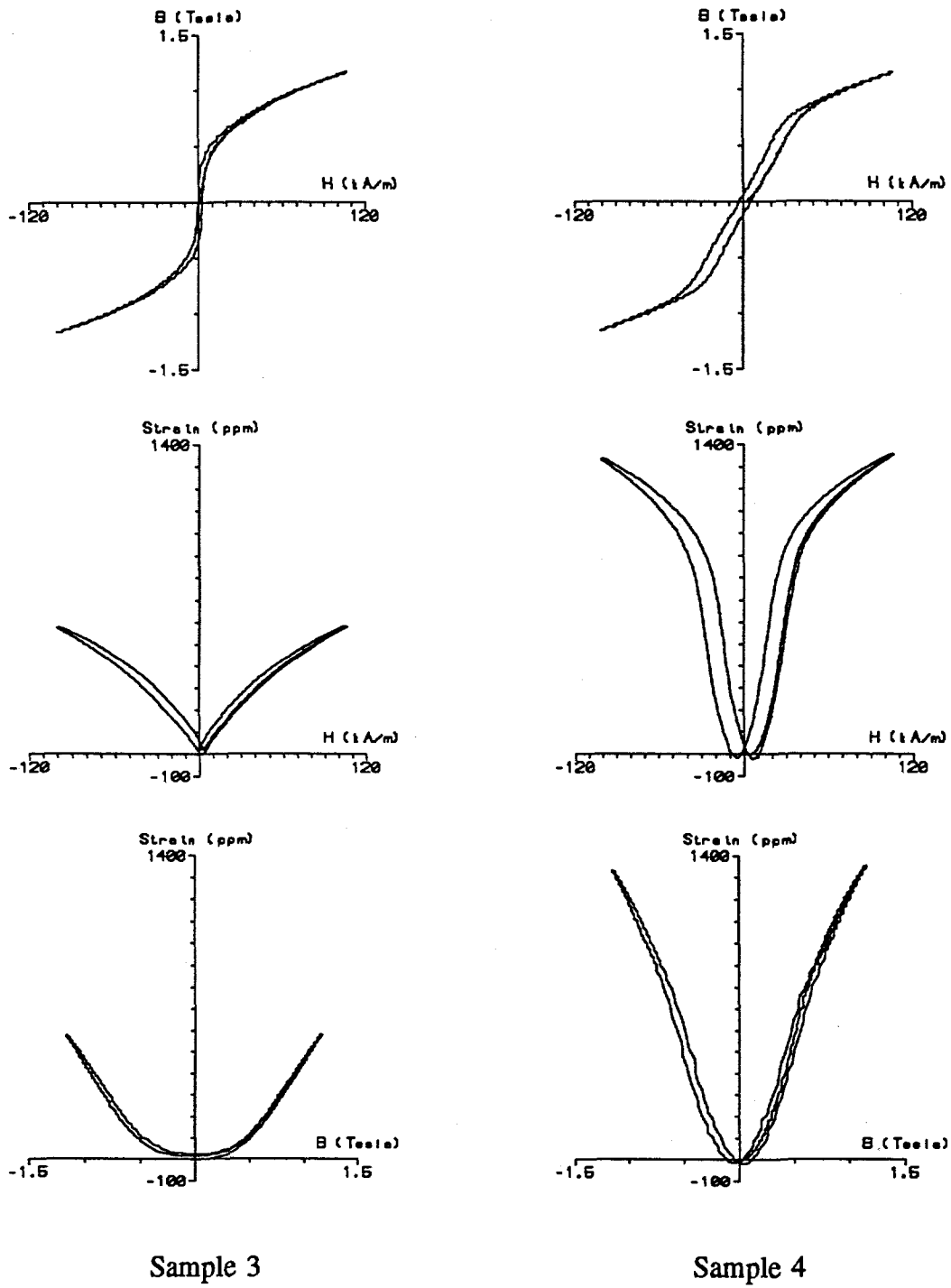
Sample 3   Sample 4

Figure 18.   14 MPa

Table 3. Summary of magnetic properties for samples 3 and 4

		λ_{max} (10^{-6})	d_{33} (nm/A)	H_d (kA/m)	μ_{33}	H_μ (kA/m)
S	0 MPa	495	13.1	6.4	103.3	1.54
a m	3.5 MPa	549	11.8	6.7	109.6	2.24
p l	7 MPa	592	12.4	3.9	96.1	0.90
e	10.5 MPa	594	11.5	4.9	91.9	2.55
3	14 MPa	597	11.0	6.9	71.2	2.90
S	0 MPa	901	64.0	3.8	108.8	2.50
a m	3.5 MPa	1065	56.6	7.2	58.4	1.93
p l	7 MPa	1204	62.3	14.2	29.9	10.65
e	10.5 MPa	1328	57.7	21.2	25.6	15.78
4	14 MPa	1357	48.4	24.4	21.6	23.81

Discussion

Samples one and two were cut from the same rod and displayed very similar

magnetic behavior as expected. The main difference between the two samples was the

microstructure. Sample one had a few misaligned grains which created an additional

internal stress in the material, whereas sample two was grain oriented throughout. The

region in sample one with the misaligned grains reduced the maximum strain and

increased the residual stress of the material. This difference in the microstructure made

the effects of stress on the magnetic properties of sample one less pronounced than in sample two.

The B vs. H curves of samples one and two at zero prestress displayed a large increase in magnetic induction of about 0.7 Tesla at an applied field of 1-2 kA/m. The induction gradually approached a saturation value near 1.2 Tesla. The large increase in induction at low fields can be attributed to 180° domain wall motion. Moments flipping 180° into a direction closer to the field direction will significantly increase the bulk magnetic induction without changing the magnetostriction. The gradual approach towards saturation can be explained by a reversible rotation of domains, whereas the large increase in magnetic induction could be due to irreversible domain wall motion.

As the applied prestress increased, the maximum change in magnetic induction with field for samples one and two decreased along with the remanence. The amount of 180° wall motion was reduced with applied prestress and the majority of magnetic processes were rotational. The resulting distortion near the origin of the B vs. H curve due to the additional anisotropy created by the applied prestress which inhibited domain wall motion was most evident in sample two at 10.5 MPa. The shape of the hysteresis curve can be described by a rotation of the domains from the [111] and [$\bar{1}\bar{1}\bar{1}$] directions at right angles to the direction of applied stress and field, first into the <111> direction 61° from the [11$\bar{2}$] direction and then into the [11$\bar{1}$] direction 19.5° from the applied field. The domains at higher field strengths rotated gradually into the field direction as the saturation value of the magnetic induction was reached. As the magnetic field was decreased from saturation, the majority of domains rotated back to a position 90° to the

applied field and stress, thereby reducing the remanence to almost zero.

The magnetostriction curve at no prestress for $Tb_{0.3}Dy_{0.7}Fe_{1.9}$ exhibited a saturation magnetostriction around 1000×10^{-6}. The increase near saturation was gradual and due mostly to domain rotation. As the magnetic field was decreased to zero, a remanent strain remained which was due to an irreversible reorientation of magnetic domains towards the <111> magnetic easy axes in Terfenol-D. Immediately after the field switched directions, the bulk magnetostriction dropped to a minimum as a result of the majority of magnetic domains aligning almost at right angles to the applied field.

The saturation magnetostriction increased with the application of prestress. For example at 14 MPa, the saturation magnetostriction was around 1900×10^{-6}, almost double the saturation value with no prestress applied. The measured magnetostriction depends heavily on the initial configuration of domains, since the bulk magnetostriction is taken to be zero in the demagnetized state, and an applied stress has the effect of reorienting the initial domain structure in Terfenol-D.

In the case of $Tb_{0.3}Dy_{0.7}Fe_{1.9}$ even the application of 3.5 MPa prestress has profound effects on the shape of the magnetostriction curve, see sample 2 in Figure 10. An almost discontinuous change in magnetostriction was observed for an applied magnetic field of less than 10 kA/m. This effect, displayed in the large values of d_{33}, is commonly referred to as the "burst effect", and can be explained by the spontaneous irreversible rotation of domains from one magnetic easy axis to another. As the amount of prestress increased, the "burst effect" occurred at higher fields. At 10.5 MPa, the "burst effect" occurred near 20 kA/m in sample 2, which is nearly double the required field at zero

prestress.

After the occurrence of the "burst effect," a slower rise in the magnetostriction was measured which was due to a continuous magnetization process. An applied compressive stress increases the internal energy around and along the direction of applied stress. The domains are unable to flip from one easy axis to another as they approach the direction of applied field and stress. Instead a gradual reorientation of the domains occurs until saturation is reached. The gradual rise in magnetostriction can be attributed to a rotation of the domains into the <111> direction closest to the applied field followed by a rotation into the field direction towards saturation. As the magnetic field is returned to zero from saturation, a remanent strain occurs. For example, in sample 2 at 10.5 MPa, the remanent strain, a result of the difference between the zero field domain configurations before and after the application of a magnetic field, was less than 100×10^{-6}. As prestress increases, the remanent strain decreases because the domains will prefer to orient 90° to the applied stress at zero field.

In $Tb_{0.3}Dy_{0.7}Fe_{1.9}$, a negative strain can be observed at low fields in some cases when a field and prestress are applied along the [11$\bar{2}$] direction. A negative strain denotes a contraction in the length of the sample with respect to the initial length instead of an elongation. The initial orientation of domains plays an important role in the observed magnetostriction. Domains oriented initially at angles greater than 90° to the applied field and stress will rotate into a direction closer to the applied field as the field increases. If the new orientation is still at an angle greater than 90° with respect to the field direction, a rotation through 90° will cause a contraction of the material.

Certain magnetic processes have different effects on the magnetic induction and magnetostriction. For example, a 180° domain process can significantly increase the magnetic induction, but has no effect on the magnetostriction, while a 90° domain process increases both the induction and magnetostriction. Therefore, plots of magnetic induction versus magnetostriction can reveal where these different processes occur on the B vs. H and λ vs. H curves.

At no prestress, the λ vs. B curve for $Tb_{0.3}Dy_{0.7}Fe_{1.9}$ shown in Figure 9 has an approximately parabolic shape, $\lambda \propto M^2$.[5] The change in strain is very small at magnetic inductions of less than 0.25 Tesla, where 180° domain processes predominate. A more significant but gradual increase in strain results at higher values of magnetic induction. One explanation is 71° and 109° domain wall movements, because an irreversible rotation of domains would produce a sharper change in strain. As Terfenol-D approaches saturation, it is more likely that the slight increase in strain is due to a coherent rotation of domains from the <111> direction 19.5° from the field direction into the field axis.

The λ vs. B curve takes on a 'v-shape' as prestress is applied. The 180° processes have almost disappeared at prestresses of 3.5 MPa and above due to stress anisotropy and are replaced by non-180° rotational processes which contribute to the observed magnetostriction. At low fields, the λ vs. B curve for sample two in Figure 10 shows a large increase in strain compared to a small increase in magnetic induction. However, at higher field strengths larger increases in both strain and induction are observed. The magnetic processes responsible for these two regions of the λ vs. B curve are different. At 14 MPa prestress, as shown in sample two in Figure 13, the increases in strain and

magnetic induction are uniform and occur simultaneously. As can be seen in sample two in Figure 10 there are at least two main contributions to the large bulk magnetostriction. The first large increase in strain at lower magnetic induction is due to a rotation of domains from one <111> easy axis to another which lies closer to the direction of applied field. The second increase in strain is not as sharp but can be explained by a rotation of domains into the <111> direction closest to the field direction. In comparing the λ vs. B plots for sample two in Figures 9 and 10, it is evident that a small amount of prestress significantly reduces the remanent strain.

Neither magnetization nor magnetostriction processes in a material are separable. In $Tb_{0.3}Dy_{0.7}Fe_{1.9}$, a stress applied along the $[11\bar{2}]$ direction alters the internal energy of the material and affects the observed magnetic properties. In comparing the results of samples three and four, it can be seen how a small change in ratio of terbium to dysprosium changes the bulk magnetic properties.

An applied stress changes the initial orientation of magnetic domains in a material by altering the internal energy. Therefore the initial configuration of magnetic domains plays an important part in determining the observed magnetostrictive properties of a material. The results on applying a prestress to the $Tb_{0.3}Dy_{0.7}Fe_y$ composition of Terfenol-D with y = 1.9 or 1.95 shows profound effects on magnetic properties but prestress has hardly any effect on the magnetic properties of the $Tb_{0.27}Dy_{0.73}Fe_{1.95}$ Terfenol-D composition, see sample three in Figures 14-18.

The magnetization vector prefers to orient itself along a crystallographic direction which has a minimum in the internal energy of the material. This energy includes the

sum of magnetocrystalline anisotropy, stress anisotropy, and field energy. As the stress is increased, the internal energy becomes a minimum at right angles to the applied stress. The internal energy along the direction of the applied stress increases making it less easy for the magnetization to increase rapidly at low field strengths, and therefore decreases the initial permeability. In addition, the remanence decreases because the magnetization vectors will prefer to orient themselves at right angles to the field direction, reducing the component of the magnetization along the field direction.

For the purposes of applications, the most important difference between the two different compositions that were tested is the presence of the 'burst effect' in the sample with composition $Tb_{0.3}Dy_{0.7}Fe_y$ where $y = 1.9$, 1.95 and the lack of this effect in the $Tb_{0.27}Dy_{0.73}Fe_{1.95}$ sample.

Variations in the growth process of Terfenol-D can greatly effect the observed magnetostrictive properties. For example samples two and four have the same composition of Tb and Dy atoms, but the maximum strain of sample two is $\approx 1900 \times 10^{-6}$ at 14 MPa, whereas the maximum strain of sample four is only $\approx 1400 \times 10^{-6}$ at 14 MPa. The difference in maximum strain which is due to grain misalignments, variations in grain size, and vartions in composition along the length of the sample due to zone refinery is the result of variations in the production of the two samples. A comparison of the magnetic properties of both compositions is summarized in Table 3.

Many problems still exist for using Terfenol-D in engineering devices. The hysteresis in the magnetostriction poses a problem when a specific strain needs to be produced. The $Tb_{0.27}Dy_{0.73}Fe_{1.95}$ composition of Terfenol-D which displays the least

hysteresis also has the lowest maximum slope of the magnetostriction curve, d_{33}, which is important in the conversion of magnetic energy to mechanical energy. In addition, there has yet to be a method of mass producing Terfenol-D rods. Larger diameter rods which can be used under heavier loads have to be produced in such a way that they sometimes display cracks on their surfaces which can adversely affect their magnetic and mechanical properties.

THEORETICAL FIELD DEPENDENCE OF MAGNETIZATION AND MAGNETOSTRICTION

Hysteresis Models

Many theories exist that attempt to describe observed magnetic phenomena. Some are based purely on physical laws and others give a phenomenological approach to the problem. Still a theory has not been developed that can account for all the complexities of hysteresis, domain wall motion and domain rotation, and magnetostriction. Before a new theory can be developed to describe the large change in magnetostriction and effect of stress on the hysteresis curve in Terfenol and similar materials, it is important to understand what other models currently exist. An overview is given of three comprehensive models of magnetic hysteresis commonly cited in the literature.

Preisach model

A phenomenological model was developed by Preisach[34] in 1935 based on the hypotheses concerning the physical mechanisms of magnetization under the action of an applied magnetic field. The model is characterized by an input function $u(t)$ which represents the magnetic field and an output function $f(t)$ representing the magnetization. The scalar Preisach model is constructed by the superposition of the simple hysteretic operator $\gamma_{\alpha\beta}$ representing rectangular hysteresis loops with α and β as the "up" and "down" switching fields, respectively. Considering an infinite set of these operators and a

weight function given by $\mu(\alpha,\beta)$, the Preisach model can be defined by the following integral.

$$f(t) = \int\int_{\alpha \geq \beta} \mu(\alpha,\beta)\gamma_{\alpha\beta}u(t)\,d\alpha\,d\beta \qquad (15)$$

The function $\mu(\alpha,\beta)$ is determined for a given material by matching experimentally measured first-order transition curves. The classical Preisach model is purely mathematical and can be used to describe the static field properties of hysteresis.[35]

It is important to include the effects of stress when modelling Terfenol because most applications of Terfenol require an applied prestress in order to maximize the mechanical work output while minimizing the power input. A small prestress of 3.5 MPa significantly increases the change in magnetostriction with applied field for the $Tb_{0.3}Dy_{0.7}Fe_y$ composition with $1.8 < y < 2.0$. The Preisach model has been used effectively to model experimental magnetization and magnetostriction curves for Terfenol under prestress.[36] The model can be useful in helping to design devices because its output is closely related to actual experimental output. This model gives no physical insight into the origin of magnetic properties nor does it explain the effect of stress on the magnetization and magnetostriction.

Jiles-Atherton model

In 1986, Jiles and Atherton published their theory on ferromagnetic hysteresis.[37] The theory is based on domain wall motion. As a domain wall moves through a material,

it becomes anchored to pinning sites within the material which inhibit its ability to move further. Both bending and translation of the domain wall are considered. Theoretical results from the model are able to reproduce the initial magnetization curve along with hysteresis loops which are asymmetric or symmetric with respect to 180° rotation about the origin of the M,H plane.

Equations of magnetization are derived by Jiles and Atherton by considering different energy contributions in ferromagnetic materials and their corresponding effect on the resulting magnetization. Each domain is assumed to interact with neighboring domains and with the internal magnetization of the domain itself, based on the mean field approximation. Simplifications to the mathematics of the theory are made by assuming a uniform distribution of pinning sites and small displacements of the domain wall as it bends. No distinction is made between different types of pinning sites. Instead they are all assumed to behave like non-magnetic inclusions with a mean pinning energy per site. The energy required to overcome domain wall pinning between two sites is assumed to be proportional to the change in energy per volume of magnetization in one domain due to the rotation into the field direction of moments in that domain.

According to Jiles and Atherton, three factors are assumed to affect the bending of domain walls:

1) the surface energy of the wall
2) the strength of the pinning sites
3) the tendency of the magnetization of the material to lie on the anhysteretic magnetization curve, a magnetization curve exhibiting no hysteresis

The theory uses four variable parameters which can be determined experimentally

to define the form of the magnetization curve. The parameter, a, represents the domain density and controls the shape of the anhysteretic curve, α defines the coupling between neighboring domains, k represents the average energy per pinning site in the material, and c denotes the amount of bending allowed before a wall is able to break away from a pinning site.

$$\frac{dM}{dH} = \frac{(1 - c)(M_{an} - M_{irr})}{[k\delta - \alpha(M_{an} - M_{irr})]} + c\frac{dM_{an}}{dH} \tag{16}$$

here M_{an} denotes the anhysteretic magnetization, M_{irr} the irreversible magnetization, H the magnetic field, and δ (= ±1) the direction of the change in magnetic field. The theory of ferromagnetic hysteresis applies to isotropic materials such as polycrystals but can also work well in modelling single crystal materials with low anisotropy.

The theory is based on a set of clearly defined physical laws which specify how a domain wall moves through a material. In addition to generating hysteresis curves, the model has been extended to describe magnetostriction curves as well.[38]

Stoner-Wohlfarth model

The magnetic behavior observed in low and moderate fields can be attributed to domain wall movement whereas the rotation of magnetic domains into the field direction is thought to dominate the high-field magnetic behavior. Only rotational processes can describe the very high coercivities that are found in some materials, such as permanent magnets. Stoner and Wohlfarth developed a theory based on rotational magnetization

processes occurring in anisotropic materials.[39] The model assumes that the material is composed of non-interacting single domain ellipsoidal particles which exhibit a larger demagnetizing factor along the short axis than along the long axis leading to shape anisotropy. The assumption of single domain particles simplifies the mathematics and implies that the shape and size of the particles are such that domain boundary formation is excluded.

The sum of the energy due to the shape of the particles and the applied magnetic field is minimized in order to determine the orientation of the magnetization vector with respect to the measurement direction. The magnitude of the change in resolved magnetization for one particle is $M_s(\cos\phi_o' - \cos\phi_o)$ when the direction of the magnetization changes from an angle of ϕ_o to an angle of ϕ_o' with respect to the measurement direction at static values of the magnetic field. Magnetization curves are calculated in two steps. First, a mean value of the magnetization is calculated for an assembly of similarly shaped ellipsoids. Second, three distinct orientations of the ellipsoid are considered with each of the three axes of the ellipsoid oriented in the plane of the applied field and randomly combined to simulate a real material.

A set of values is calculated for the resolved magnetization as a function of field for a suitable series of orientations of the polar axis of the ellipsoid relative to the field. A procedure is adopted to evaluate h, a unitless parameter denoting the normalized magnetic field strength, directly for values of ϕ at suitable intervals of θ, for decreasing h. From the descending results, values of ϕ for particular values of h may be found by inverse interpolation. The ascending curve is obtained through symmetry.

The integral

$$\overline{\cos\phi} = \frac{M}{M_s} = \int_0^{\frac{\pi}{2}} \cos\phi \sin\theta \, d\theta \tag{17}$$

must be evaluated numerically, except for a few special cases, to calculate the mean value of the resolved magnetization M/M_s for random orientations of the magnetization and a given value of h, where M_s represents the saturation value of the magnetization. The angle between the magnetic field and magnetization is represented as ϕ in the integral[39], and

$$\phi = \theta + \psi \tag{18}$$

where θ denotes the angle between the polar axis of the ellipsoid and the magnetic field, and ψ the angle between the polar axis of the ellipsoid and the magnetization. The calculations can not be performed if the magnetization vector is not in the same plane as the applied field.

There may be more than one direction of magnetization for which the energy is a minimum for certain field values, therefore the direction taken must be consistent with past history. In this case an energy minimum requires that at least one of the three directions be a minimum.

The formalism for a general ellipsoid covers a wide variety of possible particle

spherical particle. For ellipsoids with three unequal axes, hysteresis effects will always occur. However, Stoner and Wohlfarth found that hysteresis and coercivity decreased as the two longer axes of the ellipsoid became more equal. For large hysteresis and coercivity the theoretical requirement becomes that one of the principal axes must be considerably longer than the other two, when only the shape of the particle is considered to effect hysteresis.

The Stoner-Wohlfarth model suggests the physical reality of a more strongly ferromagnetic phase embedded in a less strongly ferromagnetic matrix. It works best when applied to non-ferromagnetic metals and alloys that contain ferromagnetic "impurities" such as powder magnets, and high coercivity alloys of the dispersion hardening type. The results are not relevant to Terfenol-D which exhibits low hysteresis and coercivity.

The three models described here are fundamentally different but fail to describe the negative strains observed in Terfenol. A fundamental model needs to be developed in order to gain a better understanding of the magnetic processes responsible for the observed magnetic properties of Terfenol. The Preisach model has little physical basis and does not give any further insight into the magnetic processes responsible for the bulk magnetic properties in Terfenol. The theory of ferromagnetic hysteresis does not describe adequately the hysteresis curve of Terfenol. Better agreement however is found when describing the magnetostrictive phenomena under prestress. The almost discontinuous change in strain observed in Terfenol can be attributed to the rotation of magnetic domains. The Stoner-Wohlfarth model is based on rotational magnetic processes. The

method used in the Stoner-Wohlfarth model to derive a magnetization curve by minimizing energy and following the part of a magnetization vector can be applied to describe the magnetic and magnetostrictive properties of Terfenol. A model was developed to describe the effects of rotational processes on the magnetic and magnetostrictive behavior of anisotropic materials subject to prestress where the magnetic field can be applied along any crystallographic direction and the magnetization can move in three-dimensions.

The Three-dimensional Anisotropic Rotation Model

A two-dimensional rotational theory based on the Stoner-Wohlfarth approach was developed to describe the observed magnetic phenomena in Terfenol but rotation was restricted to the (110) plane in the material to simplify the mathematics.[40] A three-dimensional model is more realistic in general and can be used for any material whose magnetic and magnetostrictive behavior depends on rotational processes. An introduction is given to the three-dimensional anisotropic rotation model.

Introduction

The three-dimensional anisotropic rotation model is based on rotational magnetic processes with no restrictions on the movement of the magnetization vector or the direction of applied field and stress. Domain rotation can be either reversible or irreversible. Within the confines of the model, a reversible rotation process is one in

irreversible. Within the confines of the model, a reversible rotation process is one in which the magnetization vector is initially oriented along a magnetic easy axis and a magnetic field is applied which moves the vector away from the easy axis but is not strong enough to move the moment into a different easy axis of lower energy. Therefore, when the applied field is removed, the magnetization vector returns to its initial orientation. An irreversible process is one that has enough energy applied to reorient the magnetization along another easy axis in the material in such a way that when the field is removed the magnetization stays oriented along the new local energy minimum.

The material is considered to be an assembly of domains, but does not include domain walls, since the model does not consider domain wall motion. Particles of this type are referred to as single domain particles, but unlike the Stoner-Wohlfarth model the shape of the particles is not considered. To simplify the mathematics, the single domain particles do not interact with each other.

The magnetization vectors are initially aligned along one of the eight <111> easy axes to simulate the initial orientation of magnetic domains in Terfenol under no field. As the magnetization vector moves in three-dimensions, the three angles specifying the position of the magnetization unit vector must satisfy

$$\alpha_1^2 + \alpha_2^2 + \alpha_3^2 = 1 \tag{19}$$

for the position to be valid, where α_i are the direction cosines of the magnetization vector.

Energy   The free energy used in the three-dimensional anisotropic rotation

model is a sum of the magnetocrystalline anisotropy energy, field energy, and the magnetoelastic energy. The form of the magnetocrystalline anisotropy energy depends on the crystal structure of the material. A cubic crystal anisotropy is assumed for simplicity even though it is known that the magnetostriction distorts the cubic crystal lattice in Terfenol. The energy due to crystal anisotropy[5] is given by

$$E_K = K_1(\alpha_1^2\alpha_2^2 + \alpha_2^2\alpha_3^2 + \alpha_3^2\alpha_1^2) + K_2\alpha_1^2\alpha_2^2\alpha_3^2 \qquad (20)$$

where K_1 and K_2 represent the first and second order anisotropy constants and α_i the direction cosines of the magnetization. The second order term in the energy is to the sixth power of a trigonometric function unlike the first order term which is just to the fourth power.

The second order term in the energy equation is ignored in this model to simplify the internal energy of the crystal. For Terfenol, K_1 = -60 kJ/m^3, which ensures that the eight <111> directions are the easy axes (ie. where the magnetocrystalline anisotropy energy is minimum), and K_2 = -140 kJ/m^3.[8]

The application of a magnetic field creates energy by coupling with the magnetization vector of the domain being considered. The energy[4] is given by

$$E_H = -\mu_o M_s H \cos\Omega \qquad (21)$$

where μ_o denotes the permeability of free space, M_s the saturation magnetization, H the magnitude of the applied magnetic field, and Ω the angle between the magnetization and

the applied field which is given by

$$\cos\Omega = \alpha_1\beta_1 + \alpha_2\beta_2 + \alpha_3\beta_3 \tag{22}$$

where α_i denotes the direction cosines for the magnetization and β_i the direction cosines for the magnetic field. The energy generated by the magnetic field is maximum when the magnetic field and magnetization are in opposite directions, and minimum when oriented in the same direction.

The energy due to the applied stress is referred to as the magnetoelastic energy[7] and can be given by

$$E_\sigma = \frac{3}{2}\sigma\lambda_{111}\sum_{i\neq j}^{3}\alpha_i^2\gamma_j^2 - 3\sigma\lambda_{100}\sum_{i\neq j}^{3}\alpha_i\gamma_i\alpha_j\gamma_j \tag{23}$$

where λ_{111} and λ_{100} are the magnetostriction constants, σ the applied stress, α_i the direction cosines of the magnetization, γ_i the direction cosines of the applied stress, and i,j denote the three crystallographic axes summed over ([100], [010], and [001]).

The method used to derive the magnetization and magnetostriction curves in the three-dimensional anisotropic rotation model relies entirely on locating the movement of a local energy minimum in three dimensions. The energy distribution of the crystal in three-dimensions is affected by properties of the crystal and externally applied variables such as the magnetic field and compressive stress. The different effects can be visualized in three-dimensional plots of the energy surface in Terfenol.

dimensional plots. The sum of the magnetocrystalline anisotropy energy, field energy, and magnetoelastic energy represents the relevant free energy of the crystal. The program calculates the free energy for all possible orientations of a magnetization unit vector in three-dimensions. The projection of the free energy along the [100], [010], and [001] axes is stored in the first, second, and third columns of a data file, respectively. Data files were generated for magnetic field values of 0-24 kA/m and applied compressive stresses between 0-14 MPa, where both the field and stress were applied along the [112] direction to simulate experiments on Terfenol. The three-dimensional plots were generated with the help of a commercial software package.

The initial magnetic state of any material is the unstressed state with no external magnetic field applied. The internal energy distribution of Terfenol with $K_1 = -60$ kJ/m^3 and no applied field or stress is shown in Figure 19. The orientation of the crystal axes is shown in Figure 20, and is the same for all the three-dimensional plots presented. The relevant free energy is represented by the radius vector which originates at the center of the plot and extends out to the surface of the three-dimensional plot. The location and value of the global energy minimum is noted in each plot for the sake of comparison.

For Terfenol, as can be seen in Figure 19, the internal energy is symmetric, having eight minima in the <111> directions which are the magnetic easy axes and six maxima in the <100> directions. The twelve intermediate values of the energy correspond to the <110> directions in the crystal. The ideal symmetry of this initial state results from the cubic anisotropy of the crystal considered.

It is important to understand the effect an applied magnetic field has on the shape
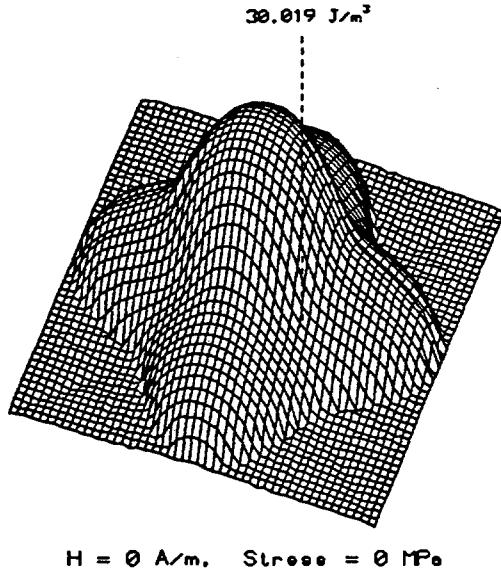
30.019 J/m³

H = 0 A/m, Stress = 0 MPa

Figure 19. Three-dimensional energy
surface
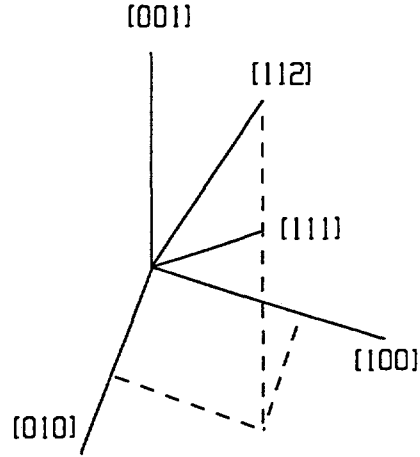

[001]

[112]

[111]

[100]

[010]

Figure 20. Crystallographic orientation
of three-dimensional plots

of the energy surface in the cubic crystal structure of Terfenol, see equation 20. Figure

21(a-c) shows the distortions in the energy surface caused by a magnetic field of strength

12, 16, and 24 kA/m, respectively, applied along the [112] direction. The energies at

angles less than 90° to the [112] direction decrease as the field increases making it less

favorable for magnetic moments to lie against the direction of the applied field.

The application of a compressive stress increases the maximum strain and d_{33}

coefficient in Terfenol. For a constant magnetic field strength of 24 kA/m, in the mid-

range of the magnetic field strengths where maximum d_{33} occurs, the effect of

progressively larger compressive stresses (3.5, 7, 10.5, and 14 MPa) applied along the

[112] direction on the three-dimensional energy surface is shown in Figure 22. As shown
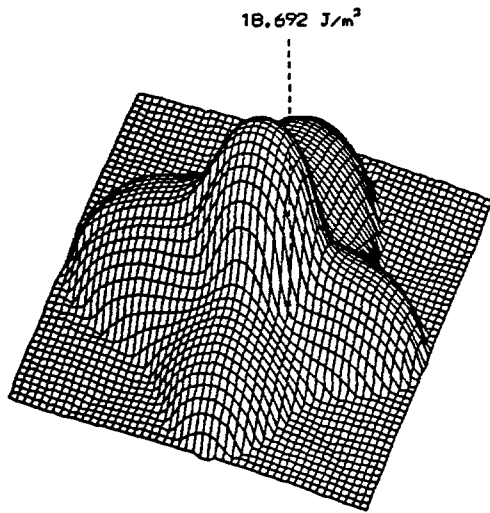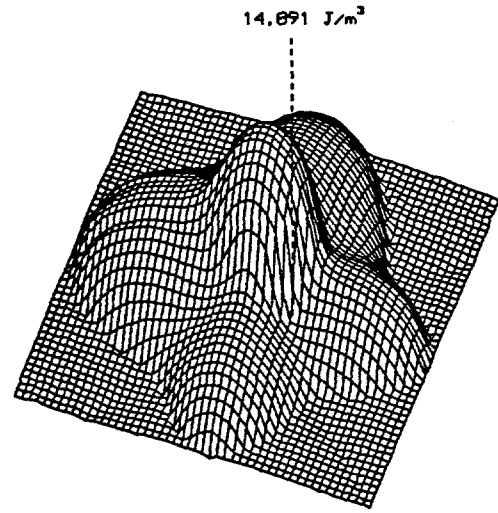
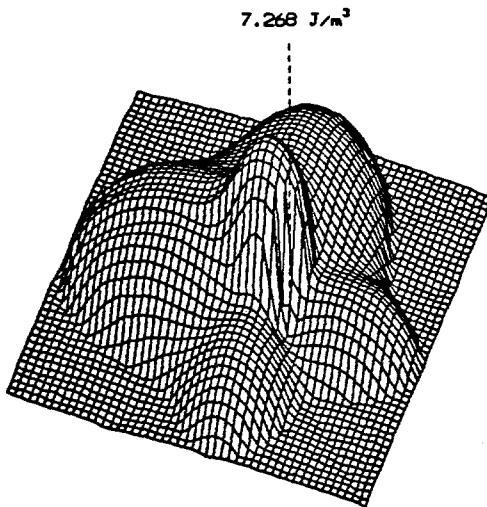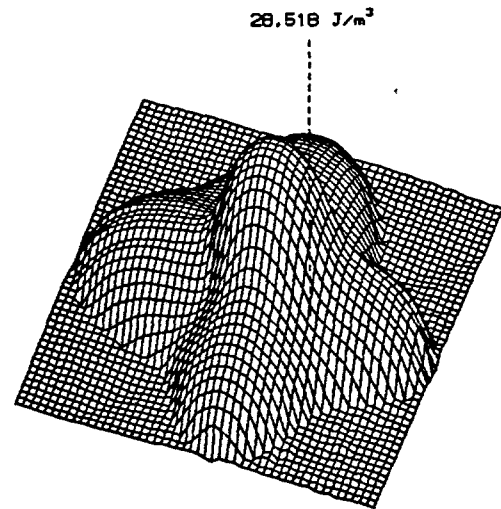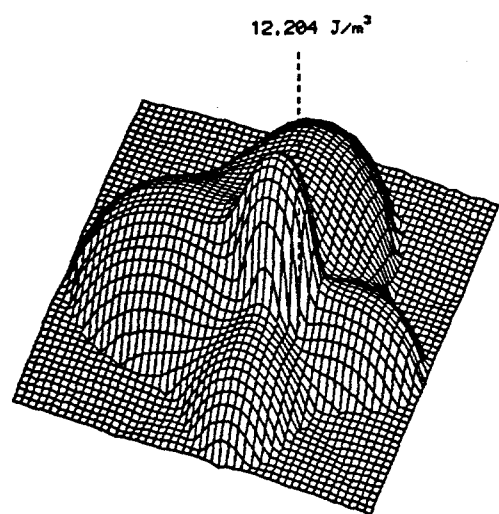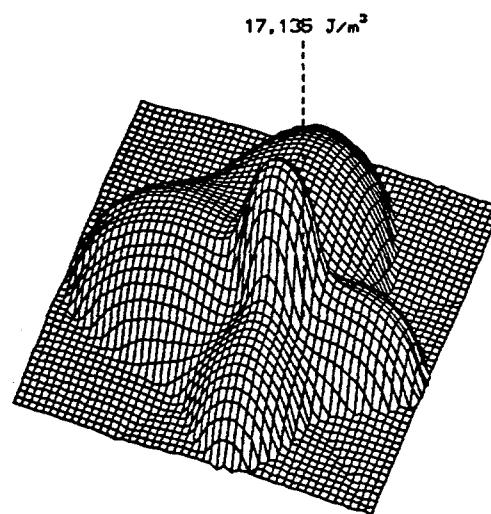Figure 21. Three-dimensional energy plots at zero stress for 12 kA/m (a), 16 kA/m (b), and 24 kA/m (c), and at 7 MPa for 12 kA/m (d)
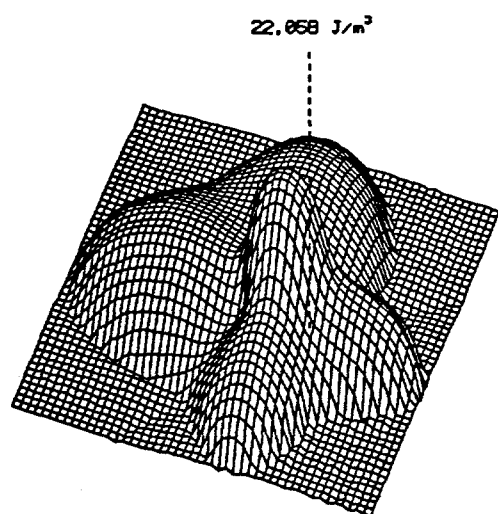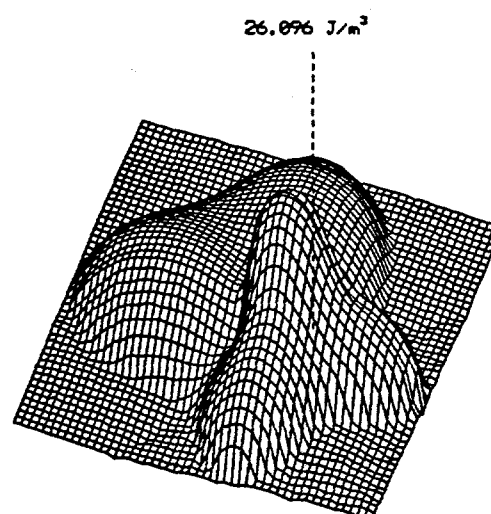
Figure 22. Three-dimensional energy plots with 24 kA/m and 3.5 MPa (a), 7 MPa (b), 10.5 MPa (c), and 14 MPa (d) applied stress

in the plots, as the stress increases the energy along the [$\bar{1}\bar{1}$1] direction, 90° from the [112] direction tends to decrease while the energy along the [112] direction tend to increase for a constant value of the applied field. As the stress increases, the energy surface at angles greater than 90° to the [112] directions flattens in the direction towards the [$\bar{1}$1$\bar{1}$] axis. The cubic symmetry of the energy surface in the crystal is broken upon the application of a magnetic field along the [112] direction.

The changes in the energy surface when applied field and stress are varied simultaneously are shown in Figures 19, 21(d), and 22(d). In Figure 19, no field or stress is applied. In Figure 21(d), a 12 kA/m field and 7 MPa of stress is applied, and in Figure 22(d), a 24 kA/m field and 14 MPa stress is applied. The energy shown along the [112] direction in the plots increases slowly as the magnitude of the applied field and stress increases. Increasing the stress applied along the [112] direction decreases the energy in the plane perpendicular to the applied stress while increasing the energy along the [112] direction, whereas increasing the applied field decreases the energy in the [112] direction.

Iteration   The magnetocrystalline anisotropy of Terfenol affects the initial magnetic state of the material and dictates preferred orientation directions for the magnetic moments in the crystal. Not considering any externally applied forces such as stress or magnetic field, it is energetically favorable for a magnetic moment to orient along one of the <111> easy axes. As the magnetic field or pressure is increased, the new orientation of the magnetization vector is located where the lowest possible local energy is found.

A modified Newton-Raphson iteration method in three dimensions is used to find the energy minimum. The position of the magnetization in one direction is held constant

while its position in the other two directions is varied until a minimum is found, then its position in another direction is held constant while its position in the two remaining directions is varied.

It is important to understand the symmetry between the [112] axis, along which the magnetic field and stress are applied, and the eight <111> easy axes in Terfenol along which the magnetization vectors are initially oriented. Table 4 lists the angles between each of the <111> axes and the [112] direction in degrees. It can be seen that the [111] direction lies closest to the [112] field direction, separated by only 19.5°. The angle between the [$\bar{1}$11] and [1$\bar{1}$1] directions and the [112] direction is 61.9°, and the [11$\bar{1}$] and [$\bar{1}$$\bar{1}$1] directions are separated by the [112] direction by 90°, while the [$\bar{1}$1$\bar{1}$] and [1$\bar{1}$$\bar{1}$] directions are separated by the [112] direction by 118°.

It can also been seen in Table 4 that the symmetry between the <111> axes and the [111] direction and [112] direction to be different. For example, with the field applied along the [111] direction, there are three directions ([$\bar{1}$11], [1$\bar{1}$1], and [11$\bar{1}$]) which are 70.5° from the [111] direction, and another three directions ([$\bar{1}$$\bar{1}$1], [1$\bar{1}$$\bar{1}$], and [$\bar{1}1\bar{1}$])

Table 4. Angles in degrees between the <111> directions and the [112] and [111] direction

[ ]	111	$\bar{1}$11	1$\bar{1}$1	11$\bar{1}$	$\bar{1}$$\bar{1}$1	$\bar{1}$1$\bar{1}$	1$\bar{1}$$\bar{1}$	$\bar{1}$$\bar{1}$$\bar{1}$
112	19.5	61.9	61.9	90	90	118	118	160.5
111	0	70.5	70.5	70.5	109.5	109.5	109.5	180

which are 109.5° away from the [111] direction. With the field applied along the [112]

direction, there are two directions ([$\bar{1}$11] and [1$\bar{1}$1]) which are 61.9° away from the [112]

direction, two more directions ([11$\bar{1}$] and [$\bar{1}\bar{1}$1]) which are 90° away from the [112] direction,

and another two directions ([$\bar{1}$1$\bar{1}$] and [1$\bar{1}\bar{1}$]) which are 118° away from the [112] direction.

In particular, the [11$\bar{1}$] and [$\bar{1}\bar{1}$1] directions are not symmetric with respect to the [111]

direction as they are with respect to the [112] direction.

Change in magnetization   The magnetization curve is calculated by following the

movement of the magnetization vector as the magnetic field is increased from zero. The

change in the component of the magnetization vector along the measurement direction ΔM is

plotted as a function of the magnetic field.

$$\Delta M = M_s(\cos\Omega_f - \cos\Omega_i) \tag{24}$$

where M_s is the saturation magnetization of Terfenol, and Ω_f and Ω_i the final and initial

orientations of the magnetization vector with respect to the measurement direction. The

saturation value of the magnetization for Terfenol is $M_s = 0.79$ MA/m, corresponding to $B_s =$

1.2 T at 165 kA/m.[8]

Change in magnetostriction   Using the anisotropic magnetostriction equation

presented in chapter one, the change in magnetostriction derived by the rotation of a

magnetization vector from an initial to a final orientation is given by

$$\Delta\lambda = \frac{3}{2}\lambda_{100}\sum_{j=1}^{3} (\alpha_{fj}^2 - \alpha_{ij}^2)\gamma_j^2$$

$$+ 3\lambda_{111}\sum_{j=1}^{3} (\alpha_{fj}\alpha_{fj+1} - \alpha_{ij}\alpha_{ij+1})\gamma_j\gamma_{j+1}$$

(25)

where the i,f subscripts denote the initial and final orientations, and the j subscript denotes each of the three crystallographic axes. The magnetostriction constants λ_{111} and λ_{100} for Terfenol are 1640 x 10^{-6} and 10-100 x 10^{-6}, respectively.[4] In the following calculations, the value $\lambda_{100} = 50$ x 10^{-6} has been used.

Hysteresis   Hysteresis is inherent in the three-dimensional anisotropic model. The magnetization vector follows the path of least energy through both reversible and irreversible rotational processes. In this model, hysteresis arises as a result of irreversible rotational processes, which depend on overcoming energy barriers caused by the magnetic anisotropy in the material. If the magnetic field is reversed from saturation to zero, the magnetization vectors in the three-dimensional anisotropic model will stay aligned along the [111] direction, because this is the position of the local energy minimum for the energy surface.

The effect of varying the first order anisotropy constant K_1 on the hysteresis of the magnetization curve is shown in Figure 23. For $K_1 = -15$ kJ/m^3, the hysteresis is significantly less than with K_1 - -60 kJ/m^3. The anisotropy constant K_1 affects the critical field values obtained using the three-dimensional rotation model. Measured values of K_1 range from -40 kJ/m^3 to -60 kJ/m^3.[41] For the following calculations, $K_1 = -40$ kJ/m^3 was used.

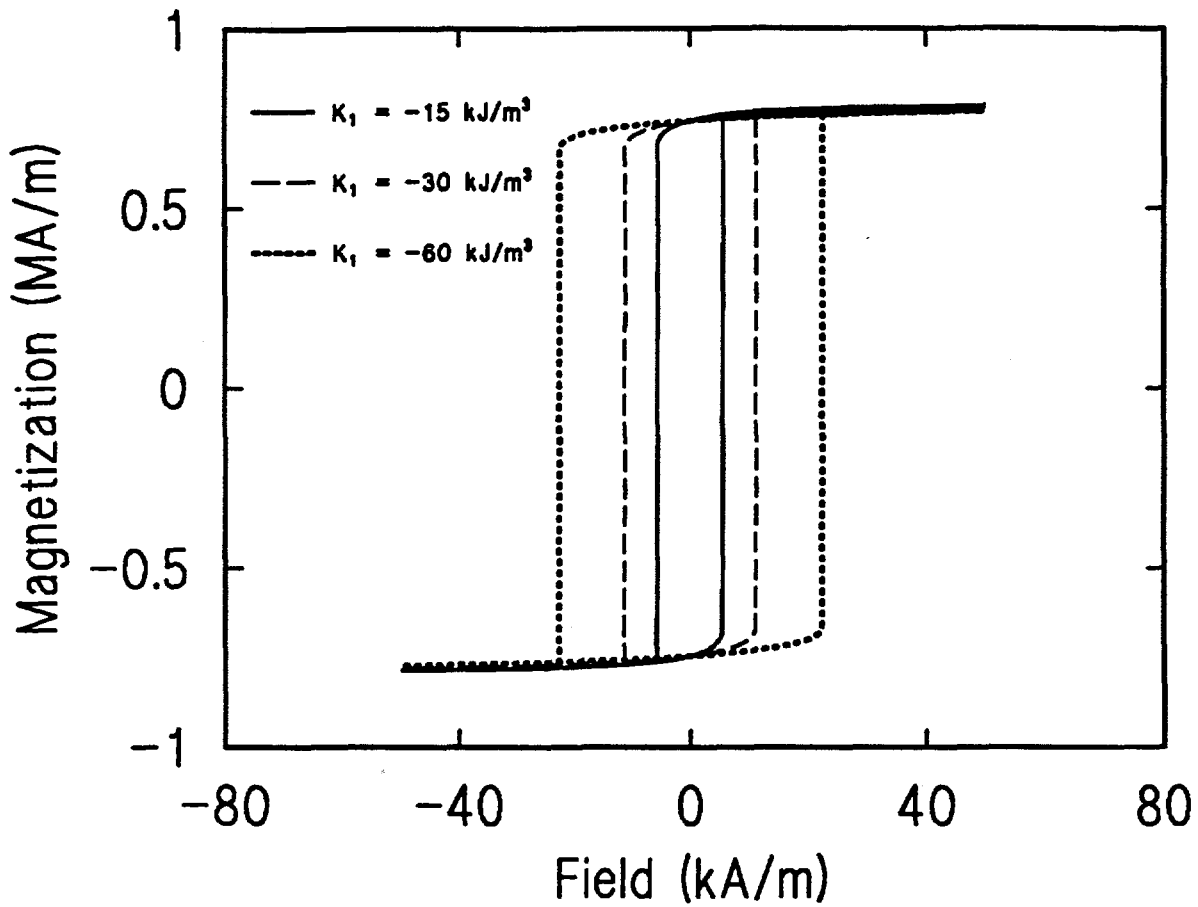Only initial magnetization and magnetostriction curves will be presented. The

Figure 23. Theoretical magnetization curves with different values for K_1

hysteresis effects observed in Figure 23 for non-interacting particles are not realistic for

Terfenol where interactions such as those between domains play an important role in the

observed magnetic and magnetostrictive properties.

Results and Discussion

Field applied along [112] direction   Figure 24 shows the magnetization and

magnetostriction curves calculated using equation 21 for no prestress with the moments

aligned initially along each of the eight <111> easy axes in Terfenol for K_1 = -40 kJ/m^3.

There are four main points of interest in each set of curves:

1) the initial values of the magnetization or magnetostriction
2) the large change in magnetization or magnetostriction occurring at a critical value of the magnetic field
3) the maximum change in magnetostriction or magnetization achieved by each initial orientation
4) the initial directions that result in a negative strain at low fields

The magnetostriction in all cases is initially zero by definition, whereas the

magnetization has either positive or negative initial values depending on whether the

component of magnetization along the field direction either lies initially parallel or

antiparallel to the field. The critical value of the magnetic field depends on the initial

orientation of the magnetization vector and the first anisotropy constant of the material.

The effect of a compressive stress on the magnetization and magnetostriction curves is

shown in the remaining figures. The magnetization and magnetostriction curves for a

compressive stress of 3.5 MPa are shown in Figure 25. It is noticeable that in some curves

there are two critical fields where a large change in magnetization or strain occurs.

The magnetization and magnetostriction curves for a compressive stress of 7 MPa are

shown in Figure 26. Similarly, for compressive prestresses of 10.5 MPa and 14 MPa, the

magnetization and magnetostriction curves are shown in Figures 27 and 28, respectively.

As the stress increases, the critical fields become larger and occur more than once in

Figure 24. Magnetostriction (top) and magnetization (bottom) curves at 0 MPa
prestress with the field and pressure applied along the [112] direction

Figure 25. Magnetostriction (top) and Magnetization (bottom) curves at 3.5 MPa prestress with the field and pressure applied along the [112] direction

Figure 26. Magnetostriction (top) and Magnetization (bottom) curves at 7 MPa
prestress with the field and pressure applied along the [112] direction
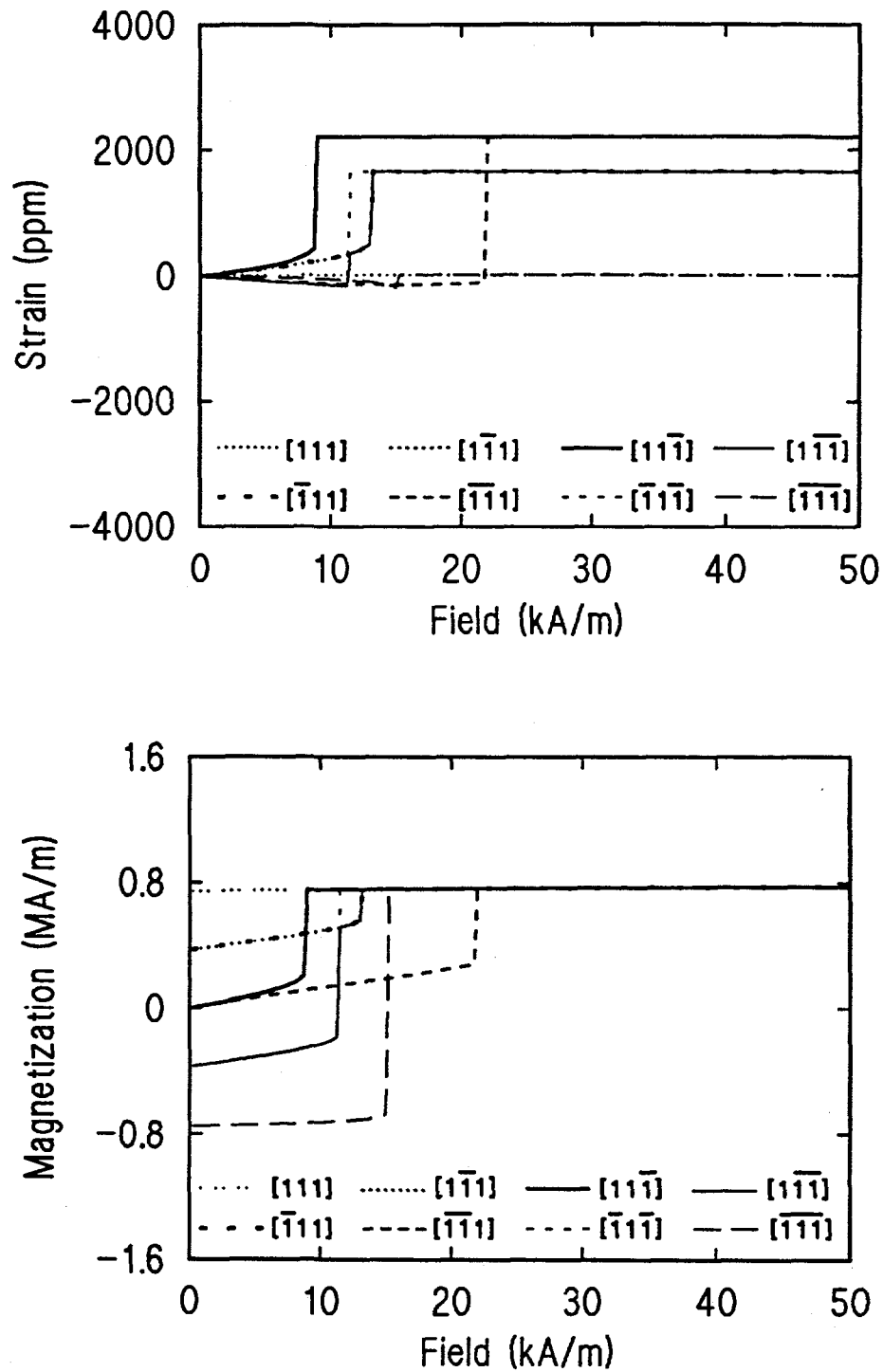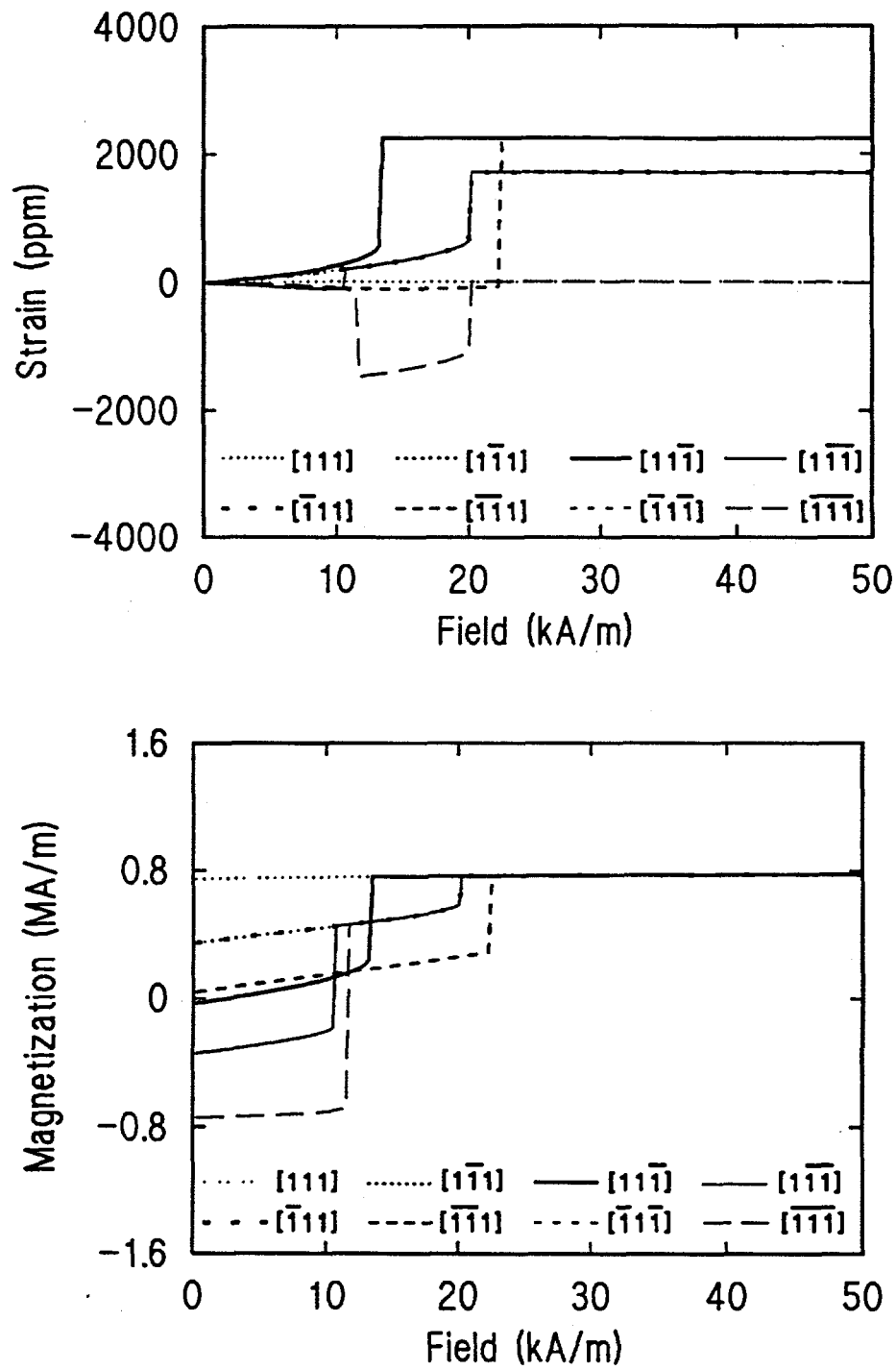
Figure 27. Magnetostriction (top) and Magnetization (bottom) curves at 10.5 MPa prestress with the field and pressure applied along the [112] direction
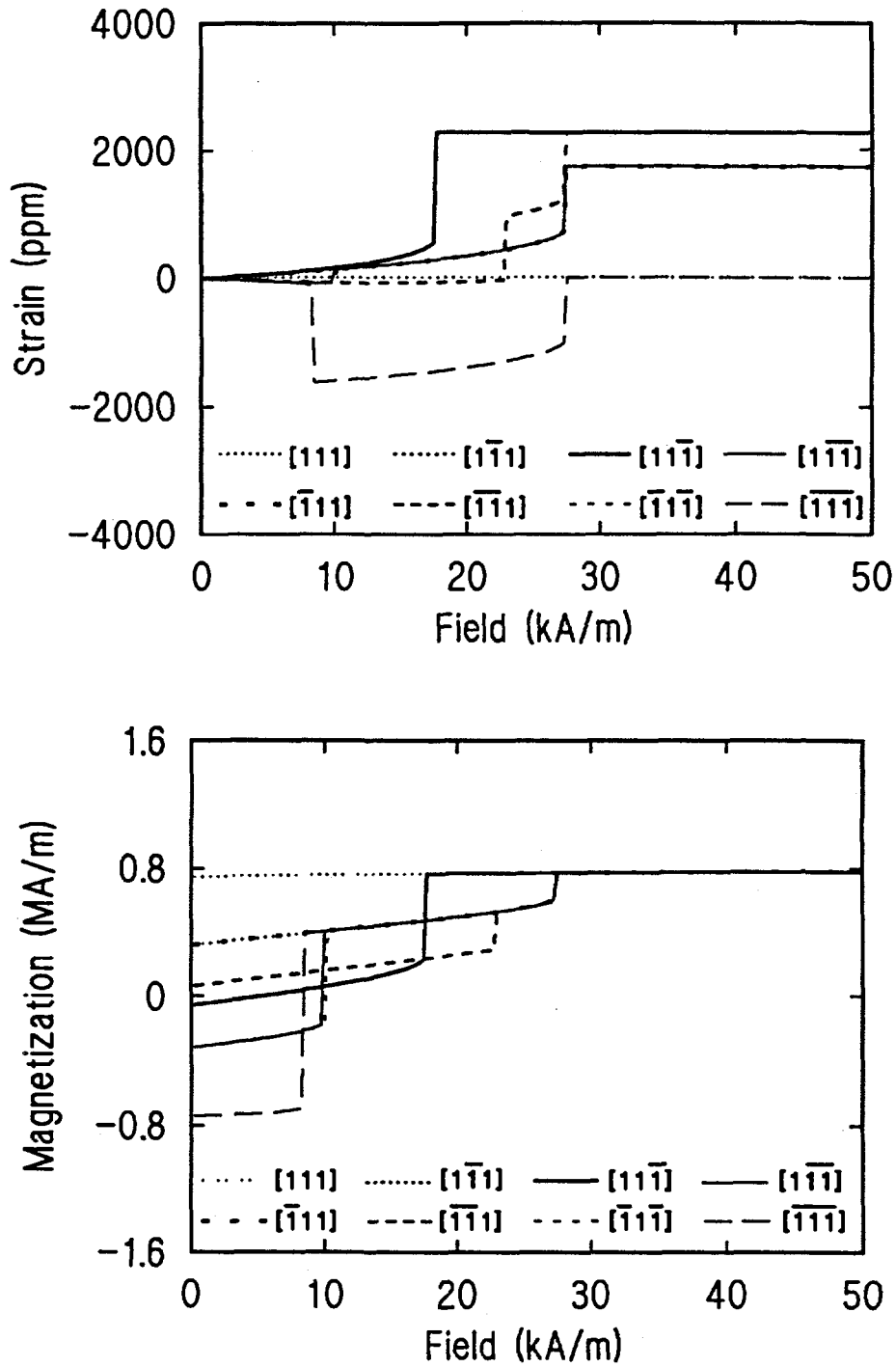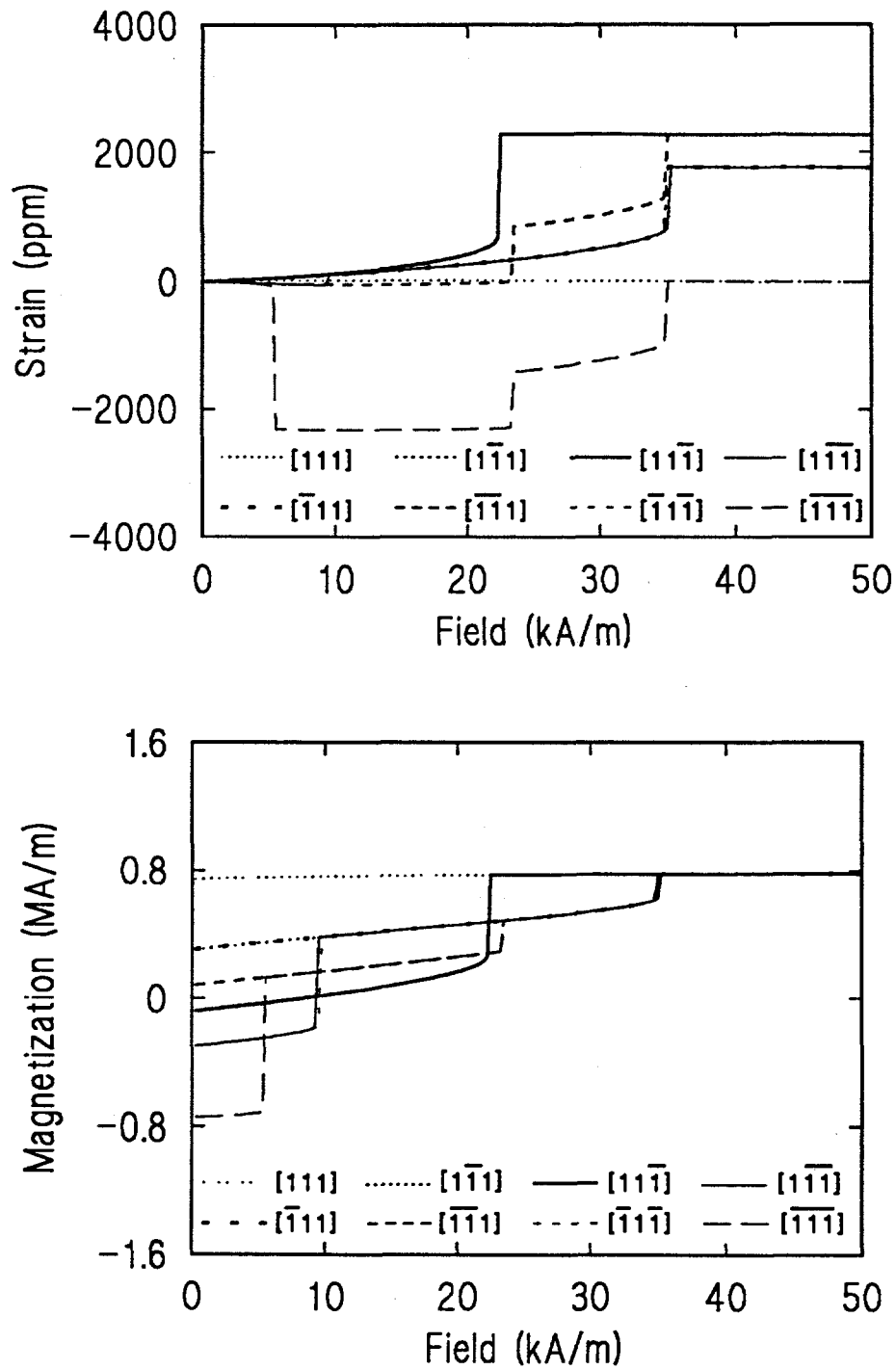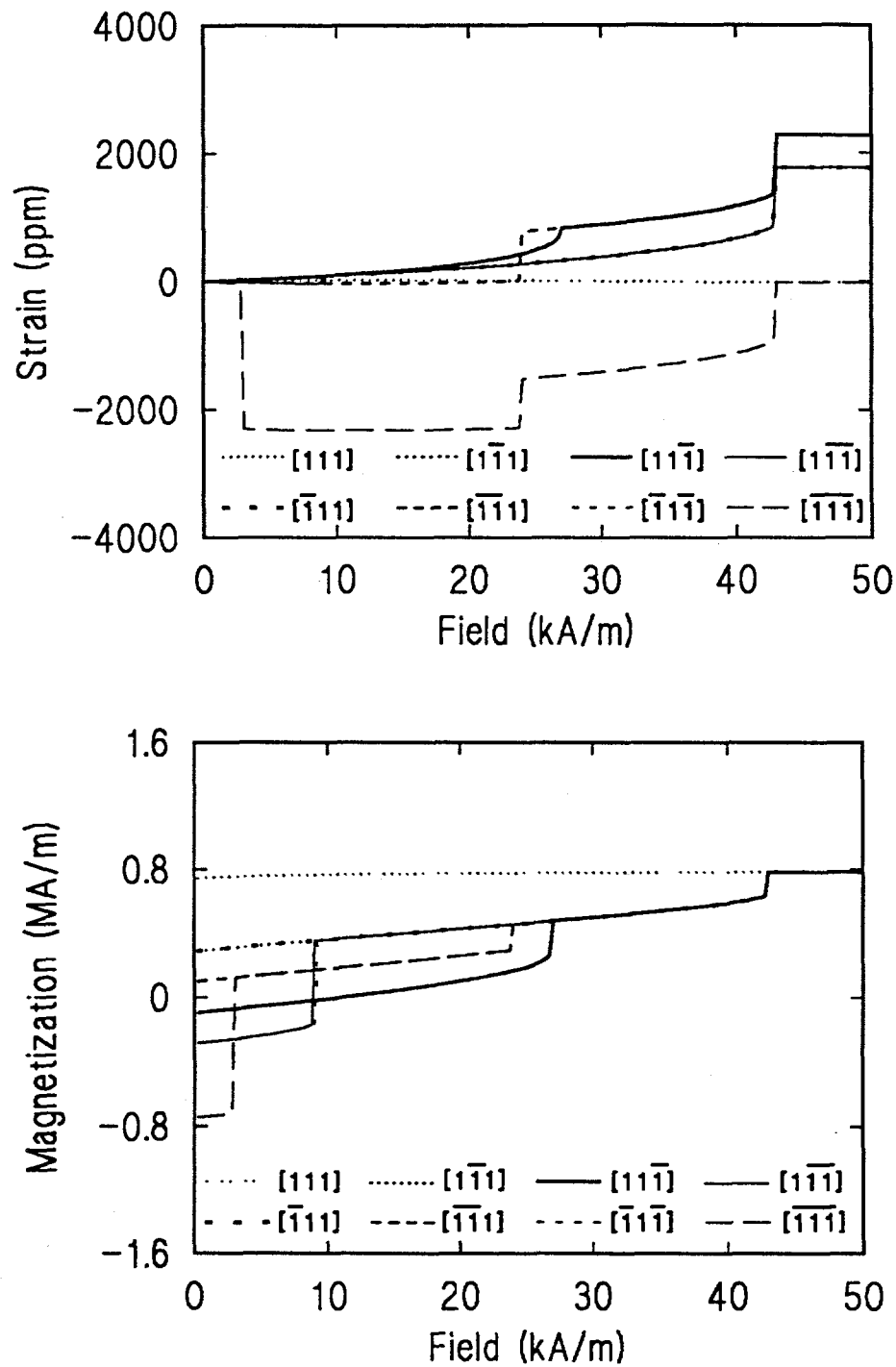
Figure 28. Magnetostriction (top) and Magnetization (bottom) curves at 14 MPa
prestress with the field and pressure applied along the [112] direction

many of the curves as a result of the magnetization rotating from one <111> direction into

another <111> direction closer to the direction of applied field and stress. The change in

strain depends only on the initial and final orientation of the magnetization vector. The only

effect of stress will be to change these orientations.

The critical field values H_{cr} in Table 5 represent the magnetic field at which the

magnetization vector rotates from its initial orientation into the [$\bar{1}$11] or [1$\bar{1}$1] direction closer

to the [111] direction and hence the direction of applied field. Only the initial orientations at

angles 90° or greater, from the direction of applied field and stress, jump into an intermediate

<111> direction before rotating into the [111] direction which is closest to the direction of

applied field and stress. Table 6 shows the magnetic field at which the magnetization vector

rotates into the [111] direction.

As shown in the magnetization curves, the critical fields vary between 9-22 kA/m for

Table 5. H_{cr} in A/m when the magnetization vector rotates from its initial <111> direction into the [$\bar{1}$11] or [1$\bar{1}$1] direction with the magnetic field applied along the [112] direction

	0 MPa	3.5 MPa	7 MPa	10.5 MPa	14 MPa
[$\bar{1}$11]	---	---	23,000	23,500	24,000
[11$\bar{1}$]	---	---	---	---	27,000
[$\bar{1}$1$\bar{1}$]	---	10,750	10,250	9,750	9,250
[1$\bar{1}$$\bar{1}$]	11,500	10,750	10,000	9,500	9,000
[$\bar{1}$$\bar{1}$$\bar{1}$]	---	11,750	8,500	23,500	24,000

Table 6. H_{cr} in A/m when the magnetization vector rotates into the [111] direction
with the magnetic field applied along the [112] direction

	0 MPa	3.5 MPa	7 MPa	10.5 MPa	14 MPa
[111]	---	---	---	---	---
[Ī11]	13,250	20,250	27,500	35,000	43,000
[1Ī1]	13,250	20,250	27,500	35,250	43,000
[ĪĪ1]	22,000	22,500	27,500	35,000	43,000
[11Ī]	9,000	13,500	17,750	22,500	43,000
[Ī1Ī]	11,500	20,250	27,500	35,000	43,000
[1ĪĪ]	13,250	20,250	27,500	35,250	43,000
[ĪĪĪ]	15,250	20,250	27,500	35,000	43,000

no prestress, and between 9-43 kA/m for 14 MPa compressive prestress. At low levels of
prestress (less than 14 MPa), a majority of <111> directions rotate into the [111] direction
near the same critical field value. At higher compressive prestress, more intermediate
irreversible rotational processes occur. Moments rotate from one <111> direction to another
<111> direction closer to the direction of the applied field. At 14 MPa, the magnetization
vectors simultaneously rotate into the [111] direction at 43 kA/m due to the large anisotropy
created by the applied stress.

Field applied along [111] direction To gain a higher bulk magnetostriction, the
magnetic field must be applied along one of the <111> directions which are the magnetic
easy axes since the magnetostriction coefficient is highest along this direction. Experiments
on Terfenol with the magnetic field applied along the [111] direction are not very common

because Terfenol is usually grown with a [11$\bar{2}$] orientation as a result of practical problems associated with the growth of large specimens of <111> oriented Terfenol. Theoretical curves were generated with the magnetic field and stress applied along the [111] direction and the magnetization vectors initially oriented along the [111] direction.

The magnetization and magnetostriction curves for no prestress are shown in Figure 29. Both the [111] and [$\bar{1}\bar{1}\bar{1}$] directions show no change in strain as expected because they involve either no rotation or 180° rotation of magnetization. The [$\bar{1}\bar{1}\bar{1}$] direction also shows no change in magnetization up to 50 kA/m, due to its orientation directly opposing the applied magnetic field, in which mathematically $dE/d\theta = 0$, so that no rotation occurs.

Again the different <111> orientations rotate into the [111] direction at different values of critical field strength. The magnetic and magnetostrictive behavior of three initial orientations are similar, and all six initial orientations achieve the same maximum strain of 2187 x 10^{-6}. The three initial directions, [$\bar{1}\bar{1}$1], [$\bar{1}$1$\bar{1}$], and [1$\bar{1}\bar{1}$], also achieve a maximum negative strain of 273 x 10^{-6} due to the strict dependence of the magnetostriction on the initial and final orientations of the magnetization vector.

With 3.5 MPa prestress applied, the magnetic and magnetostrictive behavior changes slightly as shown in Figure 30. The [$\bar{1}\bar{1}\bar{1}$] direction flips directly into the [111] direction at 35,750 A/m due to the change in the energy surface as a result of the applied stress. The three directions initially 109° from the direction of applied field and stress follow the same behavior as the [$\bar{1}$11], [1$\bar{1}$1], and [11$\bar{1}$] directions above 18,750 A/m. The slight differences in magnetostrictive behavior below 18,750 A/m are caused by the magnetization vectors not quite lying along the <111> directions after the stress is applied. The maximum achievable

Figure 29. Magnetostriction (top) and Magnetization (bottom) curves at 0MPa
prestress with the field and pressure applied along the [111] direction

Figure 30. Magnetostriction (top) and Magnetization (bottom) curves at 3.5 MPa prestress with the field and pressure applied along the [111] direction

Figure 31. Magnetostriction (top) and Magnetization (bottom) curves at 7 MPa prestress with the field and pressure applied along the [111] direction
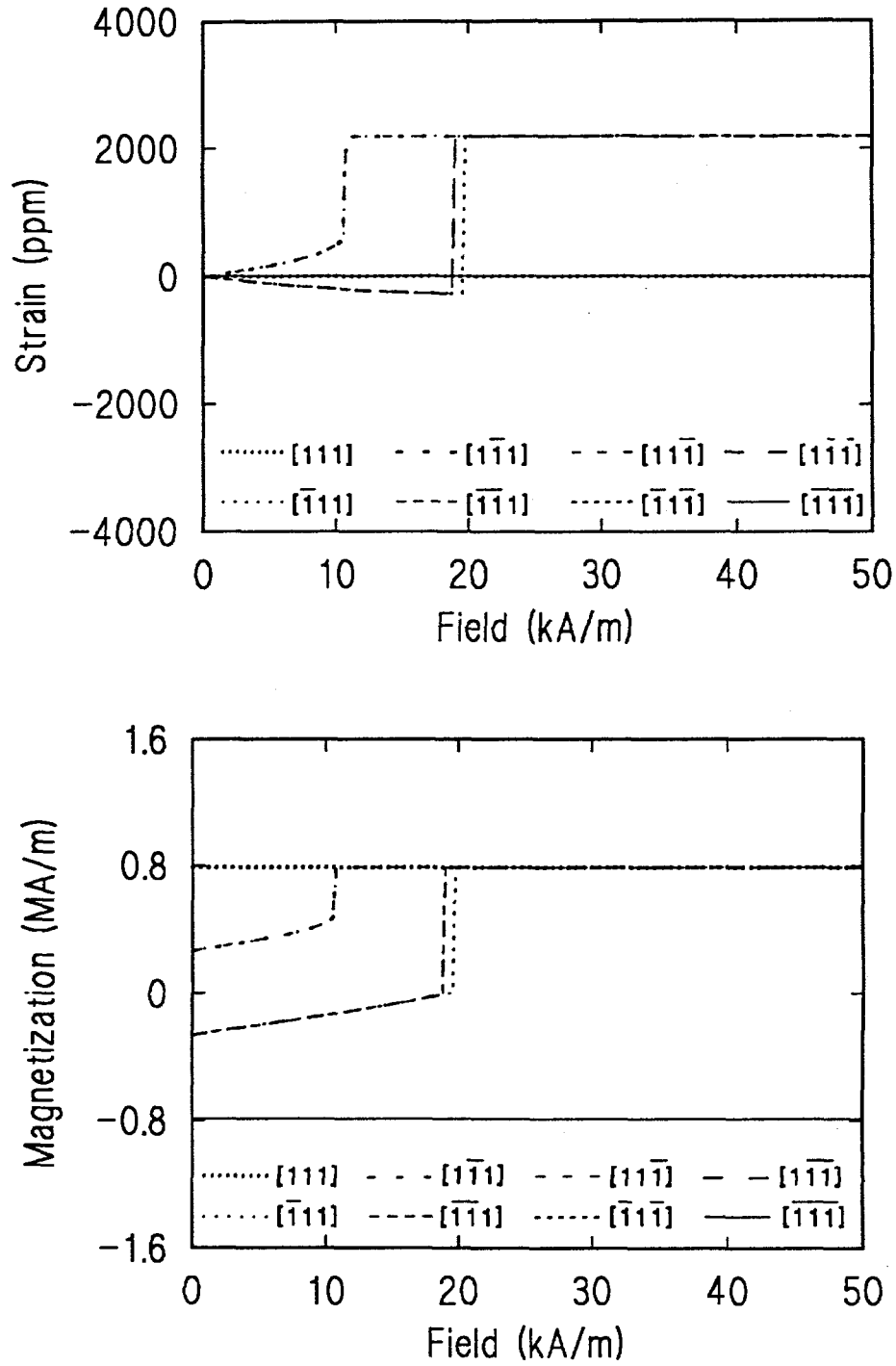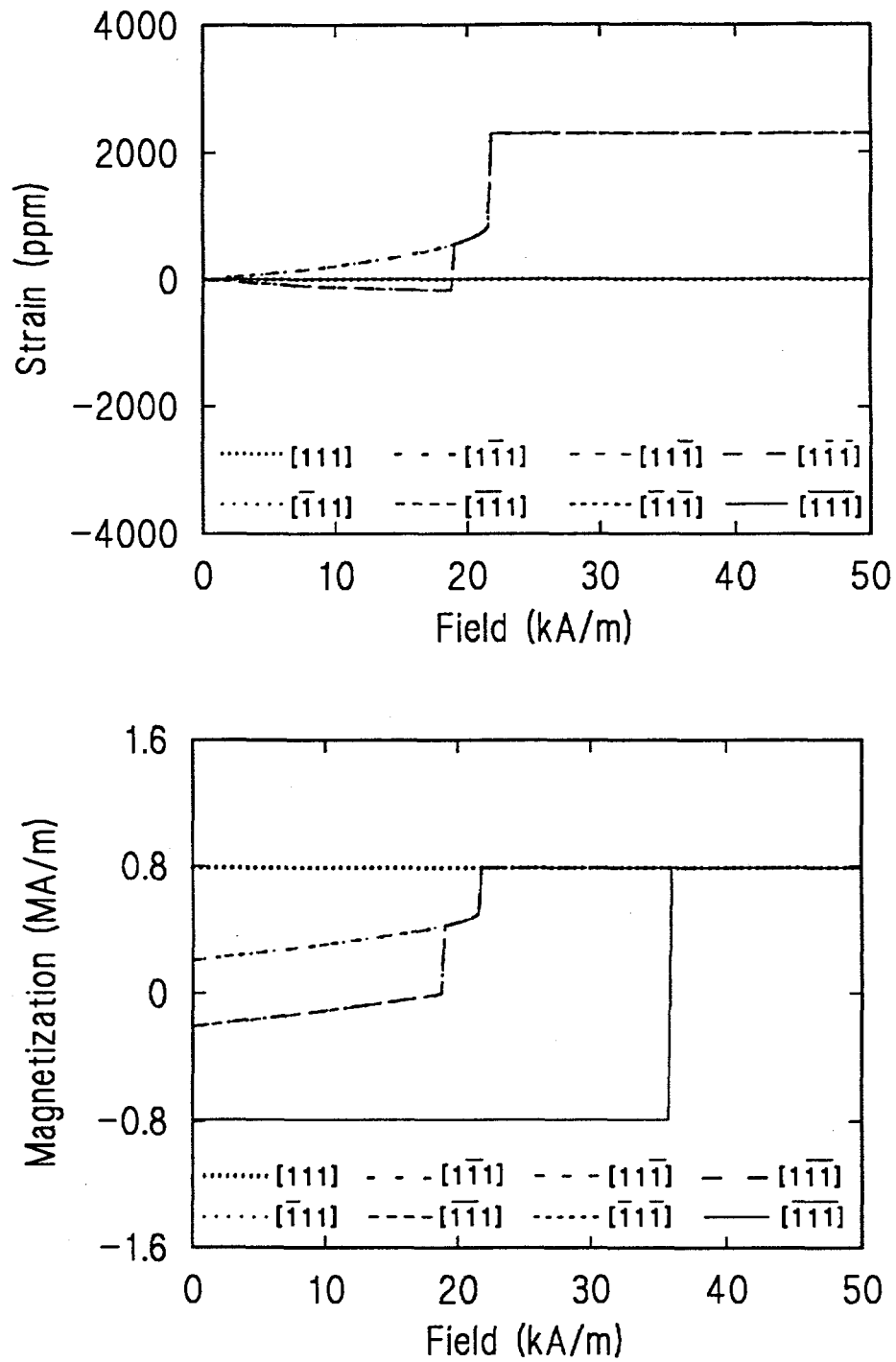
Figure 32. Magnetostriction (top) and Magnetization (bottom) curves at 10.5 MPa
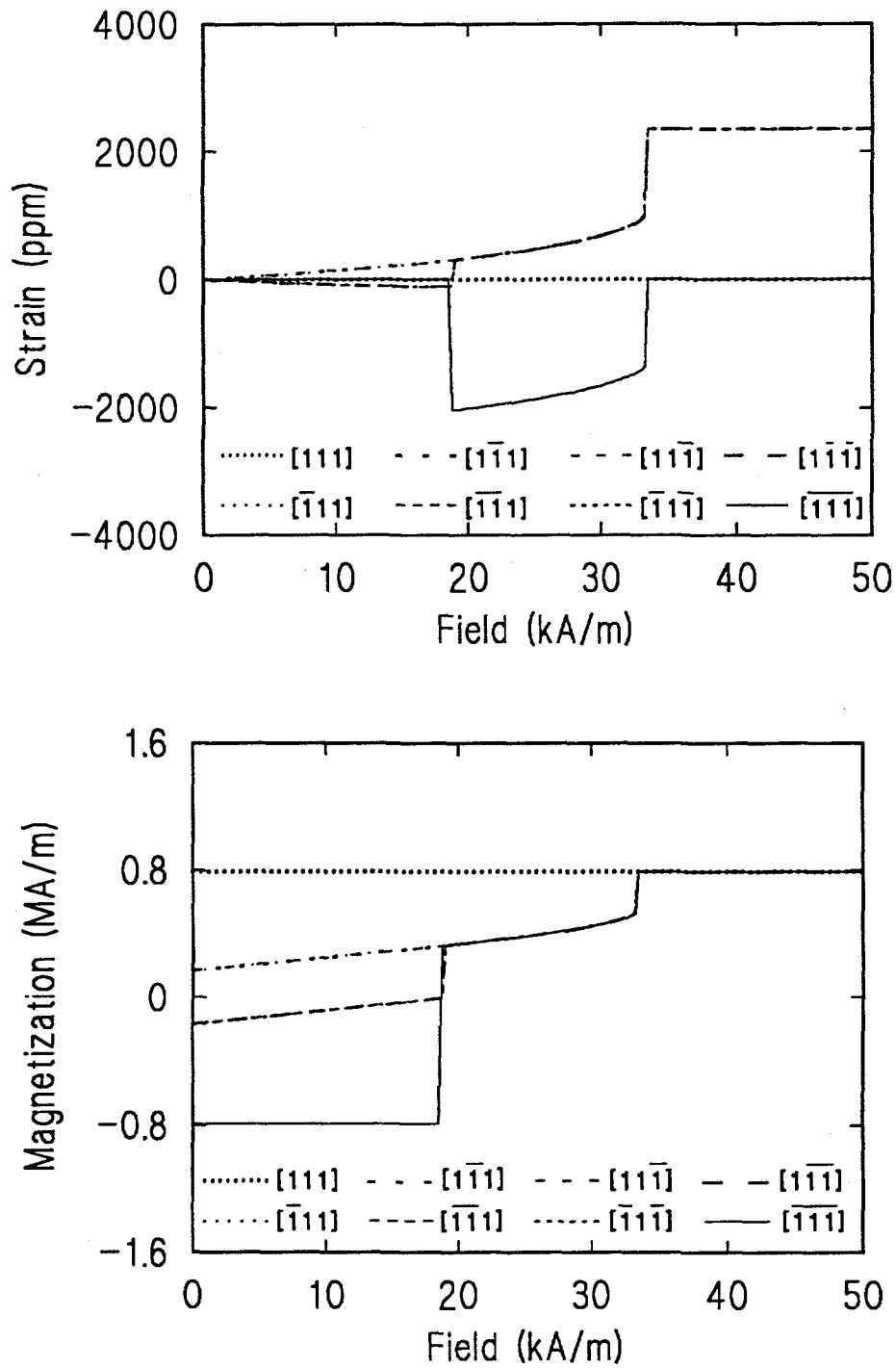prestress with the field and pressure applied along the [111] direction

Figure 33. Magnetostriction (top) and Magnetization (bottom) curves at 14 MPa prestress with the field and pressure applied along the [111] direction

strain from these six directions increases slightly while the negative strain produced by the [1$\bar{1}\bar{1}$], [$\bar{1}$1$\bar{1}$], and [1$\bar{1}\bar{1}$] directions has decreased slightly.

The magnetization and magnetostriction curves for 7 MPa and 10.5 MPa prestress are shown in Figures 31 and 32, respectively. As the prestress is increased, the [$\bar{1}\bar{1}$1] direction flips at lower field strengths into <111> directions closer to the direction of applied field and stress. Tables 7 and 8 summarize the values of the critical field for various levels of prestress and different initial orientations. The overall change in magnetostriction is still zero for the [$\bar{1}\bar{1}\bar{1}$] direction, but large negative strains are observed at some field strengths due to the magnetization vector flipping indirectly into the [111] direction through other <111> directions. At higher prestress, the moments flip into the [111] direction at higher critical fields, 33,250 A/m at 7 MPa and 45,250 A/m at 10.5 MPa. In addition, the maximum strain increases slightly, not due to any changes in λ_{100} or λ_{111}, but instead due to slight changes in the initial orientations of the magnetization vectors.

Table 7. H_{cr} in A/m when the magnetization vector rotates into a <111> direction 71° from the [111] direction which the magnetic field and stress are applied

	0 MPa	3.5 MPa	7 MPa	10.5 MPa	14 MPa
[$\bar{1}$1]	---	18,750	18,750	18,750	19,000
[$\bar{1}$1$\bar{1}$]	---	18,750	18,750	20,250	18,500
[1$\bar{1}\bar{1}$]	---	18,750	18,750	18,750	19,000
[$\bar{1}\bar{1}\bar{1}$]	---	---	---	1,000	---
	---	---	18,500	18,250	18,500

Table 8. H_{cr} in A/m when the magnetization vector rotates into the [111] direction with the magnetic field and stress applied along the [111] direction

	0 MPa	3.5 MPa	7 MPa	10.5 MPa	14 MPa
[111]	---	---	---	---	---
[$\bar{1}$11]	10,500	21,500	33,250	45,250	---
[1$\bar{1}$1]	10,500	21,500	33,250	45,250	---
[11$\bar{1}$]	10,500	21,500	33,250	45,250	---
[$\bar{1}\bar{1}$1]	18,750	21,500	33,250	45,250	---
[$\bar{1}$1$\bar{1}$]	19,500	21,500	33,250	45,250	---
[1$\bar{1}\bar{1}$]	18,750	21,500	33,250	45,250	---
[$\bar{1}\bar{1}\bar{1}$]	---	35,750	33,250	45,250	---

The magnetization and magnetostriction at 14 MPa prestress are shown in Figure 33. All the moments are initially oriented either approximately 71° or 109° from the [111] direction. The magnetization rotates gradually toward the [111] direction but does not reach saturation at 50 kA/m. As a result, the maximum strain is less than 1000 x 10^{-6} at 50 kA/m. In addition, the negative strain has almost disappeared.

The three-dimensional anisotropic rotation model consists of non-interacting single domain particles. Each particle generates its own magnetization curve independent of the other particles. In experimental situations, bulk values of the magnetic properties are measured.

In the demagnetized state, the bulk magnetization is assumed to be zero. In order to simulate this situation in our model, it is assumed that there is equal occupancy of each initial

direction of the magnetization making the initial bulk magnetization zero. The resulting

curves are shown in Figure 34 with the magnetic field applied along the [112] direction and

no prestress.

At field strengths of H = 9 kA/m and above the magnetostriction reaches 1385×10^{-6}

and the magnetization reaches 0.79 MA/m which is known to be the saturation magnetization

M_s. This applies to the equal distribution of moments among each of the easy <111>

directions. If the distributions were different in the initial state, but still lead to an initially

Figure 34. Theoretical bulk magnetization and magnetostriction curve with each initial
orientation equally probable

demagnetized state then the magnetization would still reach 0.79 MA/m at high fields but the magnetostriction amplitude would change. Magnetostriction amplitude would be a maximum if initially all moments were oriented 90° to the field. If interactions between particles are considered, the bulk magnetization and strain curves would be much smoother.

EXPERIMENTAL MAGNETIZATION CURVES ALONG DIFFERENT CRYSTALLOGRAPHIC DIRECTIONS IN SMALL [111] ORIENTED TERFENOL SAMPLES

Introduction

The highly magnetostrictive material Terfenol-D can be grown with <112> orientation, but so far it has proved impossible to grow large specimens with <111> orientation because of the large growth speed of the [11$\bar{2}$] direction.[42] This is unfortunate because the magnetostriction coefficient is largest along the <111> direction, λ_{111} = 1640 x 10^{-6}, and therefore the largest bulk magnetostrictions could be achieved with a <111> oriented single crystal specimen. As a result of the difficulty in producing <111> oriented specimens, most of the data reported in the literature[43] has been taken on <112> oriented material, although some results on <111> oriented material have been reported.[44]

In this chapter, the magnetic properties of <111> oriented specimens are investigated. Magnetic measurements carried out along the <111> axes are difficult to perform given the limitations on sample size and preparation, but the results of such measurements are unique and should give insight into the properties of [111] grown samples.

The magnetic moment of small samples can be measured directly using a vibrating sample magnetometer (VSM). The vibrating sample magnetometer[45], shown in Figure 35, provides a very simple way of determining the magnetic moment of a sample in applied fields of up to 0.5 T. Measurements directly give the magnetization of the sample being studied. The sample is vibrated using a transducer between a pair of Helmholtz coils and

Transducer

Matched pair
of coils

Electromagnet

Waveform
generator

Reference sample (Nickel)

Signal
converter
unit

IBM PC

Bi-polar DC
power supply

Test specimen

Figure 3.1 Experimental set-up with Vibrating Sample Magnetometer

the difference between the magnetic induction with and without the specimen is recorded.

With this information the magnetization of the sample can be calculated. The drawback

of using this method is that the samples must be very small which means that the

demagnetizing effects will be very large. Therefore the technique is not ideal for

determining technical magnetization curves. However, it is well-suited to determine the

saturation value of the magnetization.

Materials and Methods

<u>Sample</u> <u>preparation</u>

Magnetization curves were measured for various different crystallographic directions. These directions were determined by placing the sample in a magnetic field measuring its magnetic moment at different angles. From the magnetic moment measurements along different direction it was possible to determine each of the different

Top View   Side View

Figure 36. Crystallographic axes in disk-shaped samples

crystallographic orientations present in the samples (see Figure 36). Samples were

produced by cutting a specimen from a <112> oriented rod at the appropriate angle after

identifying the location of the <111> axis by x-ray diffraction.

A small [111] oriented Terfenol sample to be used in the VSM was cut from a

[11$\bar{2}$] oriented sample. First, a laser beam was used to align the face of the [11$\bar{2}$] sample

Figure 37. Set-up for cutting a [111] oriented sample

perpendicular to a certain reference direction, in this case an optical bench. The sample was then mounted into an x-ray diffraction unit with the plane face perpendicular to the x-ray beam. An x-ray diffraction pattern was then made, and the $[11\bar{2}]$ direction was confirmed. The sample was then rotated until the [111] and $[\bar{1}\bar{1}\bar{1}]$ directions perpendicular to the $[11\bar{2}]$ direction were at the top of the sample, 90° from the plane of the x-ray beam. This orientation was fixed and

then small [111] samples were cut using an electrical discharge cutting machine (see Figure 37). Since the sample was grain oriented, the placement of the cutting electrode along the top of the sample does not affect the orientation of the cut sample.

The error in determining the <111> axes is derived from how accurately the $[11\bar{2}]$ direction is known and the positioning of the $[11\bar{2}]$ plane parallel to the cutting plane of the electrode. The error was estimated to be less than ±5°. The three small cylindrical samples were then machined down and electropolished.

Experimental procedure

A commercial VSM was used to perform the measurements presented in this chapter. The system performs room temperature measurements and is capable of being fully controlled by a computer through a GPIB interface. The current output of two bipolar power supplies connected in series to the electromagnet was controlled by the VSM and run by a personal computer while the field was monitored by a built-in Hall effect gaussmeter probe. The VSM was capable of measuring a maximum range of 5 x 10^{-8} A•m² to 10 A•m² with an error of less than 2%.

The material was placed in the sample holder centered between the pole pieces of an electromagnet. The sample holder was directly connected to the AC transducer assembly located above the magnet. The transducer converts a constant sinusoidal ac drive signal provided by an electronic circuit located in the console into a sinusoidal vertical vibration of the sample piece. Two stationary pairs of Helmholtz coils mounted on the pole pieces of the magnet picked up the electrical signal (emf) induced as the sample was vibrated. This ac signal was proportional to the vibration frequency and magnetic moment, and dependent on the vibration amplitude. An output signal better than ±0.05% of full scale for a fixed set-up of the coil geometry was achieved using this set-up.

The VSM was supplied with a nickel sample for the purpose of calibration. Nickel has a saturation magnetic moment of 4.95×10^{-3} A•m^2 measured at the saddle point of its saturation magnetization in the VSM.

The VSM output the magnetic moment of the sample and the magnetization was then calculated. The following formula was used in determining the magnetization of the material.

$$M = \frac{\mu \cdot \rho}{m} \tag{26}$$

where M represents the magnetization in A/m, μ the measured magnetic moment in A•m^2, ρ the density of the sample in kg per cubic meter, and m the mass of the sample in kg.

The VSM control unit had internal memory, and the data were stored in the

internal memory of the VSM and then downloaded to files on disk.

Demagnetization factor

Once any magnetic sample is subject to a uniform magnetic field, demagnetizing

fields develop which depend on the shape of the sample. The magnitude of the

demagnetizing field alters the measured value of the magnetic field and must be corrected

for. The demagnetizing factor only depends on the shape (aspect ratio) of the sample[46,47]

The Terfenol samples used in these measurements were disk-shaped. The demagnetization

factor for this shape of sample is not well documented. The demagnetization factor was

instead found by considering the initial susceptibility of a cylindrical sample of known

demagnetization factor and the initial susceptibility of the same disk-shaped material.

$$H_{i,cyl} = H_i - N_d M_i \qquad (27)$$

where $H_{i,cyl}$ denotes the magnetic field of the cylindrically shaped sample, H_i the magnetic

field, N_d the demagnetization factor, and M_i the magnetization of the disk-shaped sample.

Dividing equation 27 by H_i,

$$\frac{H_{i,cyl}}{H_i} = 1 - N_d \chi_i \qquad (28)$$

where χ_i denotes the initial susceptibility of the disk-shaped sample given by

$$\chi_i = \frac{M_i}{H_i} \tag{29}$$

The initial susceptibility for the larger cylindrical sample after correcting for demagnetizing effects can be represented by

$$\chi_{i,cyl} = \frac{M_i}{H_{i,cyl}} \tag{30}$$

where $\chi_{i,cyl}$ denotes the initial susceptibility of the cylindrical sample and the magnetization of the cylindrical sample is assumed to be equal to the magnetization of the disk-shaped sample. Substituting equation 30 into equation 28 and rearranging terms results in an equation for the demagnetization factor which depends on the initial susceptibilities of both samples.

$$N_d = \frac{\chi_{i,cyl} - \chi_i}{\chi_{i,cyl}\chi_i} \tag{31}$$

After calibrating the VSM with the nickel sample supplied by the manufacturer, the crystallographic directions in a small disk-shaped sample were determined lying with its round face parallel to the field direction, Figure 36. The magnetic moment was measured at a field strength of about 240 kA/m for different angles of orientation in the applied field. This plot along with knowledge of the axes that had to be in the plane measured allowed the various crystallographic axes present to be determined. Two <110>

directions, along with the $[11\bar{2}]$ and $[\bar{1}\bar{1}2]$ directions were in the plane and the

magnetization curves with the field applied along each of these different directions was

measured. Also, the magnetization curves along both the [111] and $[\bar{1}\bar{1}\bar{1}]$ directions were

measured, which are perpendicular to the plane with the <110> directions.

Magnetization Curves

A summary of the experimental results are shown in Table 9. Magnetization

curves corrected for demagnetizing effects with $N_d = 0.22$ (disk-shaped samples of

diameter 3.1 mm and length 1.95 mm) representing one each of the <110>, <112> and

<111> directions is shown in Figure 38.

All directions, as expected exhibited similar coercivities. The curves for the <110>

directions were very similar showing the inherent symmetry in this particular set of axes.

Table 9. Experimental data

Orientation	M_{max} (A/m)	H_c (A/m)	M_{rem} (A/m)
$[1\bar{1}0]$	731000	1862 (-2205)	243000 (-206000)
$[\bar{1}10]$	730000	1862 (-2321)	221000 (-206000)
$[11\bar{2}]$	774000	1990 (-2255)	192000 (-177000)
$[\bar{1}\bar{1}2]$	773000	1862 (-1923)	164000 (-163000)
$[111]$	736000	1989 (-2285)	62300 (-49400)
$[\bar{1}\bar{1}\bar{1}]$	736000	1591 (-2387)	64400 (-49200)

Figure 38. Magnetization curves for different crystal orientations

The two curves in the <112> directions showed a larger magnetic moment at a given field strength compared with the <110> directions.

Conclusions

The coercivities are a reflection of the magneto-crystalline anisotropy and the defects in the material. The only variable is the orientation of the twinning plane with respect to the applied magnetic field. For the <110> directions, the twinning plane is parallel to the field direction, whereas for the two <112> and two <111> directions, the magnetic field is applied perpendicular to the twinning plane. The difference in maximum magnetization can be explained by the fact that the <112> directions lie closer than the <110> directions to the nearest <111> direction.

MAGNETIC EFFECTS OF A TIME VARYING MAGNETIC FIELD ON NICKEL

Loss Mechanisms

Under static conditions, a magnetic material usually exhibits a hysteresis loss as a result of impedances to changes in magnetostriction caused by the pinning sites and anisotropy when subject to a reversing quasi-dc magnetic field. The area of a static BH-loop is the energy loss. Under certain circumstances, such as the nonsaturated state with field values below the knee of the BH-curve (ie. minor loop region), the hysteresis loss can be expressed in terms of a phase lag between the magnetic induction and the applied magnetic field. If δ_h is the phase lag angle, the hysteresis loss under these conditions is given by $\tan \delta_h$. Introducing an a.c. magnetic field to the system creates further losses. An emf is generated in the plane at right angles to the direction in which the induction changes and the associated flow of currents in the material are referred to as eddy currents. There are two types of eddy current losses resulting in a reduction of the reversible permeability: macroscopic classical eddy current losses and micro eddy current losses.

The classical eddy current loss is expressed as $\tan \delta_e$, and is the result of a counteracting field generated by moving conduction electrons. The classical eddy current loss can be calculated for a sinusoidal magnetic field applied to a cylindrical conducting specimen as will be shown later. The classical eddy current losses depend on the conductivity and permeability of the material and become significant when subjected to

fields of high frequency.

Micro eddy current losses are due to eddy currents generated around domain walls and cause domain wall damping. This loss factor represented by tan δ_a depends on the pinning sites, the number, size, and shape of domain walls, and other hysteretic effects making it difficult to calculate. It is commonly referred to as an anomalous loss because in the past its origin was not well known.[48]

The frequency dependence of the classical eddy current loss is different from that of the micro eddy current loss. The energy loss due to classical eddy currents increases with frequency, whereas the loss due to micro eddy currents decreases as $1/f^2$ as the frequency increases.[49] The loss due to the generation of micro eddy currents decreases at high frequencies due to domain wall damping. Both eddy current losses also depend on the amplitude and variation of magnetic field.

Discontinuous changes in the magnetic field, such as a square or triangular variation in the magnetic field, produce additional time lag effects due to domain wall relaxation and diffusion relaxation. Disaccommodation, a change in permeability with time, is a relaxation effect which results from the mechanical, magnetic, or thermal disturbances of atoms due to a sharp discontinuity in the applied magnetic field and will be discussed in more detail later.[50]

The total loss is given by

$$\delta_{total} = \delta_h + \delta_e + \delta_a \tag{32}$$

Each loss is discussed here in more detail as it applies to continuous and discontinuous changes in the magnetic field.

Eddy current loss and the skin effect

Eddy currents   A changing magnetic field induces currents in a bulk conductor which are called eddy currents. The induced emf can be described by Faraday's law of induction given by

$$\varepsilon = -\frac{d\Phi}{dt} \tag{33}$$

for a circuit lying in a time varying magnetic flux, where ε represents the induced emf, t the time, and Φ the flux which is a product of the magnetic induction B and the area A which the induction flows through.[51] The induced currents tend to generate a magnetic field that counters the imposed change in flux, following Lenz's law, and the net effect is to prevent the applied field from penetrating to the interior of the material.

For an a.c. sinusoidal drive field (ie. a continuous change in magnetic field), the a.c. magnetic field is given by

$$H = |H|e^{j\omega t} \tag{34}$$

and the induction B is given by

$$B = |B|e^{j(\omega t - \delta_{total})} \qquad (35)$$

where the angle δ_{total} is the total loss angle or the phase angle between the induction and the magnetic field. The permeability then becomes complex.

$$\mu = \mu' + j\mu'' \qquad (36)$$

where μ denotes the permeability, μ' the real component, and μ'' the imaginary component of the permeability. The magnitude of the permeability is given by

$$|\mu| = \sqrt{\mu'^2 + \mu''^2} \qquad (37)$$

where the two components of the permeability are given by

$$\mu' = \mu\cos\delta_m \qquad (38)$$

$$\mu'' = \mu\sin\delta_m \qquad (39)$$

The real component, μ', corresponds to the magnetic flux which is in phase with the magnetic field. The imaginary part, μ'', results from the phase difference between the flux and applied field and represents the eddy current loss.[5] The difference between the classical eddy current loss and μ'' is an anomalous loss and due to damping or changes in

the domain configuration.

The effect of eddy currents can also be represented by the eddy current factor.[10]

$$\mu' = \mu \bullet X' \tag{40}$$

and

$$\mu'' = \mu \bullet X'' \tag{41}$$

where X' represents the real component and X'' the imaginary component of the eddy current factor. In order to calculate the eddy current factor and the effect of eddy currents on the magnetic field and induction inside a material, the geometry of the material must be considered.

Skin effect and geometry   As a result of eddy currents, the magnetic induction decreases from the surface of the material to the interior. The depth at which the magnetic induction has reached $1/e$ of its original value is the skin depth which is denoted as s due to the use of δ as the loss angle. The skin depth and the eddy currents depend on the frequency of the magnetic field, the permeability and the resistivity of the material.

For the simple case of a plane wave impinging on a plane infinite conducting sheet, the magnetic field inside the sheet is represented by

$$H = H_o e^{(\frac{-z}{s})} \cos(\omega t - \frac{z}{s}) \tag{42}$$

where H_o denotes the magnetic field at the surface of the sheet, z the position in question inside the sheet, and ω (= $2\pi f$) the frequency of the applied magnetic field. The skin depth s is represented by

$$s = \sqrt{\frac{2}{\omega\sigma\mu}} \tag{43}$$

where σ denotes the conductivity of the material, and μ the permeability of the material at a given magnetic field. For example, at 1 kHz, soft iron with μ_r = 500 and σ = 1 x 10^7 $\Omega^{-1}\cdot m^{-1}$ has a skin depth of 0.23 mm.[5] As frequency and conductivity increase, the skin depth of the material decreases and the applied magnetic field affects less of the material.

As Bozorth[10] has shown, for a cylindrical geometry, the magnetic field at a radius r inside the material is given by

$$H = H_o[\frac{ber^2(2\theta r/d) + bei^2(2\theta r/d)}{ber^2\theta + bei^2\theta}] \tag{44}$$

where ber and bei are the real and imaginary components of combinations of Bessel functions (see Appendix B), d the diameter of the sample, and

$$\theta = [\frac{f}{f_c}]^{\frac{1}{2}} \tag{45}$$

where f_c is the characteristic frequency given by

$$f_c = \frac{\rho}{2\mu\pi^2 d^2} \qquad (46)$$

where ρ represents the resistivity.

The contribution of eddy currents to the induced emf can be gauged using the eddy current factor. For a cylindrical sample, the real component of the eddy current factor is represented by

$$X' = \frac{\mu'}{\mu} = \frac{2}{\theta}[\frac{ber\theta \; bei'\theta - bei\theta \; ber'\theta}{ber^2\theta + bei^2\theta}] \qquad (47)$$

The imaginary component is given by

$$X'' = \frac{\mu''}{\mu} = \frac{2}{\theta}[\frac{ber\theta \; bei'\theta - bei\theta \; ber'\theta}{ber^2\theta + bei^2\theta}] \qquad (48)$$

and all the variables in both equations are defined above. The magnitude of the eddy current factor is given by

$$X = \sqrt{X'^2 + X''^2} \qquad (49)$$

A plot of the complex eddy current factor for a cylindrical sample as a function of f/f_c is shown in Figure 39. The behavior of the magnitude of the eddy current factor is similar to the behavior of X' as the frequency increases and both are zero where f/f_c is

Figure 39. A plot of the magnitude and real and complex components of the eddy current factor for a cylindrical sample

infinite. However, the behavior of X'' is out of phase with the magnitude and is attributed to a loss component. The peak in the behavior of the complex eddy current factor X'' is due to the counteracting effects of an increase in energy loss due to eddy currents at low frequencies and eddy current shielding at higher frequencies.

Discontinuous changes in the magnetic field with time induce large eddy currents in a very short time. For example in a square wave field variation, eddy currents play an

important role in the losses incurred in the induced emf at the point where the field

changes discontinuously, but the effects disappear quickly when the field is constant since

a changing field is required to induce eddy currents in the material.

The secondary effects of a discontinuous change in the applied magnetic field are

due to inductances produced by the magnetic fields. After the discontinuous change in

the field gradient occurs, the behavior of the induced emf in a sense coil can be correlated

to the behavior of an LR-circuit. When the material is subject to a negative discontinuous

field gradient (step down), the induced emf is given by

$$\varepsilon = \varepsilon_o e^{(-t/\tau)} + b \tag{50}$$

where ε represents the induced emf, ε_o a product of the emf generated by the solenoid

and a factor depending on the ratio of wire resistances in the solenoid and the coil, and b

an offset factor in case the field does not originate at zero and steps from $-|H|$ to $+|H|$.

All values are given in volts. The time constant τ for the inductor-resistor magnetic

circuit is given by L/R in seconds.

The inductance is given by

$$L = \frac{N^2 \mu A}{l} \tag{51}$$

where N represents the number of turns in the coil, μ the permeability in the linear region

of the BH-curve at a given field, A the cross-sectional area, and l the length of the

sample. The inductance is proportional to the permeability and can be rewritten as

$$L = k(\mu' + j\mu'') \tag{52}$$

where k is a proportionality constant.

The exponential in equation 50 can be rewritten in terms of the permeability.

$$e^{-t/\tau} = e^{-tR/[k(\mu' + j\mu'')]} \tag{53}$$

Eliminating the complex term from the denominator of the exponential,

$$e^{-t/\tau} = e^{-tR(\mu' - j\mu'')/[k(\mu'^2 + \mu''^2)]} \tag{54}$$

and

$$\varepsilon = \varepsilon_o e^{-tR\mu'/[k(\mu'^2 + \mu''^2)]} e^{jtR\mu''/[k(\mu'^2 + \mu''^2)]} \tag{55}$$

The first exponential term on the right represents an exponential decay of the induced emf in time, while the second exponential term on the right is oscillatory and distorts the induced emf. The time constant for the decay is

$$\tau = \frac{k(\mu'^2 + \mu''^2)}{k\mu'} \tag{56}$$

which can be represented by the real and complex eddy current factor since k is a
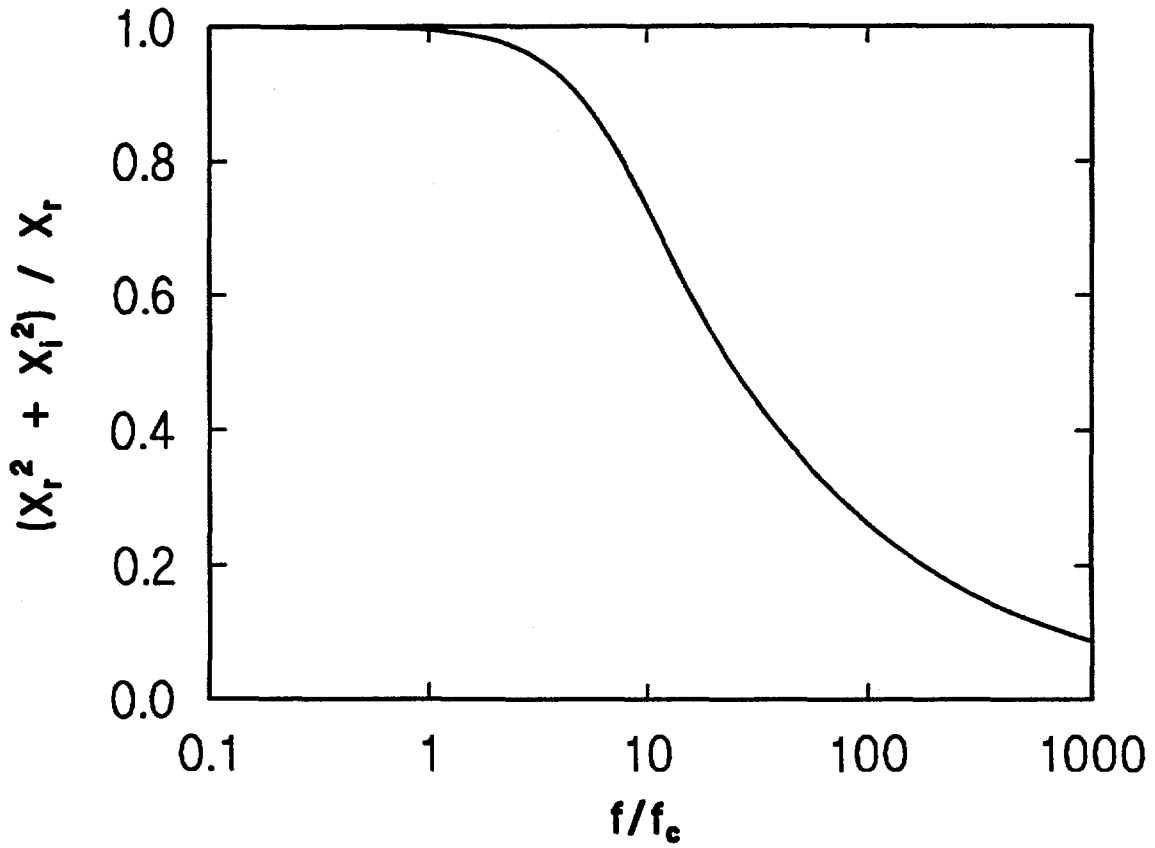
Figure 40. Plot of the decay constant as a function of f/f$_c$

constant and the change in R for a thin copper wire is negligible.

$$\tau \propto \frac{(X'^2 + X''^2)}{X'} \qquad (57)$$

The time constant given in equation 57 is plotted as a function of f/f$_c$ in Figure 40.

$\tau = 1$ when f/f$_c$ < 1. For f/f$_c$ > 1, the time constant exponentially decays increasing the

exponential decay of the induced emf at high frequencies.

Relaxation and disaccommodation

Sharp changes in the field gradient also result in a relaxation of the domain walls. At low frequencies, the wall energy remains equal to its static value and there is no relaxation. At high frequencies, the wall energy is not equal to its static value and energy losses occur due to relaxation effects attributed mainly to the creation and destruction of segments of domain walls. Above a certain frequency, the surface energy of domain walls will decrease to reduce the magnetostatic energy. Consequently, there is a decrease in the amount of domain walls used in the magnetization process and a transformation of the hysteresis loop occurs along with increased energy losses.[52]

Disaccommodation[50] is a relaxation effect which results when the magnetization is raised to an unstable value from which it returns in time. The disturbance can be either mechanical, magnetic, or thermal. The disaccommodation can be calculated by measuring the permeability soon after the application of an a.c. magnetic field and then at some time much later. The disaccommodation[50] is usually expressed as a percentage and can be given by

$$D = \frac{\mu_1 - \mu_2}{\mu_1 (\log_{10} \frac{t_2}{t_1})} \tag{58}$$

where μ_1 is the permeability at t_1, immediately after the application of an a.c. field, and μ_2

is the permeability at t_2, usually many hours or days later, depending strongly on the material. For example, in iron containing impurity carbon atoms, the disaccommodation is due to the diffusion of the carbon atoms with time which decreases the permeability. Disaccommodation in most cases produces a small change in permeability.

Most magnetic and magnetostrictive materials used in applications are subject to an alternating magnetic field. When considering ac applications of material such as Terfenol-D, it is very important to understand the dynamic response of the material. In this chapter, the dynamic response of a nickel bicrystal sample (a single crystal with a macro dislocation) has been examined building the basis for further experimental work on time dependent effects in ferromagnetic materials.

Materials and Experimental Methods

Measurements were taken on a 99.99% pure nickel bicrystal sample (8 mm diameter and 50 mm long) with the magnetic field applied along the length of the rod. A 30-turn coil was wound around the center of the sample to measure the induced voltage. The resistance of the coil was measured to be 0.652 Ω, and the inductance 3.5 mH.

The sample and coil were placed inside a long solenoid (maximum rise time of 0.2 ms) controlled by a bipolar power supply as shown in Figure 41. A function generator connected to the input of the bipolar power supply controlled the frequency, shape, and limits of the current output to the solenoid. The voltage across the solenoid was fed into one channel of a storage oscilloscope while the induced voltage in the coil wound around

Figure 41. Experimental set-up

the sample was fed into the other channel. In some cases, the induced voltage in the coil

was integrated with a fluxmeter before being fed into the oscilloscope to see the effect of

a dynamic field on B. Once a full cycle of both channels was stored in the memory of

the scope, the image was plotted through the analog output of the scope to paper. The

data was digitized and further analyzed with the help of a personal computer.

Measurements were taken for different waveform variations (ie. square, sinusoidal,

and triangular) of the magnetic field along with various magnetic field amplitudes, up to

24 kA/m, and frequencies ranging from 1 Hz to 1000 Hz. In addition, a semi-static

hysteresis loop was generated for the nickel sample with a sinusoidal waveform input and

a maximum magnetic field strength of 28 kA/m varied at 1.6 mHz.

Results

The quasi dc hysteresis curve for the nickel bicrystal sample, neglecting

demagnetizing effects, is shown in Figure 42. The maximum magnetic flux was found to

be 0.6 T at 28 kA/m, in agreement with the literature.[10] The permeability was 25, and the
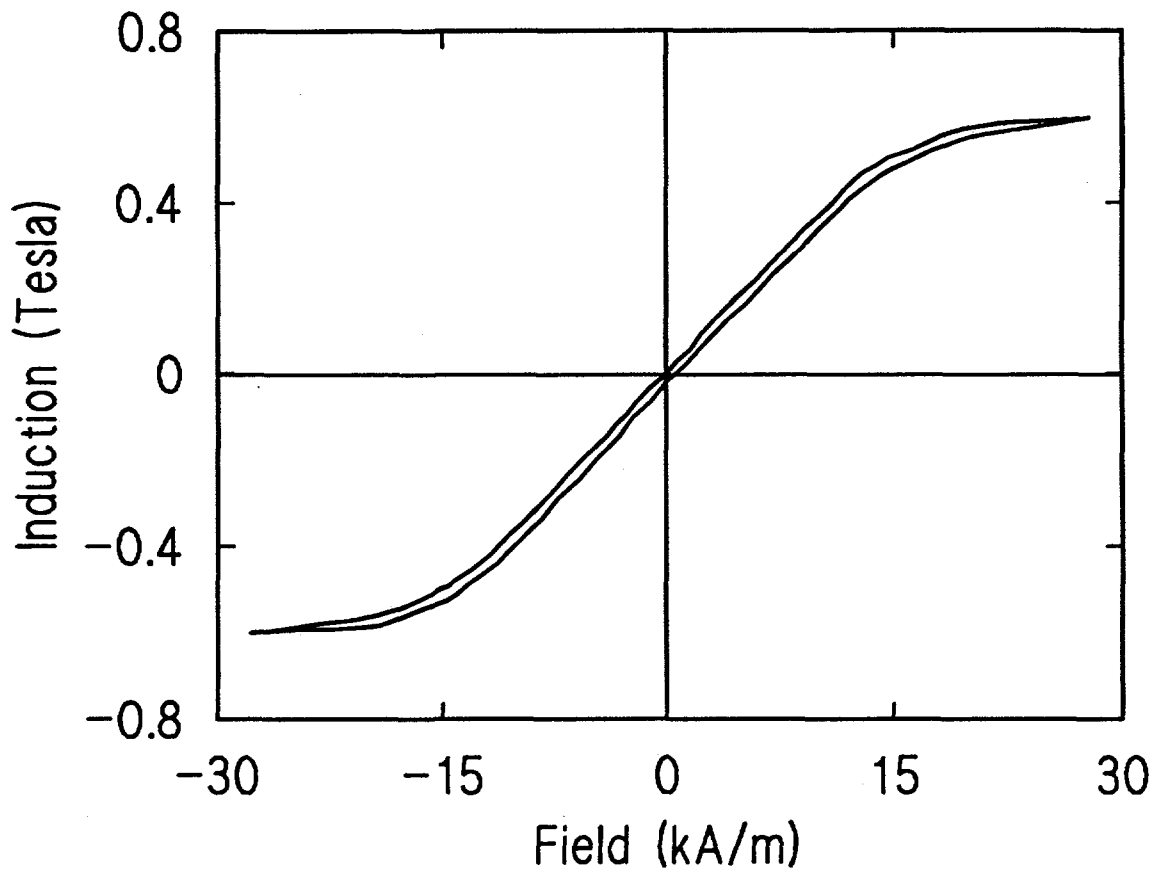

Figure 42. Hysteresis curve for the nickel bicrystal sample

characteristic frequency was calculated using equation 46 to be 86 Hz with $\rho = 0.087 \times 10^{-6}$ $\Omega \cdot m$ for nickel.[53]

Plots of the induced emf versus time are shown in Figures 43-46 for both continuous (sinusoidal) and discontinuous (triangular and square) changes in the magnetic field. Table 10 shows the frequencies, wave types, and drive fields for all the measurements presented.

The results for the sinusoidal waveform at 5 Hz, 10 Hz, and 25 Hz are shown in Figure 43 with a maximum magnetic field strength of 18 kA/m applied. At 25 Hz, the induced emf is almost parabolic, while at lower frequencies the emf becomes distorted. The maximum voltage induced is about 120 mV for 5 V input to the solenoid.

Table 10. Frequency, wave type, and drive field for the measurements taken

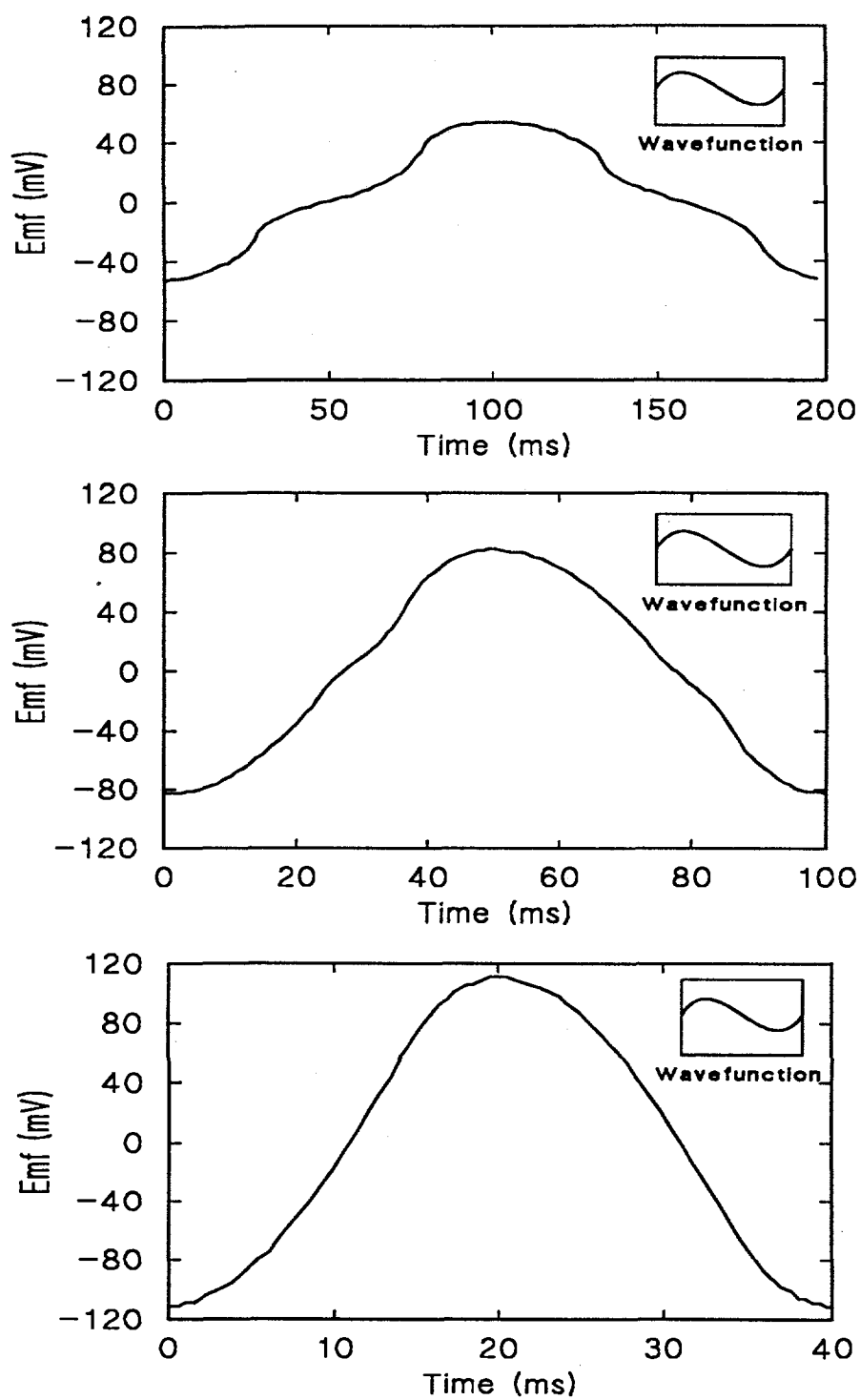| Wave Type					
Sinusoidal		Triangular		Square	
f	H_{max}	f	H_{max}	f	H_{max}
(Hz)	(kA/m)	(Hz)	(kA/m)	(Hz)	(kA/m)
5	18	5	9	10	3.6
10	18	5	28	200	3.6
25	18	10	9	200	9
---	---	10	28	200	18
---	---	20	9	200	28
---	---	20	28	1000	3.6

Figure 43. Induced emf for a magnetic field amplitude of 18kA/m varied
at 5Hz (top), 10Hz (middle) and 25Hz (bottom)

Plots for triangular waveforms at 5 Hz, 10Hz, and 20 Hz are shown in Figures 44

and 45 with a maximum magnetic field of 9 kA/m and 28 kA/m, respectively. The solid

lines represent the experimental data and the dotted lines represent the theoretical fit

derived assuming an a.c. magnetic circuit with an inductor and resistor present, equation

50. The static value of the time constant was calculated to be 5.37 ms which is inaccurate

for use in magnetic materials since it does not take the ac field dependence of the

permeability and variation in permeability along the length of the sample into account.

Therefore τ has been determined theoretically using a least fit method for each frequency,

wave type, and magnetic field amplitude. The plots of induced emf show an exponential

decay, except the plot at 5 Hz and 28 kA/m which is saturating. A maximum induced

voltage of 65 mV is reached for 2.5 V (or 9 kA/m) input and 60 mV for 7.75 V (or 28

kA/m) input.

Plots for square waveforms at 10, 200, and 1 kHz are shown in Figure 46 with a

maximum magnetic field strength of 3.6 kA/m applied, whereas square waveforms at 200

Hz are shown in Figure 47 for applied maximum field strengths of 3.6 kA/m, 9 kA/m, 18

kA/m, and 28 kA/m. In these figures, the solid lines again represent the experimental

data, and the dotted lines the theoretical data using the same fit as for the triangular

waveform. The plots show an exponential decay in all cases, as for the triangular

waveform. The maximum induced emf obtained is 185 mV at 200 Hz and 7.75 V (or 28

kA/m) input.

For the discontinuous waveforms, the induced emf as a function of time was

compared to the emf generated in an LR-circuit. Table 11 lists the theoretical values of

Figure 44. Induced emf for a magnetic field of amplitude 9kA/m varied
at 5Hz (top), 10Hz (middle), 20Hz (bottom)

Figure 45. Induced emf | H | =28kA/m varied at 5Hz (top), 10Hz (middle)
and 20Hz (bottom)

Figure 46. Induced emf for | H |=3.6kA/m varied at 10Hz (top), 200Hz (middle), 1000Hz (bottom)

Figure 47. Induced emf at 200Hz and 3.6 kA/m (a), 9 kA/m (b),
            18 kA/m (c), 28 kA/m (d)

and τ for both the triangular and square waveforms.

Plots of the induction versus time are presented in Figures 48 and 49. A triangular

field waveform at 5 Hz and 20 Hz with a maximum field strength of 18 kA/m applied is

and τ for both the triangular and square waveforms.

Plots of the induction versus time are presented in Figures 48 and 49. A triangular

field waveform at 5 Hz and 20 Hz with a maximum field strength of 18 kA/m applied is

applied shown in Figure 48. A square field waveform is shown in Figure 49 at 10 Hz and

Figure 48. Magnetic induction with | H |=18kA/m varied at 5Hz (top) and 20Hz (bottom)

Figure 49. Magnetic induction with $|H|$=18kA/m varied at 10Hz (top) and 200Hz (bottom)

Table 11. Theoretical parameters for the triangular and square waveforms

Waveform	f (Hz)	V (mV)	ε (m\`	$\varepsilon = \varepsilon_0 e^{-t/\tau} + b$		
triangle	5	5	0.05?			
triangle	10	5	0.06‹			
triangle	20	5	0.05(			
triangle	5	15.5	0.05!			
triangle	10	15.5	0.03‹			
triangle	20	15.5	0.06?			
square	10	2	0.03?			
square	200	2	0.02			
square	1000	2	0.013			
square	200	5	0.05588	0.0869	3.356E-4	-0.0547
square	200	10	0.11785	0.32261	2.467E-4	-0.1123
square	200	15	0.1866	0.39809	2.240E-4	-0.1770

[Handwritten annotation:] exponential term in the relaxation of magnetization

[Handwritten annotation:] constant term in due to the magnetic field changing

200 Hz with a maximum field strength of 18 kA/m applied. The magnetic flux displays a parabolic shape with time.

Discussion

For a continuous field gradient (sinusoidal), the maximum induced emf, neglecting the effect of eddy currents, is proportional to the frequency of the a.c. magnetic field.

$$\varepsilon \propto f \tag{59}$$

When eddy currents are present, the maximum induced emf is reduced by an amount proportional to the frequency over the characteristic frequency.

$$\varepsilon \propto \frac{f}{f_c} \tag{60}$$

Therefore, when the frequency is increased, the induced emf increases faster than the counteracting effect of the eddy currents.

For the sinusoidal waveform, eddy currents dominate the dynamic energy losses. In Figure 43, at 5 Hz, the magnetic flux of the nickel sample is saturating at high field strengths as can be seen by the flat peak in the induced emf. The material has sufficient enough time to respond to the changing magnetic field. As the frequency increases to 10 Hz, the induced emf increased but less than expected due to eddy currents. The eddy current factor is shown in Figure 39. At 10 Hz, $f/f_c = 0.12$ and the loss due to eddy currents is small.

As the frequency is increased to 25 Hz, the induced emf is also expected to increase significantly. However only a slight increase to 110 mV occurs compared to the estimated increase to around 200 mV. At this frequency the eddy currents are starting to reduce the induced emf of the nickel sample and $f/f_c = 0.29$.

At higher frequencies, the induced emf will be further reduced. At ≈ 700 Hz, the

loss due to eddy currents will be maximum. At even higher frequencies, the skin effect reduces the magnetic field inside the material and the resulting induced emf.

The square and triangular waveforms display discontinuous changes in magnetic field. In the square waveform, the discontinuous change is from a maximum negative field to a maximum positive field and vice versa. In the triangular waveform, the derivative of the field changes sharply from an increasing field to a decreasing field and vice versa.

As the magnetic field in the solenoid increases, either stepwise or linearly, the inductance in the nickel sample as measured by the coil wrapped around it increases also. For a step change in magnetic field, the increase in inductance is sharp to begin with determined by the instantaneous generation of the eddy currents and gradually tapers off due to the reduction in $d\phi/dt$, whereas with a linear increase in field, the increase in inductance is more gradual. With a step change in field, the inductance may overshoot due to eddy currents and decrease to a more stable value as in Figures 46 and 47(d).

Equation 50 was used to produce the theoretical fits with ε representing the induced emf, ε_o a product of the emf generated by the solenoid and a factor depending on the ratio of wire resistances in the solenoid and the coil, and b an offset factor because the emf does not start at zero. All are given in volts. The time constant for inductor-resistor magnetic circuit is given by τ (= L/R) in seconds. Table 11 shows the theoretical values of ε, ε_o, b, and τ for the triangular and square waveforms. The measured value does not compare with the theoretical value due to the field dependence of the magnetic properties of the material.

As seen in Table 11, the time constant τ is significantly smaller for the square waveforms. Therefore, the inductor responds more quickly with the square wave response than with the triangular wave response. The losses that reduce the permeability are mainly due to eddy currents with a small contribution due to relaxation effects. The disaccommodation was measured to be around 4.1% at 100 Hz.

CONCLUSIONS

Summary

This work has been concerned with the magnetization and magnetostriction of the rare earth iron alloy Tb-Dy-Fe, also known as Terfenol-D, and a nickel bicrystal. The work includes experimental measurements on these materials and theoretical modelling of the magnetic behavior of the materials under the action of a magnetic field and applied external pressure. In the later chapters results on magnetic disaccommodation in a pure nickel bicrystal are presented.

To show the differences in magnetic properties in two compositions of Terfenol-D, magnetic flux and magnetostriction data were taken on Terfenol-D with compositions $Tb_{0.3}Dy_{0.7}Fe_{1.95}$, $Tb_{0.3}Dy_{0.7}Fe_{1.9}$, and $Tb_{0.27}Dy_{0.73}Fe_{1.95}$. It was shown in that chapter that the application of a prestress resulted in an increase in the bulk magnetostriction in the higher anisotropy compositions $Tb_{0.3}Dy_{0.7}Fe_{1.95}$ and $Tb_{0.3}Dy_{0.7}Fe_{1.9}$. A large change in strain with applied field known as the 'burst effect' is also characteristic of this composition with prestress applied. A drawback, at least from the viewpoint of applications, is the presence of hysteresis in the magnetostriction.

The magnetostrictive properties of the lower anisotropic composition $Tb_{0.27}Dy_{0.73}Fe_{1.95}$ were very different. The application of a prestress along the $[11\bar{2}]$ direction resulted in only a small increase in bulk magnetostriction and no 'burst effect'. The change in strain with applied field was almost linear giving a low d_{33}. This

composition showed little hysteresis compared to the $Tb_{0.3}Dy_{0.7}Fe_{1.95}$ and $Tb_{0.3}Dy_{0.7}Fe_{1.9}$ compositions.

The magnetic properties of both compositions were explained in terms of domain wall motion and rotation. It was concluded that the large change in strain with applied field observed in the $Tb_{0.3}Dy_{0.7}Fe_{1.95}$ and $Tb_{0.3}Dy_{0.7}Fe_{1.9}$ compositions of Terfenol-D could be explained by domain rotation. The moments want to align along the [111] and [$\overline{111}$] directions 90° from the direction of applied stress at high prestress, where the magnetic processes are attributed mostly to 90° domain wall motion and rotation.

Existing models have given no further insight into describing the magnetic and magnetostrictive phenomena of this material. Therefore, a new theoretical model was developed. The three-dimensional anisotropic rotation model uses an approach similar to that taken by Stoner and Wohlfarth to explain the rotational processes in Terfenol-D for various levels of applied prestress and anisotropy. The model allows the magnetization vector to move in three dimensions as the magnetic field is increased. The magnetization vector was assumed to orient itself in the most energetically favorable position for any given applied magnetic field H. The magnetization vectors were initially oriented along each of the eight <111> easy directions in Terfenol-D and the magnetic field was applied along the [112] direction in one case and along the [111] direction in another case.

With no prestress applied, the magnetization vectors flip from their initial orientation directly into the [111] direction which lies closest to the direction of applied field. An applied prestress alters the initial orientations of the magnetization vectors. Upon the application of a magnetic field with prestress present the magnetization vectors

tend to flip from one <111> direction to another <111> direction closer to the field direction as the field increases. The critical field strength at which the magnetization vector rotates into the <111> direction closest to the field direction increases with prestress.

The change in magnetization with magnetic field was plotted for each initial orientation of the magnetization vector, along with the change in magnetostriction with applied field. The model did not take into consideration any interactions between magnetization vectors, so the theoretical data representing local magnetic behavior is not easy to compare with experimental magnetization and magnetostriction curves. Important information was gathered from the critical field values and the maximum values of magnetization and magnetostriction achieved for each initial orientation. The values of the critical field compared well with the experimental values.

A bulk magnetization and magnetostriction curve was generated by adding up the individual magnetization and magnetostriction curves in each of the eight directions for no prestress and a magnetic field applied along the [112] direction. These curves display a number of discontinuous changes in magnetization and strain because there is no interaction between domains. This is the main weakness of the three-dimensional anisotropic rotation model.

The magnetic properties of various <111> directions in Terfenol-D were also investigated. The [111] oriented samples of Terfenol-D were specially cut and magnetization curves were taken along three different crystallographic directions using a VSM. It was found that the coercivity did not vary for different crystallographic

directions, but the saturation value of the magnetization and the remanence differed between the different orientations, due to the magnetocrystalline anisotropy.

The origin of the static properties of Terfenol-D has been discussed but the dynamic properties are most important for applications. In general, an a.c. magnetic field applied to a magnetic material introduces new mechanisms of energy loss due to dynamic effects such as relaxation and the presence of eddy currents.

The properties of eddy currents in cylindrically shaped samples were reviewed and the eddy current factor was calculated and plotted as a function of the frequency. However, studies on relaxation effects are less common, harder to calculate, and produce a smaller energy loss. A system was built to measure the frequency response and relaxation of magnetic materials, in this case nickel.

The response of nickel to a discontinuous magnetic field gradient was measured for different frequencies between 5-1000 Hz and drive fields up to 28 kA/m. The experimental data were fit to the behavior of an LR circuit. Almost perfect fits of the magnetic behavior were obtained for magnetic conditions below the saturation point of nickel. The response of nickel to continuous changes in the magnetic field was measured and compared well to classical eddy current theories.

Future Work

Further work can be done on the three-dimensional anisotropic model in order to obtain closer fits to experimental data. The model will become more effective as the

algorithm for finding the direction of the magnetization vector is improved. In addition, it is important to add interactions between domains in order to more accurately simulate a material under real conditions. The metallurgical properties such as twins and temperature effects will later become important in improving the model. For this the anisotropy constants (K_1 and K_2) of different Terfenol-D compositions need to be more accurately determined. The magnetostriction and magnetic moment along different crystallographic directions in Terfenol-D will also be needed at different temperatures for a saturating field to allow the incorporation of temperature effects into the three-dimensional model.

The work on measuring the frequency response of nickel has to be expanded to include work on Terfenol-D at room temperature and different prestress levels for engineering applications. The knowledge of the change in strain and magnetic flux in Terfenol-D for different a.c. magnetic fields is vital for applications.

REFERENCES

1. R. Eisberg, and R. Resnick, *Quantum Physics of Atoms, Molecules, Solids, Nuclei, and Particles* (John Wiley and Sons, New York, 1985).

2. C. Kittel, *Introduction to Solid State Physics*, 6th ed. (John Wiley and Sons, New York, 1987).

3. J. Crangle, *Solid State Magnetism* (Edward Arnold, London, 1990), Chapter 7.

4. D. C. Jiles, *Introduction to Magnetism and Magnetic Materials* (Chapman and Hall, New York, 1991).

5. S. Chikazumi, *Physics of Magnetism* (John Wiley and Sons, New York, 1964).

6. B. D. Cullity, *Introduction to Magnetic Materials* (Addison-Wesley, Bonn, 1972).

7. E. W. Lee, Rept. Prog. Phys. **18**, 184-229 (1955).

8. A. E. Clark, *Ferromagnetic Materials*, ed. E. P. Wohlfarth (North Holland, Amsterdam, 1980), Chapter 7.

9. J. P. Joule, Phil. Mag. **30**, 76-87 (1847).

10. R. M. Bozorth, *Ferromagnetism* (D. Van Nostrand Co., Inc., New York, 1951).

11. R. C. Hall, J. Appl. Phys. **30**, no. 6, 816-19 (1959).

12. R. M. Bozorth and J. G. Walker, Phys. Rev. **88**, 1209 (1952).

13. C. M. Davis, H. H. Helms, and S. F. Ferebee, J. Acoust. Soc. Am. **29**, no. 4, 431-4 (1957).

14. C. M. Davis and S. F. Ferebee, J. Acoust. Soc. Am. **28**, no.2, 286-90 (1956).

15. N. E. Topp, *The Chemistry of the Rare Earth Elements* (Elsevier Pub. Co., New York, 1965), pp. 1-13.

16. J. J. Rhyne, and S. Legvold, Phys. Rev. **138**, A507-11 (1965).

17. A. E. Clark, B. F. DeSavage, and R. Bozorth, Phys. Rev. **138**, A216 (1965).

18. S. Legvold, J. Alstad, and J. Rhyne, Phys. Rev. Letts. **10**, 509 (1963).

19. J. R. Cullen and A. E. Clark., Phys. Rev. B **15**, no. 9, 4510-15 (May 1977).

20. R. D. Greenough, A. G. I. Jenner, M. P. Schulze, and A. J. Wilkinson, J. Mag. Magn. Mat. **101**, 75-80 (1991).

21. A. E. Clark and H. T. Savage, J. Mag. Magn. Mat. **31-34**, 849-851 (1983).

22. R. A. Laudise, *The Growth of Single Crystals* (Prentice Hall, New York, 1970).

23. A. S. Van der Goot and K. H. Buschow, J. of Less Common Mat. **21**, 151-157 (1970).

24. M. P. Dariel et. al., J. of Less Common Mat. **45**, 91 (1976).

25. J. D. Verhoeven, E. D. Gibson, O. D. McMasters, and H. H. Baker, Met. Trans. A **18A**, 223-31 (1987).

26. O. D. McMasters, J. D. Verhoeven, and E. D. Gibson, J. Mag. Magn. Mat. **54-57**, 849-50 (1986).

27. Y. J. Bi, A. M. H. Hwang, and J. S. Abell, J. Mag. Magn. Mat. **104-107**, 1471-72 (1992).

28. M. P. Schulze, N. Galloway, R. D. Greenough, D. C. Jiles, J. D. Verhoeven, P. Pulvirenti, presented at Intermag 1992 in Houston, Texas.

29. A. E. Clark, J. D. Verhoeven, O. D. McMasters, and E. D. Gibson, IEEE Trans. Mag. **MAG-22**, no. 5, 973-5 (Sept. 1986).

30. A. E. Clark, J. P. Teter, J. Appl. Phys. **68**, no. 8, 3910 (1988).

31. M. P. Schulze, R. D. Greenough, N. Galloway, to be published in IEEE Trans. Mag. 1993.

32. S. Habermehl and D. C. Jiles, Rev. Prog. QNDE **5A**, 843-852 (1986).

33. R. D. Greenough, A. G. I. Jenner, M. P. Schulze, and A. J. Wilkinson, J. Mag. Magn. Mat. **101**, 75-80 (1991).

34. F. Preisach, Z. Phys. **94**, 277 (1935).

35. I. D. Mayergoyz and C. E. Korman, J. Appl. Phys. **69**, no. 4, 2128-34 (1991).

36. A. Bergqvist and G. Engdahl, IEEE Trans. Mag. **27**, 4796-4798 (Nov. 1991).

37. D. C. Jiles and D. L. Atherton, J. Mag. Magn. Mat. **61**, 48-60 (1986).

38. M. J. Sablik and D. C. Jiles, J. Appl. Phys. **64**, 5402 (1988).

39. E. C. Stoner and E. P. Wohlfarth, Phil. Trans. Roy. Soc. **A240**, 599-641 (1948).

40. A. E. Clark, H. T. Savage, and M. L. Spano, IEEE Trans. Mag. **MAG-20**, no. 5, 1443-5 (Sept. 1984).

41. J. P. Teter, A. E. Clark, and O. D. McMasters, J. Appl. Phys. **61**, no. 8, (April 15, 1987).

42. J. D. Verhoeven, J. E. Ostenson, E. D. Gibson, and O. D. McMasters, J. Appl. Phys. **66**, no.2, 772-9 (1989).

43. A. E. Clark, J. P. Teter and O. D. McMasters, J. Appl. Phys. **63**, 3910 (1988).

44. J. P. Teter, K. Mahoney, M. Al-Jiboory, D. G. Lord, and O. D. McMasters, J. Appl. Phys. **69**, 5768 (1991).

45. *Model 4500 Vibrating Sample Magnetometer Instruction Manual* (EG&G Princeton Applied Research, New Jersey, 1989).

46. J. A. Osborn, Phys. Rev. **67**, 351-7 (1945).

47. J. A. Brug and W. P. Wolf, J. Appl. Phys. **57**, 4685-4694 (1985).

48. Fionillo, IEEE Trans. Mag. **26**, 2904 (1990).

49. Iozi, Phys. Rev. **80**, 1090 (1950).

50. E. C. Snelling, *Soft Ferrites: Properties and Applications* (Iliffe Books, Ltd., London, 1969), Chapter 8.

51. P. Lorrain and D. R. Corson, *Electromagnetic Fields and Waves*, third edition (W. H. Freeman and Co., New York, 1988).

52. M. Guyot, T. Merceron, and V. Cagan, J. Appl. Phys. **57**, no. 1 (15 April 1985).

53.   H. Kuchling, *Taschenbuch der Physik* (Verlag Harri Deutsch, Frankfurt, 1979) p. 627.

APPENDIX A. DERIVATION OF THE MAGNETOSTRICTION CONSTANTS IN TERMS OF THE STRAIN COMPONENTS[7]

The total anisotropy energy of a cubic crystal lattice is given by

$$E = E_o + E_{an} + E_{me} + E_{el} \tag{61}$$

where E_o denotes a constant of the energy, E_{an} the magneto-crystalline anisotropy energy, E_{me} the magnetoelastic energy, and E_{el} the elastic energy.

The energy can be written in terms of the direction cosines of the magnetization (α_x, α_y, and α_z), and the components of the strain ϵ_{ij} in cartesian coordinates to first order.

$$E_{an} = K_1(\alpha_x^2 + \alpha_y^2 + \alpha_z^2) + constant \tag{62}$$

$$E_{me} = b_o(\epsilon_{xx} + \epsilon_{yy} + \epsilon_{zz}) + b_1(\alpha_x^2\epsilon_{xx} + \alpha_y^2\epsilon_{yy} + \alpha_z^2\epsilon_{zz})$$
$$+ b_2(\alpha_x\alpha_y\epsilon_{xy} + \alpha_y\alpha_z\epsilon_{yz} + \alpha_z\alpha_x\epsilon_{zx}) \tag{63}$$

where b_o, b_1, and b_2 are the magnetoelastic constants.

$$E_{el} = \frac{1}{2}c_{11}(\epsilon_{xx}^2 + \epsilon_{yy}^2 + \epsilon_{zz}^2) + c_{12}(\epsilon_{yy}\epsilon_{zz} + \epsilon_{zz}\epsilon_{xx} + \epsilon_{xx}\epsilon_{yy})$$
$$+ \frac{1}{2}c_{44}(\epsilon_{xy}^2 + \epsilon_{yz}^2 + \epsilon_{zz}^2) \tag{64}$$

where c_{11}, c_{12}, and c_{44} are the elastic constants.

The magnetostriction $\Delta l/l$ is determined from the definition

$$\frac{\Delta l}{l} = \sum_{i \geq j} \epsilon_{ij}^{eq} \beta_i \beta_j \qquad (65)$$

where β_i denotes the direction cosines of the measurement

direction with respect to the cartesian axes, and ϵ_{ij}^{eq} are determined from

$$\frac{\delta E}{\delta \epsilon_{ij}} = 0 \qquad (66)$$

For a cubic crystal,

$$\epsilon_{ii}^{eq} = -\frac{b_1 \alpha_i^2}{(c_{11} - c_{12})} - \frac{b_o}{(c_{11} + 2c_{12})} + \frac{c_{12} b_1}{(c_{11} - c_{12})(c_{11} + 2c_{12})} \qquad (67)$$

and

$$\epsilon_{ij}^{eq} = -\frac{b_2 \alpha_i \alpha_j}{c_{44}} \qquad (68)$$

Substituting into the equation for the magnetostriction,

$$\frac{\delta l}{l} = \lambda^\alpha + \frac{3}{2}\lambda_{100}(\alpha_x^2\beta_x^2 + \alpha_y^2\beta_y^2 + \alpha_z^2\beta_z^2 - \frac{1}{3}) \\ + 3\lambda_{111}(\alpha_x\alpha_y\beta_x\beta_y + \alpha_y\alpha_z\beta_y\beta_z + \alpha_x\alpha_z\beta_x\beta_z) \qquad (69)$$

where

$$\lambda^{\alpha} = -\frac{3b_o}{(c_{11} + c_{12})} + \frac{3c_{12}b_1}{(c_{11} + 2c_{12})(c_{11} - c_{12})} \tag{70}$$

$$\lambda_{100} = -\frac{2b_1}{3(c_{11} - c_{12})} \tag{71}$$

$$\lambda_{111} = -\frac{b_2}{3c_{44}} \tag{72}$$

APPENDIX B. BESSEL FUNCTIONS

$$ber(\theta) = (-1)^{s-1} \left[\frac{\theta}{2}\right]^{4(s-1)} \frac{1}{(2s-2)!^2}$$

$$bei(\theta) = (-1)^{s-1} \left(\frac{\theta}{2}\right)^{4s-2} \frac{1}{(2s-1)!^2}$$

$$ber'(\theta) = (-1)^2 \, 2s \left(\frac{\theta}{2}\right)^{4s-1} \frac{1}{(2s)!^2}$$

$$bei'(\theta) = (-1)^{s-1} (2s-1)\left(\frac{\theta}{2}\right)^{4s-3} \frac{1}{(2s-1)!^2}$$

where $\theta = (f/f_c)^{\frac{1}{2}}$ and s is the order of the Bessel function.